

Control of LED Emission via Surface Plasmon  
Interaction

by

Michael D. Harries

A thesis submitted to Cardiff University for the degree of Doctor of  
Philosophy.

October 2009

UMI Number: U585249

All rights reserved

INFORMATION TO ALL USERS

The quality of this reproduction is dependent upon the quality of the copy submitted.

In the unlikely event that the author did not send a complete manuscript and there are missing pages, these will be noted. Also, if material had to be removed, a note will indicate the deletion.



UMI U585249

Published by ProQuest LLC 2013. Copyright in the Dissertation held by the Author.  
Microform Edition © ProQuest LLC.

All rights reserved. This work is protected against  
unauthorized copying under Title 17, United States Code.



ProQuest LLC  
789 East Eisenhower Parkway  
P.O. Box 1346  
Ann Arbor, MI 48106-1346

## **Acknowledgements**

I would like to thank all those that have supported me over the duration of this Ph.D.

In particular I would like to thank Dr. Huw Summers for giving me the opportunity to take part in this exciting research and for all his help and support over the years. I thank Dr. Pierpaolo Porta for his assistance, especially in experimental setups and for our very useful, almost daily, discussions on an area of research that was new to the department. I would also like to thank Prof. Peter Blood for his helpful lectures and discussions on semiconductor devices.

I huge thank you goes to my family, for their love and support both before and during the Ph.D., without which I would never have made it here in the first place.

<b>ACKNOWLEDGEMENTS.....</b>	<b>2</b>
<b>ABSTRACT .....</b>	<b>4</b>
<b>1 INTRODUCTION AND THEORY .....</b>	<b>5</b>
1.1 PROJECT AIM AND THESIS OUTLINE.....	5
1.2 SURFACE PLASMONS .....	8
1.2.1 Introduction .....	8
1.2.2 Theory .....	9
1.2.3 General Applications .....	21
1.3 SEMICONDUCTOR LIGHT EMITTING DIODES.....	23
1.3.1 Brief History .....	23
1.3.2 Theory.....	23
1.4 PHOTON-SURFACE PLASMON INTERACTION .....	44
1.4.1 Controlling light using surface plasmon interaction .....	44
1.4.2 Semiconductor devices with integrated coupling with surface plasmon waves.....	46
<b>2 EXPERIMENTAL TECHNIQUES .....</b>	<b>49</b>
2.1 OPTICAL POWER VERSUS EMISSION ANGLE.....	49
2.2 FAR-FIELD EMISSION IMAGES .....	51
<b>3 SUBWAVELENGTH-APERTURED GOLD GRATING .....</b>	<b>53</b>
3.1 DEVICE DESIGN .....	53
3.2 FAR-FIELD EMISSION IMAGES .....	58
3.3 ANALYSIS OF EMISSION PATTERN .....	61
3.4 EMISSION SPECTRA.....	63
<b>4 PERIODIC GOLD FILM .....</b>	<b>70</b>
4.1 HEXAGONAL AND SQUARE GRATING.....	73
4.3 1-D GRATING.....	75
4.3.1 Device measurements.....	75
4.3.2 Alternative grating pitch.....	82
<b>5 SURFACE PLASMON ANALYSIS.....</b>	<b>86</b>
5.1 CALCULATED VERSUS EXPERIMENTAL SURFACE PLASMON WAVE-VECTOR VALUE .....	86
5.2 DIPOLE ANTENNA ARRAY AND SURFACE PLASMON PROPAGATION LENGTH .....	91
<b>6 DISCUSSION AND CONCLUDING REMARKS .....</b>	<b>100</b>
<b>7 APPENDIX.....</b>	<b>105</b>
7.1 MATLAB CODE FOR THE ANALYSIS OF GRATING COUPLING.....	105
7.2 MATLAB CODE FOR N-DIPOLE ARRAY .....	107
7.3 REFRACTIVE INDEX DATA FOR GOLD AS A FUNCTION OF WAVELENGTH(60).....	108
<b>BIBLIOGRAPHY .....</b>	<b>109</b>

## Abstract

In this thesis we demonstrate how the optical emission from a typical light emitting diode (LED) device can be spatially controlled via the deposition of a periodically structured gold film.

A periodically structured gold film was deposited within a 20  $\mu\text{m}$  square aperture in the top, p-doped, contact surface of an AlGaInP/GaInP multiple quantum well edge emitting LED. We show that the far-field emission is vastly altered and is spatially controlled by the properties local to the surface plasmon. It is shown that each order of rotational symmetry produces a single emission curve in the far-field which is related directly to the coupling of photon to surface plasmon via the grating vector.

We find that the origin of these strong emission curves in the far field is emission of the surface plasmon as photons. These are highly polarised and have a peak emission of 660 nm (as opposed to the peak wavelength from the standard LED device of 654 nm). The k vector for the surface plasmon propagating within the thin gold film with  $\text{SiO}_2$  islands is found to be  $1.002 \times 10^7 \text{ m}^{-1}$  from experimental measurement. It is also shown that a similar gold film with a grating of 592 nm would result in normal emission.

Considering the surface plasmon emission as being analogous to emission from a linear dipole antenna array, the far-field emission as a function of angle is modelled using Matlab. From comparison with real profile plots this suggests that a surface plasmon wave spans a distance of 7.5 nm which agrees approximately with the propagation length of a surface plasmon in this gold film.

# 1 Introduction and Theory

## 1.1 *Project Aim and Thesis Outline*

This research was funded as part of Research Councils Basic Technology Research Programme grant to carry out research and development of an ‘optical biochip’. The Optical Biochips project aims to reduce typical biological experiments to the micro-scale level. This includes light emission, detection and methods to control and manipulate the biological sample. Benefits include improving the success rate of drug discovery, diagnosis of disease and allowing complex biological tests to be done away from the laboratory.

The general aim of this PhD project is to achieve coupling between photons and surface plasmons within a semiconductor device. This is work related to the Optical Biochips project as it would possibly allow Surface Plasmon Resonance (SPR) experiments to be undertaken using a single handheld device. SPR is an experimental method used mainly by cell biologists as a way of quantifying cell reactions, and their rates. This experiment uses separate components such as a light source, a prism and a detector, and it is our aim to combine these into a single device. This would reduce the experiment from a substantial piece of equipment, generally confined to a laboratory, to a component that could be integrated into an optical biochip and used to provide measurements in the field.

Surface Plasmons, which are electron oscillations which exist at the interface between a metal and dielectric material, can be classed as non-radiative. A major challenge focuses on how to achieve and control the interaction between photons emitted from a semiconductor device, and surface plasmons. In conventional SPR experiments this is achieved by using methods such as ‘prism coupling’ and ‘grating coupling’. These methods will be discussed later in this chapter. The focus of this work will be on the interaction between light and gold films, deposited onto the surface of a light emitting diode (LED), designed to allow coupling between surface plasmons and free-space photons. Understanding this

would allow control over the spatial emission from the device due to well defined linear relationships between the wave-vectors of photons and surface plasmons. Upon understanding the surface plasmon properties further work could go towards using the devices within a SPR experiment on an optical biochip.

All work in this thesis is based on achieving interaction between light and surface plasmons on the top contact surface and an edge emitting LED. The semiconductor device used in this work is a AlGaInP p-i-n junction diode consisting of three GaInP quantum wells. An emission window is made within the thick gold contact layer which allows light to escape. It is within this window that a gold film with certain properties is applied to achieve photon to surface plasmon coupling.

This thesis first provides a background into the theory behind surface plasmons and their uses. We see how surface plasmons are a solution to Maxwell's equations at an interface between materials with specific dielectric constants. Surface plasmons are shown to be non-radiative and require specific localised changes for interaction with free-space photons to occur. Chapter 1 provides some history and background theory on the function of LEDs. A review of work done on the coupling between surface plasmons and light is undertaken. This section is split into looking at research on the interaction between surface plasmons and light where the light source is separate from the surface plasmon layer, or integrated. The work in this research would be classed as integrated as the light source and surface plasmon interface are both on a single device.

Chapter two explains some of the measurement techniques and experiment setups that are used throughout this research. The measurements taken are mainly concerned with the photonics of the device and therefore require careful planning and an accurate setup.

Chapter 3 and 4 show the measurements taken from modified LED devices. They show that interaction between surface plasmons and photons is possible and has some interesting properties. These include a modification of the typical isotropic

far-field emission associated with an LED, a change of the emission spectrum and polarisation effects. These chapters also explain how the thin gold film was designed to allow coupling between surface plasmons and light and how this results in the spatial changes of the far-field emission from the top surface of the device.

In chapter 5 we analyse the previous experimental results to obtain a value for the wave-vector of the surface plasmon at the top surface. Using k-space analysis the far-field pattern is modelled and shows a close fit to experimental data. Furthermore the divergence of the strong angular emission is analysed. The system can be thought of as analogous to antenna emission, and surface plasmon emission is modelled as a linear array of emitting elements. Here we see that the number of elements contributing to the far-field pattern is related to the propagation length for the surface plasmon wave.

Chapter 6 summarises the achievements of the work done in this thesis, suggests improvements and future work.

The work associated with the research in this thesis has contributed to two journal papers: ‘Directional Control of Light-Emitting-Diode Emission Via a Subwavelength-Apertured Metal Surface’ by Michael D. Harries and Huw D. Summers(1); and ‘Surface plasmon mediated emission in resonant-cavity light-emitting diodes’ by Pierpaolo A. Porta, Michael D. Harries and Huw D. Summers (2).

## **1.2 Surface Plasmons**

### **1.2.1 Introduction**

In his work on characterising energy losses of fast electrons passing through thin metal films, Ritchie predicted the existence of self-sustained collective excitations at metal surfaces(3). It had already been noted by Pines and Bohm (4)(5) that the long-range nature of the Coulomb interaction between valence electrons in metals yields collective plasma oscillations similar to the electron-density oscillations observed by Tonks and Langmuir in electrical discharges in gases (6), thereby explaining early experiments by Ruthemann(7) and Lang(8) on the bombardment of thin metallic films by fast electrons. Ritchie investigated the impact of the film boundaries on the production of collective excitations and found that the boundary effect is to cause the appearance of a new lowered loss due to the excitation of surface collective oscillations (3). Two years later, in a series of electron energy-loss experiments Powell and Swan (9) demonstrated the existence of these collective excitations, the quanta of which Stern and Ferrell first referred to as the surface plasmon (10).

Since then, there has been a significant advance in both theoretical and experimental investigations of surface plasmons, which for researches in the field of condensed matter and surface physics have played a key role in the interpretation of a great variety of experiments and the understanding of various fundamental properties of solids. These include the nature of Van der Waals forces (11)(12), the classical image potential acting between a point classical charge and a metal surface (13)(14)(15)(16), the energy transfer in gas–surface interactions (17), surface energies (18)(19)(20), the damping of surface vibrational modes (21) (22), the energy loss of charged particles moving outside a metal surface (23)(24) and the de-excitation of adsorbed molecules (25). Surface plasmons have also been employed in a wide spectrum of studies ranging from electrochemistry (26), wetting (27) and biosensing (28)(29)(30) to scanning tunneling microscopy (31), the ejection of ions from surfaces (32), nanoparticle growth (33)(34), surface-plasmon microscopy (35)(36) and surface-plasmon

resonance technology (37)(38)(39)(40). Renewed interest in surface plasmons has come from recent advances in the investigation of the electromagnetic properties of nano-structured materials (41)(42), one of the most promising aspects of these collective excitations now being their use to control light in subwavelength structures and to enhance transmission through periodic arrays of subwavelength holes in optically thick metallic films (43)(44).

The so-called field of plasmonics represents an exciting new area for the application of surface and interface plasmons, an area in which surface-plasmon based circuits merge the fields of photonics and electronics at the nanoscale (45). Indeed, surface-plasmon polaritons can serve as a basis for constructing nanoscale photonic circuits that will be able to carry optical signals and electric currents (46)(47). Surface plasmons can also serve as a basis for the design, fabrication and characterisation of subwavelength waveguide components (48)(49)(50)(51)(52)(53)(54) (55). In the framework of plasmonics, modulators and switches have also been investigated (56)(57), as well as the use of surface plasmons as mediators in the transfer of energy from donor to acceptor molecules on opposite sides of metal films (58).

### 1.2.2 Theory

The free electrons of a metal can be treated as a high density liquid or plasma. Displacing a small number of electrons from their respective ions results in the density fluctuations known as “plasma waves” or “Langmuir waves”, occurring due to the restoring Coulomb force of the nearby positive ions. Using the free electron model it can be shown that the plasma oscillates at a frequency (59):

$$\omega_p = \sqrt{\frac{ne^2}{m\epsilon_0}} \quad (1.1)$$

where  $\omega_p$  is the angular frequency of the plasma oscillations,  $n$  is the density of electrons,  $e$  is the electric charge,  $m$  is the mass of the electron, and  $\epsilon_0$  is the permittivity of free space. It should be noted that this equation is calculated using the assumption of ions of infinite mass. This is a reasonable assumption as the mass of the ions is much greater than that of the electrons. A plasmon is the resulting quasi-particle associated with the quantisation of the plasma fluctuations.

Maxwell theory shows that under certain conditions plasmons can travel along a metal surface as longitudinal waves of electron oscillations. The plasmons that exist at an interface between are known as ‘surface plasmons’. The charge distribution and electromagnetic field of the surface plasmon waves is shown in Figure 1.

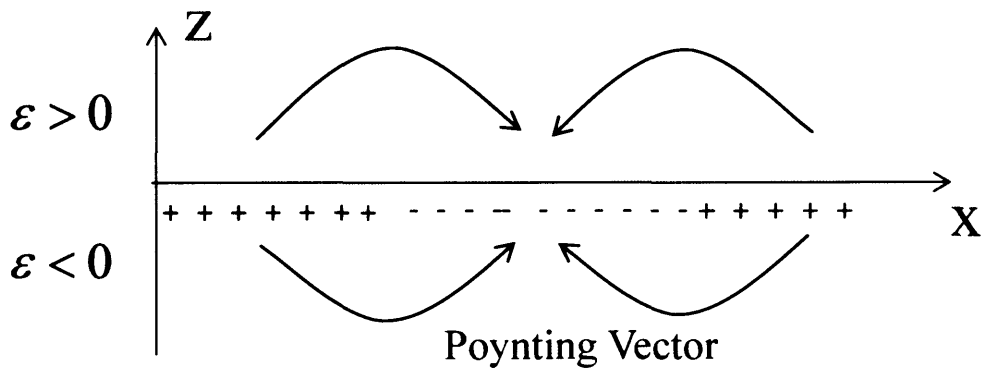


Figure 1: charge distribution and electromagnetic fields of the surface plasmons propagating on the surface in the  $x$  direction.

The dispersion relationship can be found by using Maxwell’s equations. Let us consider the surface plasmon dispersion relationship at the interface between a semi-infinite metal and material with a dielectric constant of  $\epsilon_d$ . The interface lies in the  $x$ - $y$  plane. The electric field of the surface plasmon travelling in the  $x$  direction can be described by

$$E = E_0^\pm \exp[i(k_x x \pm k_z z - \omega t)] \quad (1.2)$$

where we use '+' for  $z \geq 0$ , '-' for  $z \leq 0$  and where  $k_z$  is imaginary. The imaginary  $k_z$  results in the exponential decay of the electromagnetic field in the  $z$  direction. The maximum field is at the surface, where  $z=0$ , and this explains why surface plasmons waves are sensitive to the properties close to the interface.

We shall define the complex dielectric function of the metal,  $\epsilon_m$ , as

$$\epsilon_m = \epsilon'_m + i\epsilon''_m \quad (1.3)$$

A full derivation of the surface plasmon dispersion equation can be found in (60), however by considering a wave travelling in the  $x$  direction and applying Maxwell's equations at the interface we have:

$$\epsilon_d \left(\frac{\omega}{c}\right)^2 = k_x^2 + k_{zd}^2 \quad (1.4)$$

And

$$\epsilon_m \left(\frac{\omega}{c}\right)^2 = k_x^2 + k_{zm}^2 \quad (1.5)$$

With

$$\frac{k_{zd}}{\epsilon_d} + \frac{k_{zm}}{\epsilon_m} = 0 \quad (1.6)$$

Here  $k_{zd}$  is the  $z$ -component of the wave-vector in the dielectric, and  $k_{zm}$  is  $z$ -component of the wave-vector in the metal. As the  $k_x$  is continuous through the surface, the dispersion equation can be written as (60):

$$k_x = \frac{\omega}{c} \left( \frac{\epsilon_d \epsilon_m}{\epsilon_d + \epsilon_m} \right)^{\frac{1}{2}} \quad (1.7)$$

If we were to assume that the material adjacent to the metal is air ( $\epsilon_d=1$ ) and the metal has  $\epsilon_m < 0$ , and  $|\epsilon_m| > 1$ , it follows that  $k_x > \omega/c$  and  $k_{zd}$  and  $k_{zm}$  are imaginary or complex. This is as expected for a surface wave, where the maximum field is at  $z=0$  and decays exponentially as  $|z|$  increases.

It should be recognised in equation 1.7 that the dispersion equation of the surface plasmon is highly dependent on the dielectric constants of both mediums. However it is mainly dependent on the dielectric functions of the material at a distance less than the skin depth away from the interface. This distance varies with wavelength and dielectric constant, but it is generally less than a micron. This makes surface plasmons very useful in sensor applications such as in Surface Plasmon Resonance (SPR) experiments which will be explained further in the following section.

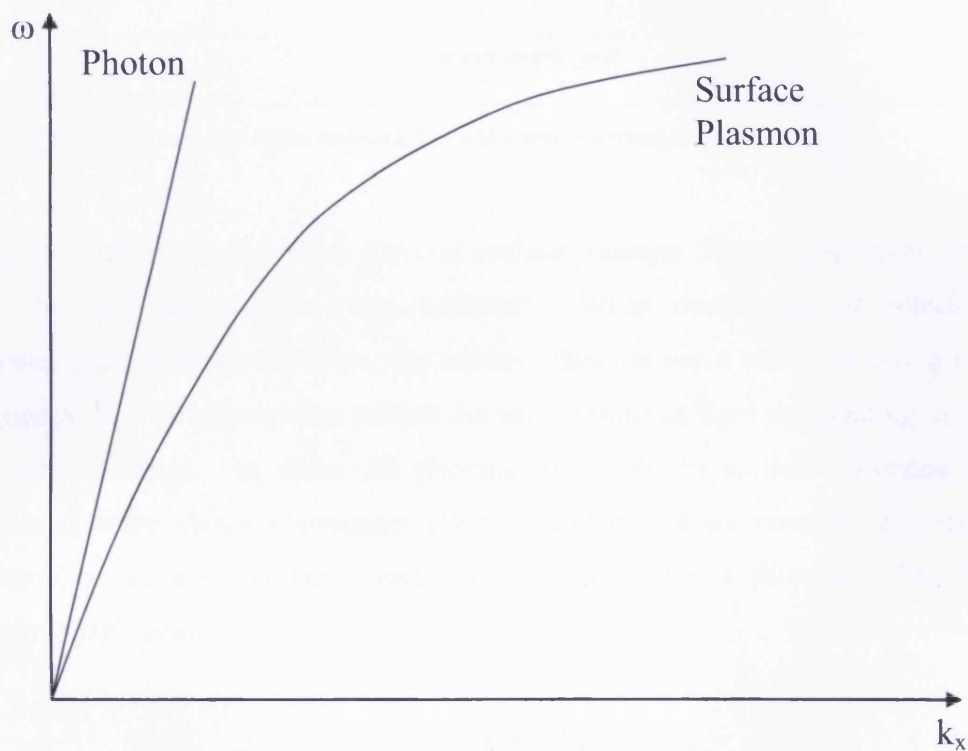


**Figure 2: Dispersion curve of a surface plasmon, at the surface between a dielectric and a metal, and a free-space photon travelling in the same dielectric material**

The surface plasmon curve does not follow the trend you would imagine from first inspection of equation 1.7. This is due to the dielectric index of metal being dependent on frequency, as shown in Figure 3.

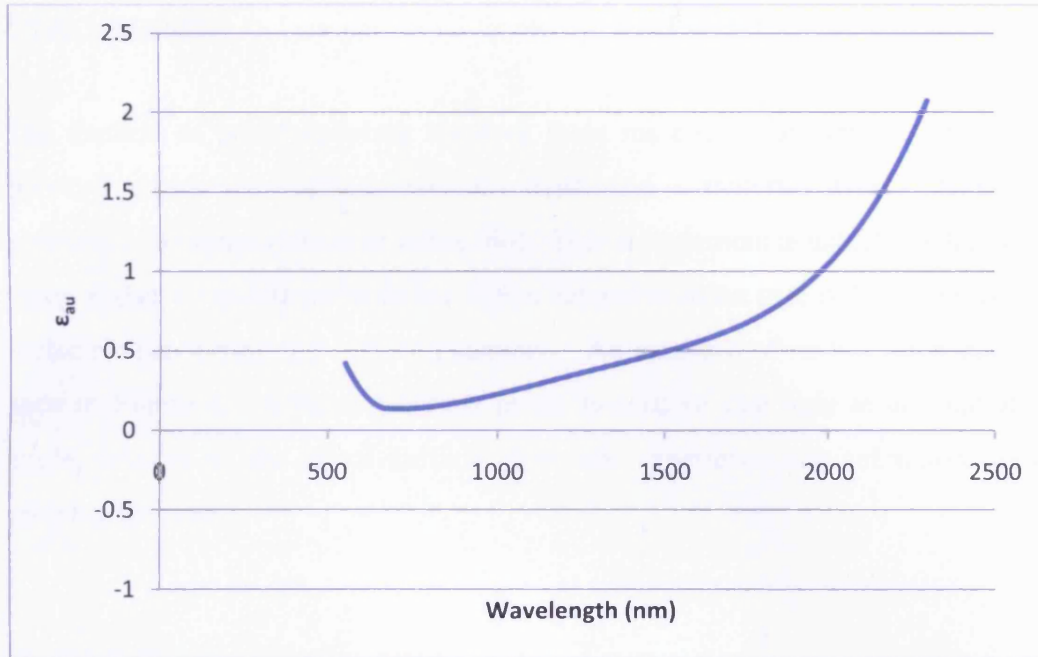


Figure 3: Plot of the real part of the dielectric for gold versus wavelength.

On inspection of the dispersion curve of surface plasmon, Figure 2, it can be seen why they are described as ‘non-radiative’. When considering an interface between a metal and a dielectric, the surface plasmon wave vector, at any given frequency, will be greater than that of the wave vector of light propagating in the dielectric material. In order for photons to couple to surface plasmons an additional wave vector component must be added. If we consider a surface plasmon on an x-y interface plane, propagating in the x direction, then for coupling to be possible

$$k_{sp} = k_{ph} + \Delta k_x \quad (1.8)$$

Where  $k_{sp}$  is the k vector of the surface plasmon,  $k_{ph}$  is the component of the k vector of the photon in the x direction.  $\Delta k_x$  is the additional wave-vector needed to allow photon-surface plasmon coupling. The two main methods of achieving coupling are by using grating coupling and prism coupling.

## Prism Coupling

The method of prism coupling involves three materials, the metal, a dielectric between which the surface plasmons exist, and a material with a dielectric constant of a higher refractive index (60). This arrangement is usually undertaken using a glass or quartz prism as the higher refractive index material, and air as the dielectric supporting the surface plasmons. An example of such a setup can be seen in Figure 4. A hemi-spherical prism is used so that light at any incident angle, relative to the metal surface, does not experience any refraction upon entering the prism.

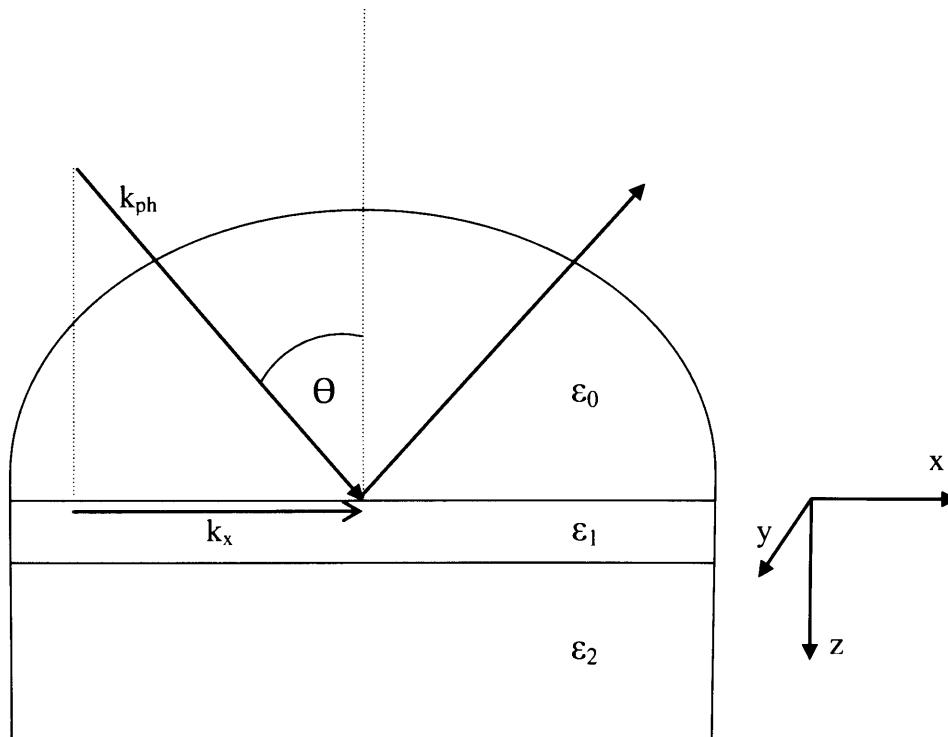


**Figure 4: Reflection of light at metal surface ( $\epsilon_1$ ). Medium above metal is dielectric material, typically glass or quartz, and the material below the metal film is a dielectric material where  $\epsilon_2 < \epsilon_0$ .**

Light incident upon the metal surface, as shown in Figure 4, has a wave vector, along the x-direction, of

$$k_x = \sqrt{\epsilon_0} \frac{\omega}{c} \sin \theta \quad (1.9)$$

The dispersion relation for the surface plasmons at the metal-air interface is

$$k_{sp} = \frac{\omega}{c} \left( \frac{\epsilon_1 \epsilon_2}{\epsilon_1 + \epsilon_2} \right)^{\frac{1}{2}} \quad (1.10)$$

Figure 5 shows the dispersion curves for both surface plasmon and light in both medium 0 and medium 2. The dispersion curve of the surface plasmon is marked as A and is defined by equation 1.7, although in Figure 5  $k_{sp}$  is plotted along the axis labelled  $k_x$  as to compare with the wave vector components of light in both media 0 and 2. The linear dispersion line of light in medium 2 is shown labelled as line C, and similarly light in medium 0 is marked as B.

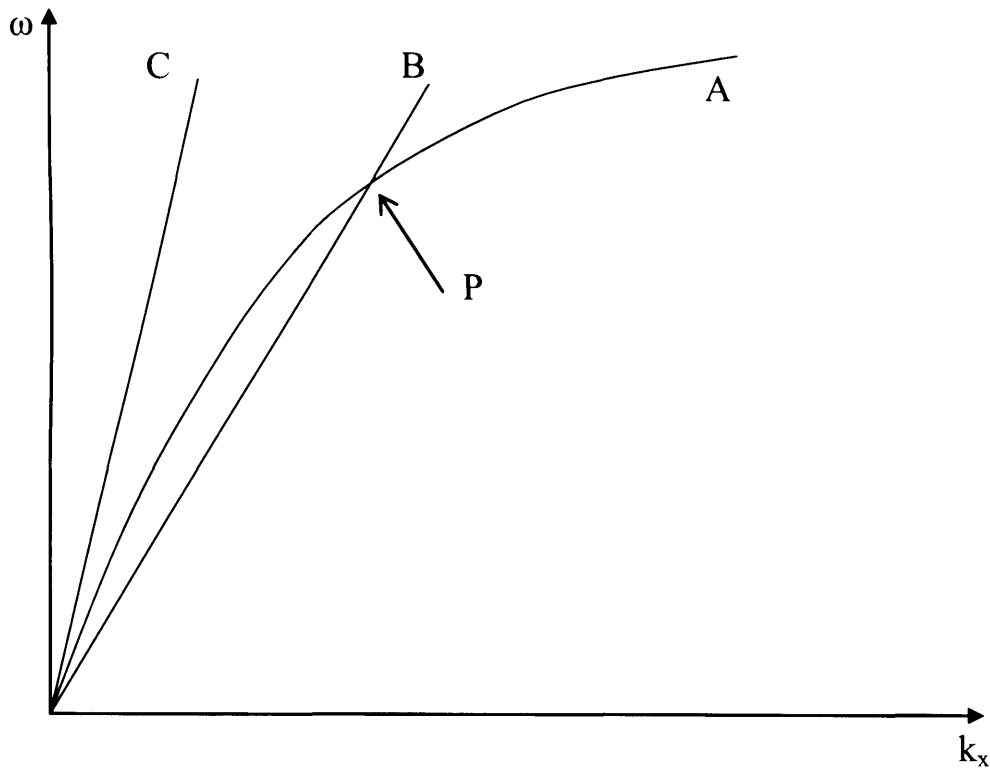


**Figure 5: Dispersion relationships of : (A) Surface plasmon at the interface between medium 1 and 2; (B) light in medium 0, and (C) light in medium 2.**

It can be seen in Figure 5 that light in air (material 2) would not be able to couple to the surface plasmons at the interface of 1/2. Hence surface plasmons are said to be non-radiative. Light in a material with a higher dielectric constant, for example light in the glass prism, can couple. In fact since curve B lies to the right of A up to point P light in material 0 can excite surface plasmons at the 1/2 interface up to the frequency at point P.

Coupling between light in material 0 and the surface plasmon at interface 1/2 can be achieved by making the metal layer significantly thin enough to allow an evanescent wave to interact with the surface plasmons at the metal-air interface. For the evanescent field to have significant amplitude at the metal-air interface the metal layer is thin, on the order of tens of nanometres. At the correct angle,  $\theta$ , (see Figure 4) the wave vectors of both the incident light (prism) and the surface plasmon (air-metal) are equal and coupling can occur. The simplest way to view the coupling is by measuring the reflected light as a function of incident photon

angle. At the angle that coupling occurs there will be a dip in the intensity of the reflected light, as photons energy transfers to surface plasmons.

### Grating Coupling

Another popular method of allowing photon-surface plasmons coupling is by introducing some form of periodicity into the system, e.g. a grating (60). For simplicity if we were to consider a grating with a pitch,  $\Lambda$ , then we can say that it has a wave-vector,  $k_g$ , where

$$k_g = \frac{2\pi}{\Lambda} \quad (1.11)$$

We can then combine equations 1.8 and 1.9 to show that coupling occurs when

$$k_{sp} = \sqrt{\epsilon_0} \frac{\omega}{c} \sin \theta_i \pm N k_g \quad (1.12)$$

where  $N$  is an integer and  $\theta_i$  is the incident angle of the light and  $k_{sp}$  is the surface plasmon wavevector. So, for a specific photon wavelength and grating pitch, the light will couple with surface plasmons at a particular angle.

This coupling angle is for a specific  $k_{sp}$ , which is dependent on the dielectric constants at the interface of the two materials, and therefore the angle varies depending on the materials being used. Coupling need not only occur with a grating of a single grating pitch. There simply needs to be some form of periodicity to produce the necessary additional wave vectors for coupling to be possible. There can also be a range of grating wave vectors, which would in turn result in a range of coupling angles. An example of this would be to have surface roughness at the interface.

It is often useful when considering real devices to consider coupling within two dimensional k-space. If we define a real-space plane lying in x-y as being parallel to the surface plasmon interface layer we can define a  $k_x$  and  $k_y$  as shown in Figure 6

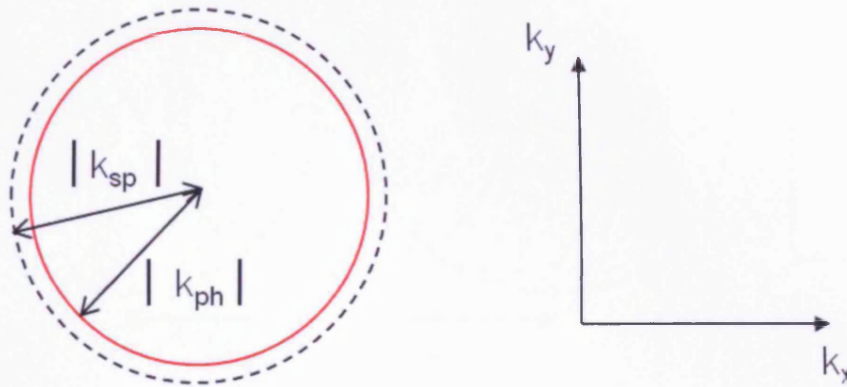


**Figure 6:** Two-dimensional k-space representation of a device without a grating. The circles represent the k vector values for a given wavelength.

The two concentric circles lie with their centre at the origin and represent the possible value of wave-vector for both the surface plasmon and free space photon. The dashed circle is that of the surface plasmon and the solid line is that of the free-space light. The radii of the circles correspond to the magnitude of both the  $k_{sp}$  and  $k_{ph}$  vectors, as defined previously. The value of  $k_{ph}$  shown in this diagram is equivalent to  $\theta=90^\circ$  (where  $\theta$  is the angle from the surface normal to the plane), which gives the largest possible component of the photon wave-vector in the x-y plane. We see in Figure 6 that the magnitude of the photon wave-vector is smaller than that of the surface plasmon. This is consistent with the dispersion relation shown in Figure 5 if one were to consider a specific frequency, or wavelength. The ‘light’ circle is within the circle of the surface plasmon and therefore even at  $\theta=90^\circ$  the wave-vector is not large enough to couple to the surface plasmon.

If we consider a grating or periodicity in the x direction we can effectively shift the surface plasmon circle by  $k_g$ . Figure 7 shows how the surface plasmon circle

is shifted by  $k_g$  in both the positive and negative x direction. We can see that there are arcs of the surface plasmon circle that lie within the maximum value of the photon wave-vector.

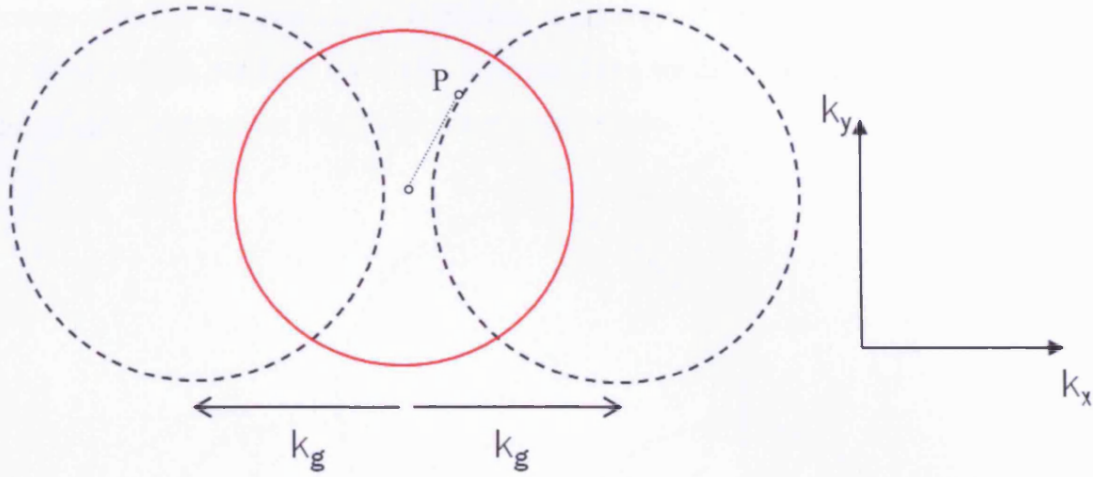


Figure 7: K-space representation of the effect a grating has on the photon to surface plasmon coupling.

Where the surface plasmon circles lie within the photon circle coupling can occur. The magnitude of the distance from a point, P, on the surface plasmon circle, within the photon circle, to the centre of the circle corresponds to a specific angle. We know that the photon k-vector circle is made from the largest value of wave-vector in the x-y plane. If we define the distance from P to the origin to be  $r$  (with units of  $m^{-1}$ ) we can say, from manipulation of equation 1.9, that the angle of coupling,  $\theta$ , is:

$$\theta = \sin^{-1} \left( \frac{rc}{\sqrt{\epsilon_0} \omega} \right) \quad (1.13)$$

It should be noted that Figure 7 shows a shift in the positive and negative x-direction of a single grating vector. If  $N$  (see equation 1.12) were to be greater than one then multiple pairs of surface plasmon circles would be drawn. It is possible, if  $k_g$  was smaller than shown in Figure 7, to have many more arcs from surface plasmon circles within the photon circle at value of  $N=1,2,3..$  etc.

Figure 7 shows a simple situation where there is a grating in a single direction, however there can of course be gratings in the y direction, or a combination of both. This approach, as shown in Figure 8, is still valid. We simply must shift the surface plasmon circles in the y-direction (or any required direction) by the necessary amount. Despite Figure 8 showing a grating with equal pitch in both x and y direction this need not always be the case. Here we define  $k_{xg}$  and  $k_{yg}$  as the grating vectors in both the x and y direction respectively.

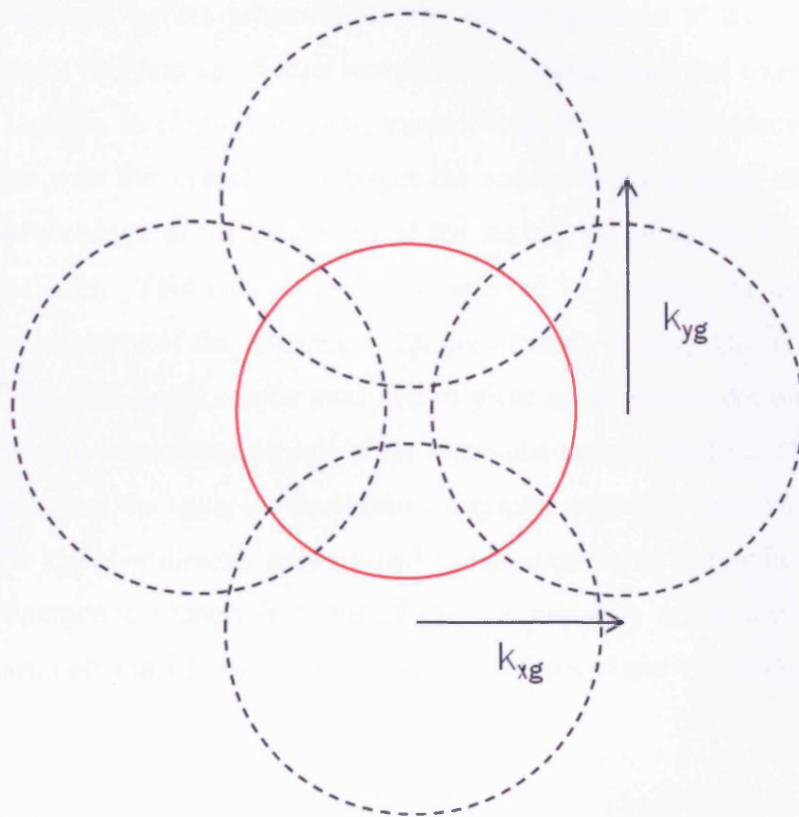


**Figure 8: K-space coupling between surface plasmons and photons for a device with periodicity in both x and y directions. The maximum photon wave-vector in the x-y plane is shown with a solid line circle whereas the dashed circles of radius  $|k_p|$  are representing the surface plasmon.**

### **1.2.3 General Applications**

#### Surface Plasmon Resonance (SPR)

Surface plasmon resonance is a phenomenon which occurs when light is reflected off thin metal films. A fraction of the light energy incident at a sharply defined angle can interact with the delocalised electrons in the metal film (plasmon) thus reducing the reflected light intensity. The precise angle of incidence at which this occurs is determined by the properties of the surface plasmon at the interface between the metal film and air. Target molecules are immobilised and fixed to the metal film. Ligands, in controlled areas, interact with these target molecules. If binding occurs with the immobilised target the local refractive index changes. This results in a change of the properties of the surface plasmon, and hence the SPR angle (61; 62). This change can be monitored in real-time by detecting changes in the intensity of the reflected light, producing a sensorgram. The rates of change of the SPR signal can be analysed to yield apparent rate constants for the association and dissociation phases of the molecule-surface reaction. The ratio of these values gives the apparent equilibrium constant (affinity). The size of the change in SPR signal is directly proportional to the mass being immobilised and can thus be interpreted crudely in terms of the stoichiometry of the interaction. Signals are easily obtained from sub-microgram quantities of material (61).

#### Plasmonic Computer Chips

Ongoing work continues into using surface plasmons as a method to transfer data within computer chips (45). The surface plasmon travels at the speed of light, leading to frequencies 100,000 times faster than current standard computer chips. Whilst photons can operate at the same speed they require guides (eg. optical fibres) about half the wavelength of the light, which is more than double the thickness of wires used in computer chips today.

Surface plasmons allow for the same speed as photons, but can be used in devices of the scale that computer chips are currently manufactured. Using surface plasmon waves to transfer data between transistors would stop the transfer interconnects becoming the limiting factor in chip speed. Research is currently being done on finding appropriate plasmon sources for silicon.

### Plasmonic Microscope

By placing a microscopic sample onto a thin metal coated glass surface, plasmons can be used to magnify images. A drop of glycerin is deposited on top of the glass. Laser light, shone through the glass, excites surface plasmons in the metal layer. The plasmons, with a wavelength of 70nm, scatter off the details that normal light cannot 'see' due to their shorter wavelength. The drop of glycerin redirects the plasmon waves into the metal layer, where a nanoscale grating allows the plasmons to be emitted as photons which can be captured by an ordinary microscope.

Using this method structures of the order of 150nm have been seen in the sample. This would have been impossible with a conventional microscope without the surface plasmons. It is believed that a lateral resolution of around 3nm could be achieved (63).

Other applications such as high density optical storage (64) and 'invisibility'(65) are current topics of great interest.

## **1.3 Semiconductor Light Emitting Diodes**

### **1.3.1 Brief History**

It was as early as 1907 that it was initially noted that a semiconductor junction could produce light. Henry Round, working at the Marconi Company, informed *Electrical World* that applying various voltages to carborundum crystals produced light of various colours. However it was not until 1955 that Rubin Braunstein, working at Radio Corporation of America, used semiconductor alloys (primarily GaAs) to produce infrared emission (66). Six years later Bob Biard and Gary Pittman, of Texas Instruments, found that when an electric current is passed through GaAs it emitted infrared light. Biard and Pittman were able to obtain a patent for the Infrared LED by proving the priority of their work (67). It was in 1962, when Nick Holonyak Jr., working at General Electric Company, created the first visible LED. As other work was being done on infrared emission, Holonyak developed a method of synthesising Gallium Arsenide Phosphide (GaAsP) crystals, which emitted red light. It was Holonyak's work that demonstrated the viability of III-V alloys and they are still used in all high performance LEDs and lasers today.

### **1.3.2 Theory**

#### Introduction to semiconductors

A semiconductor material sits between a metal and an insulator with respect to its ability to conduct electricity. A metal has many closely spaced energy levels between the valence and conduction band, or there are more accessible levels than there are electrons to fill them, which allows electrons to flow easily. In contrast in insulators there are as many valence band energy levels as there are electrons to occupy them. Whilst electrons are free to move from level to level within an insulator the net effect is negligible as electrons are indistinguishable from one another. The energy gap between the valence and conduction band is too large for

electrons to jump, even with a large potential difference is applied. Whereas in metals there is in effect no gap as the bands can be considered to overlap and any free electrons can flow through the material, contributing to a net electrical current. In insulators the band gap is far higher than the thermal energy of the electron. Semiconductors have an energy gap between valence and conduction band of  $\sim 1\text{eV}$ . Elemental semiconductors are those that consist of just one type of atom, such as Silicon. A compound semiconductor is a semiconductor compound composed of elements from two or more different groups of the periodic table. These compounds are mixed at a specific ratio to control the energy gap and lattice spacing in order to meet a required operating requirement.

A typical compound semiconductor is made using III-V semiconductors, meaning that one element is from column three of the periodic table and the other is from column five. Most III-V compound semiconductors crystallise in the zincblende structure; however in II-VI compounds the wurtzite structure often appears in addition to zincblende. A third semiconductor can be added into the mixture and what is known as a Ternary semiconductor is formed. For example aluminium can be added to GaAs to form AlGaAs, which is written as  $\text{Al}_x \text{Ga}_{1-x} \text{As}$ , where  $x$  refers to the content of the material within the compound. This step can go further and quaternary and quinary materials can be made (68). The work discussed in this thesis will be using a semiconductor made from a combination of GaAs and AlGaAs, which will be discussed later.

Semiconductors can be either intrinsic or extrinsic. An intrinsic semiconductor is one where the semiconductor is pure and therefore contains no impurity atoms. At room temperature a small number of electrons will have enough thermal energy to contribute to the conduction process. In effect the electron has enough energy to leave the electrostatic force of the atom, thus leaving a hole. This hole will soon be filled by another electron that has escaped into the conduction band. Therefore the flow of electrons in one direction, perhaps due to an applied potential, is equal and opposite to the flow of holes. So in an intrinsic semiconductor the number of free electrons,  $n$ , equals the number of holes,  $p$ . The number  $n$  is therefore a function of temperature, and material. Extrinsic

semiconductors are those which have been ‘doped’ with impurity atoms in order to introduce additional holes or free electrons into the semiconductor crystal. Dopants that create holes are known as acceptors and the semiconductor is classed as p-type. Similarly dopants that add additional electrons are known as donors and the material is referred to as n-type.

It is convenient to consider a simple band diagram to understand the energy levels within a semiconductor material. Figure 9 shows the valence band, conduction band and energy levels of both a donor and acceptor.

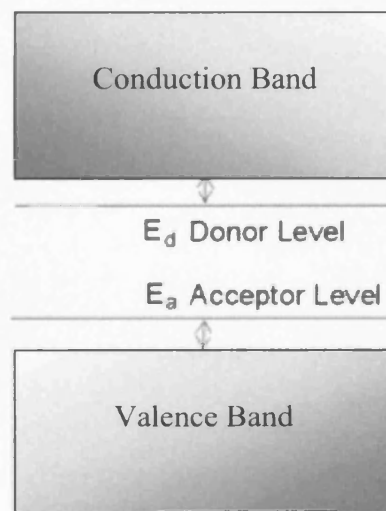


Figure 9: schematic energy band diagram of a semiconductor material.

This figure assumes that the wavevector,  $k$ , is zero. The energy gap is at a minimum for direct gap semiconductors when  $k=0$ . The top of the valence band is the highest filled level when  $T = 0K$  and the lowest level of the conduction band is the lowest unfilled level when  $T= 0K$ . The conduction and valence band can in fact be approximated by parabolic functions of  $k$  near the band edges:

$$\text{Conduction-band: } E = E_g + \frac{\hbar^2 k^2}{2m_e} \quad (1.14)$$

$$\text{Valence band: } E = -\frac{\hbar^2 k^2}{2m_h} \quad (1.15)$$

Where  $m_e$  and  $m_h$  are the effective masses of the electron and hole respectively and  $E_g$  is the band gap. The electron and hole effective mass is found to be

$$m_e = \frac{\hbar^2}{d^2 E / dk^2} \quad (1.16)$$

$$m_h = -\frac{\hbar^2}{d^2 E / dk^2} \quad (1.17)$$

### Fermi level

Electrons are fermions and therefore follow the Fermi-Dirac distribution function (59) as shown in equation 1.18 when in thermodynamic equilibrium.

$$f(E) = \frac{1}{\exp[(E - E_F) / k_B T] + 1} \quad (1.18)$$

Here  $k_B$  is the Boltzman constant and  $E_F$  is the energy at which there would be a probability of 0.5 of finding an electron. However only specific energies are allowed, defined by the density of states (equation 1.19) for the conduction band.

$$g(E) = \frac{V}{2\pi^2 \hbar^3} (2m_e)^{3/2} (E - E_g)^{1/2} \quad (1.19)$$

and the valence band,

$$g(E) = \frac{V}{2\pi^2\hbar^3} (2m_h)^{3/2} (-E)^{1/2} \quad (1.20)$$

Where the energy  $E$  is measured from the highest state of the valence band.

At high temperatures Equation 1.18 can be approximated to

$$f(E) = e^{-(E-E_F)/k_B T} \quad (1.21)$$

It follows that in the conduction band the number (per unit volume) of electrons is:

$$n = \frac{N}{V} \quad (1.22)$$

and so

$$n = \frac{1}{V} \int_{E_x}^{\infty} f(E)g(E)dE \quad (1.23)$$

$$n = \frac{(2m_e)^{3/2}}{2\pi^2\hbar^3} \int_{E_x}^{\infty} e^{-(E-E_F)/k_B T} (E - E_F)^{1/2} dE \quad (1.24)$$

$$n = 2 \left( \frac{2\pi m_e k_B T}{\hbar^2} \right)^{3/2} e^{-(E_F - E)/k_B T} \quad (1.25)$$

As in the valence band, the probability of a hole is

$$F_h(E) = 1 - F_e(E) \quad (1.26)$$

which can similarly be approximated to

$$F_h(E) = e^{(E-E_F)/k_B T} \quad (1.27)$$

A similar calculation yields the hole density

$$p = 2 \left( \frac{2\pi m_h k_B T}{\hbar^2} \right)^{3/2} e^{-E_F/k_B T} \quad (1.28)$$

The value of  $E_F$  depends on the number of acceptors ( $N_a$ ) and donors ( $N_d$ ). However  $E_F$  can be eliminated between equations 1.25 and 1.28 to give the important relation

$$np = n_i^2 = N_c N_v e^{-E_G/k_B T} \quad (1.29)$$

where  $N_c$  and  $N_v$  are the prefactors in (1.25) and (1.28),

$$N_c = 2 \left( \frac{2\pi m_e k_B T}{\hbar^2} \right)^{3/2} \quad (1.30)$$

$$N_v = 2 \left( \frac{2\pi m_h k_B T}{\hbar^2} \right)^{3/2} \quad (1.31)$$

As stated, (1.29) holds for all  $T$  and is independent of the values of  $N_a$  and  $N_d$ . In the intrinsic region, the extrinsic density is negligible, and then  $n=p$  since each electron excited to the conduction band leaves a hole behind it. In the intrinsic region, therefore

$$n_i = p_i = (N_c N_v)^{1/2} e^{-E_g/2k_B T} \quad (1.32)$$

If we substitute into (1.32) the values of  $n$  and  $p$  from (1.25) and (1.28),

$$m_e^{3/2} e^{-(E_F - E_c)/k_B T} = m_h^{3/2} e^{-E_F/k_B T} \quad (1.33)$$

This gives the value of  $E_F$  in the intrinsic region, and simple manipulation leads to

$$E_F = \frac{1}{2} E_g + \frac{3}{4} k_B T \ln \left( \frac{m_h}{m_e} \right) \quad (1.34)$$

Where  $E_g = E_c - E_v$  is the bandgap. The Fermi level of an intrinsic material lies close to the middle of the bandgap.

Within extrinsic semiconductors, where  $N_a^-$  and  $N_d^+$  are the number of ionised acceptor and donor sites respectively, charge neutrality means that:

$$n + N_a^- = p + N_d^+ \quad (1.35)$$

The number of sites that contain an electron can be found by:

$$N_d^+ = N_d [1 - f(E_g - E_d)] \quad (1.36)$$

And

$$N_a^- = N_a f(E_a) \quad (1.37)$$

It is typical to have some counter doping within a semiconductor material. For example in an n-type material  $N_d > N_a$  and  $N_a > 0$ . At  $T=0K$  the electrons from the donor sites move to fill the  $N_a$  acceptor sites. Therefore

$$N_d^+ = N_a \quad (1.38)$$

And means that the donor sites are not fully occupied.

This will not change for very low temperatures,  $k_B T \ll E_d$ , so substitution of the value of  $E_F$  into (1.25) gives for

$$n = N_c e^{-E_d/k_B T} \quad (1.39)$$

It is seen that (1.39) is definitely a low-temperature result. For p-type doping, the result corresponding to (1.39) is

$$p = N_v e^{-E_a/k_B T} \quad (1.40)$$

for

$$k_B T \ll E_a \quad (1.41)$$

The important operating condition is where all donors are ionised. This means that

$$n = N_d - N_a \quad (1.42)$$

Since  $N_a$  electrons are required for occupation of the acceptor sites. It can be seen that (69):

$$E_F = E_g - k_B T \ln \left( \frac{N_c}{N_d - N_a} \right) \quad (1.43)$$

The corresponding results for p-type doping are

$$p = N_a - N_d \quad (1.44)$$

$$E_F = E_g - k_B T \ln \left( \frac{N_v}{N_a - N_d} \right) \quad (1.45)$$

Note that in this technical region if the counter doping is negligible,  $N_a \ll N_d$  or  $N_d \ll N_a$ , (1.42) and (1.44) simplify to  $n = N_d$  and  $p = N_a$ .

## Semiconductor homojunctions and heterostructures.

Semiconductors are often combined to construct devices with useful properties. This includes combining semiconductors or different materials, different doping and different crystal lattice constants. For example, a junction between one or more semiconductors is known as a heterojunction. The differing energy gap across a heterojunction can confine current or photons, or both.

### p-n junction

We first consider a junction made between a semiconductor of identical material, but of opposite doping. This type of junction is commonly known as a homojunction. The fabrication of such a device is often done by doping, or during crystal growth, in order to decrease the effect of interface scattering that would occur if two separate pieces of semiconductor were physically combined.

The Fermi energy across the junction must be constant as the device is in thermal equilibrium.

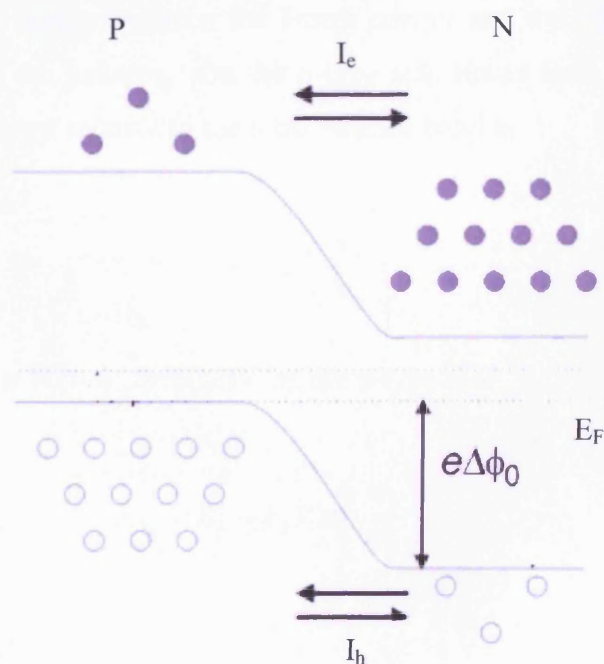


Figure 10: Energy band diagram at a p-n interface illustrating the band bending.

As the Fermi energy,  $E_F$ , is near the conduction band in the n-type material and near the valence band in the p-type, the bands bend across the junction.

The excess electrons on the n-type side diffuse into the p-type side of the junction. Similarly the excess holes move into the n-type side. Momentarily a current flow arises, referred to as the diffusion current. The recombination of carriers at the interface produces a depletion region or layer, containing the dopant ions. Positively charged ions exist in the n-type region and negatively charged ions in the p-type region. As recombination occurs more ions are created, resulting in an increasing electric field across the depletion layer. This electric field retards and then prevents further recombination. So there are two processes: the diffusion process which results in negatively charged ions, and the electric field, due to the ions, preventing further free-carrier diffusion. Therefore, under zero bias, equilibrium is quickly established.

To calculate the electric field we need to find the band offset. This is the difference in energy between the Fermi energy and top of the valence band on both sides of the junction. On the p-type side (away from the depletion region) the Fermi energy, relative to the local valence band is

$$E_{Fp} = k_B T \ln\left(\frac{N_v}{N_a}\right) \quad (1.46)$$

Assuming that  $N_d = 0$ . Similarly, on the n-type side

$$E_{Fn} = E_g - k_B T \ln\left(\frac{N_c}{N_d}\right) \quad (1.47)$$

where  $N_a$  is assumed to be zero. From Figure 10 it follows that

$$e\Delta\phi_0 = E_{Fn} - E_{Fp} = E_g + k_B T \ln\left(\frac{N_d N_a}{N_c N_v}\right) \quad (1.48)$$

and therefore that

$$\Delta\phi_0 = \frac{k_B T}{e} \ln\left(\frac{N_d N_a}{n_i^2}\right) \quad (1.49)$$

because

$$n_i = p_i = (N_c N_v)^{1/2} e^{-E_g/k_B T} \quad (1.50)$$

The variation of  $\phi$  along  $x$ , if the interface is in the  $y$ - $z$  plane, is the electric field.

$$E_x = -\frac{d\phi}{dx} \quad (1.51)$$

This can be calculated as long as the variations of  $N_a$  and  $N_d$  along  $x$  are known. If we assume that there is an abrupt junction, the charge distribution has the form

$$\rho(x) = \begin{cases} -N_a e & -w_p < x < 0 \\ N_d e & 0 < x < w_n \end{cases} \quad \text{for} \quad (1.52)$$

Where  $w_p$  and  $w_n$  are the semi-widths of the depletion region. The electric field must satisfy Gauss' Law

$$\nabla \cdot D = \rho \quad (1.53)$$

Since  $D = \varepsilon_0 \varepsilon_r E$  with  $\varepsilon_0$  constant, and in the present 1-d case

$$\nabla \cdot E = \frac{dE}{dx} \quad (1.54)$$

this gives

$$\frac{dE}{dx} = \begin{cases} -N_a e / \epsilon_0 \epsilon_r & -w_p < x < 0 \\ N_d e / \epsilon_0 \epsilon_r & \text{for } 0 < x < w_n \\ 0 & \text{otherwise} \end{cases} \quad (1.55)$$

The boundary conditions are  $E=0$  for  $x < -w_p$  and  $x > w_n$  since the junction is in equilibrium. The solution of (1.55) is therefore,

$$E = \begin{cases} \frac{-N_a e}{\epsilon_0 \epsilon_r} (x + w_p) & -w_p < x < 0 \\ \frac{N_d e}{\epsilon_0 \epsilon_r} (x - w_n) & \text{for } 0 < x < w_n \end{cases} \quad (1.56)$$

Furthermore,  $E$  must be continuous at  $x=0$ , which gives

$$N_a e w_p = N_d e w_n \quad (1.57)$$

As seen from the figure, this is simply the condition of electrical neutrality of the whole depletion region. The variation of  $E$  with  $x$  given is shown in (1.56)

Equations 1.51 and 1.55 together give  $\phi(x)$

$$\phi = \begin{cases} \frac{eN_a}{2\epsilon_0 \epsilon_r} (x + w_p)^2 & -w_p < x < 0 \\ \Delta\phi - \frac{eN_d}{2\epsilon_0 \epsilon_r} (x - w_n)^2 & \text{for } 0 < x < w_n \end{cases} \quad (1.58)$$

$\phi$  must be continuous at  $x=0$ ; this gives a second relation between  $w_p$  and  $w_n$ :

$$\Delta\phi = \frac{e}{2\varepsilon_0\varepsilon_r}(N_a w_p^2 + N_d w_n^2) \quad (1.59)$$

Recall that  $\Delta\phi$  is already known from (1.49). The variation of  $\phi$  with  $x$  given by (1.58). As stated, (1.49), (1.58) can be solved for the values of  $w_p$  and  $w_n$ ; they are,

$$w_n = \left( \frac{2\varepsilon_0\varepsilon_r N_a \Delta\phi_0}{eN_d(N_a + N_d)} \right)^{1/2} \quad (1.60)$$

$$w_p = \left( \frac{2\varepsilon_0\varepsilon_r N_d \Delta\phi_0}{eN_a(N_a + N_d)} \right)^{1/2} \quad (1.61)$$

An external voltage,  $V$ , can be applied across the junction. Forward bias is when the p-type semiconductor material is connected to the positive terminal of the battery, and the negative terminal to the n-type side. When this is the case electrons and holes both flow towards the junction, reducing the width of the depletion zone. The potential difference,  $eV$  appears between the Fermi levels on the p and n type side, as shown in Figure 11. It can be seen that as the voltage is increased the current across the junction increases as there is a smaller barrier to overcome.

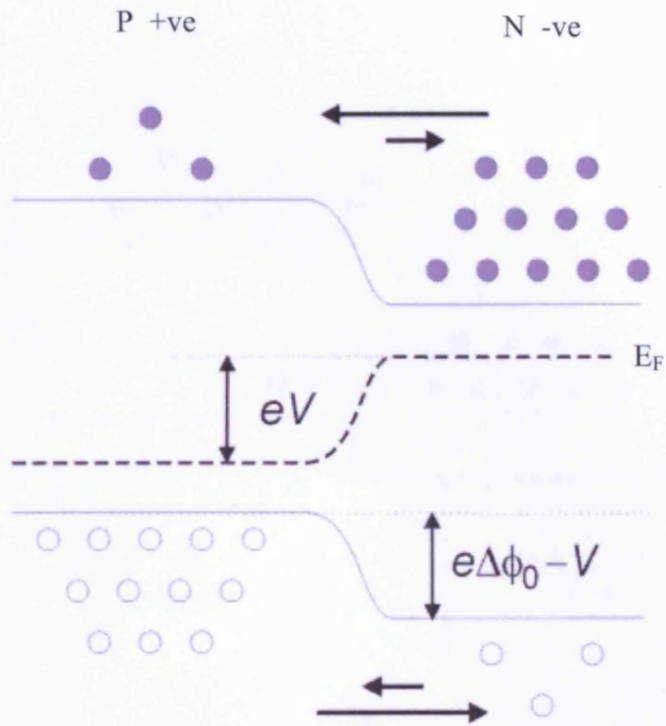


Figure 11: Energy band diagram showing a p-n interface with an external voltage,  $V$ , applying a forward bias. Arrows show the relative flow of carriers.

In reverse bias, where the negative terminal is attached to the p-type side of the junction (and positive terminal to n-type) the depletion width is increased. The holes in the p-type material are pulled away from the junction towards the cathode, and vice versa. This increases the voltage barrier and acts to reduce the flow of carriers, resulting in a high resistance across the p-n junction. See Figure 12.

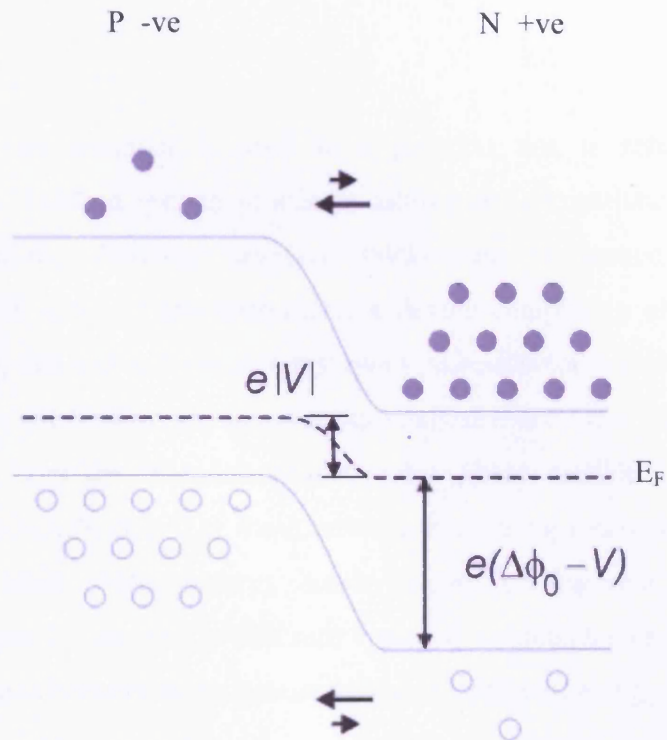


Figure 12: Energy band diagram showing a p-n interface with an external voltage,  $V$ , applying a reverse bias. Arrows show the relative flow of electrons and can be compared to those in Figure 11.

The modified depletion widths can be calculated in a similar method as shown previously and it can be shown that

$$w_n = \left( \frac{2\epsilon_0\epsilon_r N_a (\Delta\phi_0 - V)}{eN_d (N_a + N_d)} \right)^{1/2} \quad (1.62)$$

$$w_p = \left( \frac{2\epsilon_0\epsilon_r N_d (\Delta\phi_0 - V)}{eN_a (N_a + N_d)} \right)^{1/2} \quad (1.63)$$

The different operating properties of forward or reverse bias operation suggest that a semiconductor p-n junction can be used as a diode.

## Quantum wells

If more than one material is used at a junction this is referred to as a heterojunction. Modern growth processes allow very abrupt junctions between different materials, allowing interface thicknesses of around one atomic monolayer. The simplest heterostructure, a device comprising of one or more heterojunctions, that can be formed is just two semiconductor materials. There are common sets of III-V semiconductor compounds that are often used due to the quality of the interface that can be created. These include GaAs/AlGaAs, GaInAs/InP, GaN/AlN etc. The main advantage of using heterostructures is the possibility to often control energy bands, carrier confinement and photonic emission. Figure 13 shows the different types of semiconductor heterojunction that can be created between two semiconductors of different energy gap.

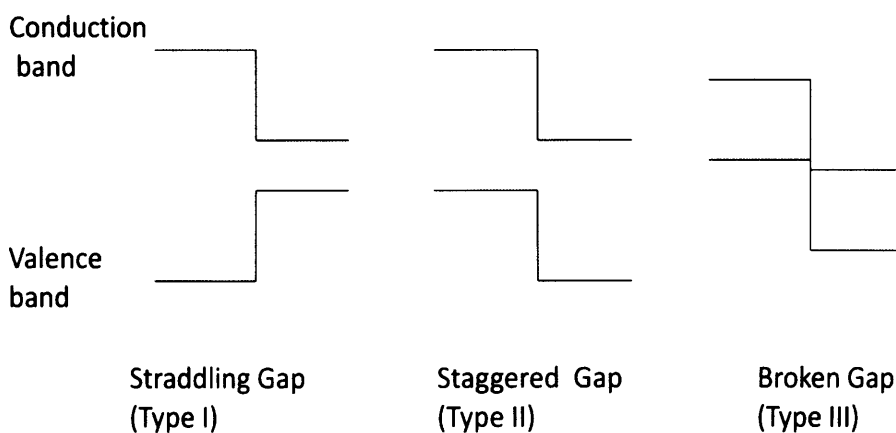


**Figure 13: Different configurations of semiconductor heterojunctions.**

If the wider bandgap material is added to both sides of the smaller bandgap material then what is known as a well structure is made (Figure 14).

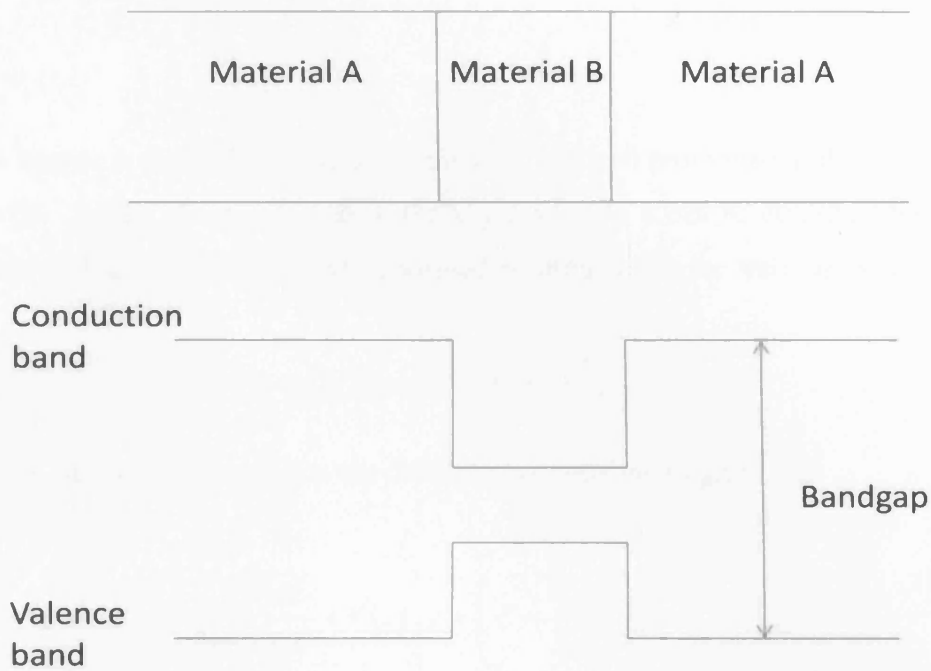


Figure 14: Schematic showing how a well can be made by placing a semiconductor between another with a wider bandgap. Here material A has a wider bandgap than material B.

Carriers can be confined to the smaller band gap material due to the potential barrier they experience at the interfaces with the wider bandgap material. If the width of the well is larger than that of the de Broglie wavelength of an electron it is referred to as a classical well and classical treatment of electron motion can be applied. However for well widths which are comparable or smaller than the de Broglie wavelength the classical approach breaks down and quantum theory must be applied.

Quantum wells are very useful for use in optoelectronic applications as their design allows some control of the properties of the device, especially the wavelength of emission.

To calculate the energy levels within the quantum well it is convenient to consider an idealised form of the potential

$$V(z) = \begin{cases} 0 & \text{for } |z| \leq w/2 \\ V_0 & \text{for } |z| \geq w/2 \end{cases} \quad (1.64)$$

Where  $w$  is the width of the quantum well, and  $z=0$  positioned at the centre of the well. As the electron is free in the  $x$ - $y$  directions it can be described by a plane wave. The wave function of a confined electron within the well can be written as

$$\psi(x, y, z) = e^{ik_x x + ik_y y} \cdot \chi(z) \quad (1.65)$$

This can be substituted into the Schrödinger equation to give

$$\left[ \frac{-\hbar^2}{2m_e^*} \cdot \frac{\partial^2}{\partial z^2} + V(z) \right] \chi = \left( E - \frac{\hbar^2 k_{xy}^2}{2m_e^*} \right) \chi \quad (1.66)$$

where  $k_{xy}$  is the wavevector of the electron in the  $xy$  plane and therefore  $\hbar^2 k_{xy}^2 / 2m_e^*$  is the kinetic energy of the electron in this plane.  $E$  is the total energy and therefore  $\varepsilon$  is the energy perpendicular to the interface plane.

$$\varepsilon = E - \frac{\hbar^2 k_{xy}^2}{2m_e^*} \quad (1.67)$$

There are two types of solution to this now one dimensional Schrödinger equation. If  $\varepsilon > V_0$  then we expect a continuum of unbound states, whereas if  $\varepsilon < V_0$  we expect discrete energy levels within the quantum well. The Schrödinger equation can be solved by fixing limits such as  $\chi$  is zero for  $z \rightarrow \pm \infty$ , and that  $\chi$  and  $d\chi/dz$  are continuous for all  $z$ .

The result can found to be (69)

$$\left( k_1 \frac{w}{2} \right)^2 + \frac{m_w}{m_b} \left( k_2 \frac{w}{2} \right)^2 = \frac{2m_w V_0}{\hbar^2} \left( \frac{w}{2} \right)^2 \quad (1.68)$$

Where

$$k_2 \sqrt{\frac{m_b}{m_w}} \frac{w}{2} = \frac{m_b k_1}{m_w} \frac{w}{2} \tan k_1 \frac{w}{2} \quad (1.69)$$

for even solutions, and

$$k_2 \sqrt{\frac{m_b}{m_w}} \frac{w}{2} = -\frac{m_b k_1}{m_w} \frac{w}{2} \cot k_1 \frac{w}{2} \quad (1.70)$$

for odd solutions.

$m_w$  and  $m_b$  are the masses of the electrons in the well and the barrier respectively.

Plotting  $k_2 \sqrt{\frac{m_b}{m_w}} \frac{w}{2}$  against  $k_1 \frac{w}{2}$  produces the graphs below, the potential

generates a circle of radius  $\sqrt{\frac{2m_w V_0}{\hbar^2}} \frac{w}{2}$ . The energy levels in the well are found

from the intersection of the tangent and cotangent relationships with the circle within the positive quarter. An example of this is shown in Figure 15.

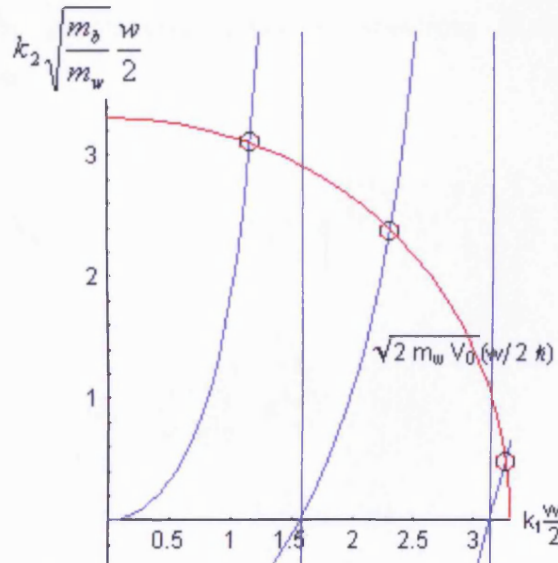


Figure 15: Graphical method of finding the energy levels within a quantum well. The intersection points, noted by circles, are supported energy levels.

These discrete energy levels exist in both the conduction and valence band for the smaller bandgap material. The confinement of carriers within this small area can lead to recombination and the interaction with electromagnetic fields. If we consider two generalised energy levels  $E_1$  and  $E_2$  then:

$$\omega = \frac{(E_2 - E_1)}{\hbar} \quad (1.71)$$

If the lowest energy,  $E_1$ , is occupied by an electron then an electromagnetic wave with the correct energy can raise this electron to the higher energy level  $E_2$ . This is photon absorption. Conversely an electron can lose energy from  $E_2$  to  $E_1$  and a photon of energy  $\hbar\omega$  will be emitted. Stimulated emission occurs where an electron in level  $E_2$  interacts with a photon of energy  $\hbar\omega$  and drops to level  $E_1$  whilst also emitting a photon with the same direction, polarisation and phase of the incoming photon. This process is known as stimulated emission.

If we take into account the energy levels within the conduction and valence band, transfer rates, incident photon densities, density of states within the semiconductor, the spontaneous emission spectrum from a device can be calculated to be (69):

$$R_{sp}(\omega) = D_0 (\hbar\omega - E_g)^{\frac{1}{2}} e^{\frac{\hbar\omega - E_g}{k_B T}} \quad (1.72)$$

where

$$D_0 = \frac{\sqrt{2} m_r^{3/2}}{\pi^2 \hbar^2 \tau_R} e^{\frac{-E_g}{k_B T}} \quad (1.73)$$

is a frequency independent constant.  $\tau_R$  is the radiative lifetime of electrons and holes, the reduced mass,  $m_r$ , of the electron-hole pair is

$$m_r = \frac{m_e m_h}{m_e + m_h} \quad (1.74)$$

Figure 16 shows a plot of this function, for illustrative purposes only, with the following parameters:

$T = 300\text{K}$ ,  $\tau_R = 1 \times 10^4$ ,  $E_g = 0.5\text{eV}$  ( $8 \times 10^{-20}\text{ J}$ ) and for simplicity the reduced mass used here was just the mass of an electron.

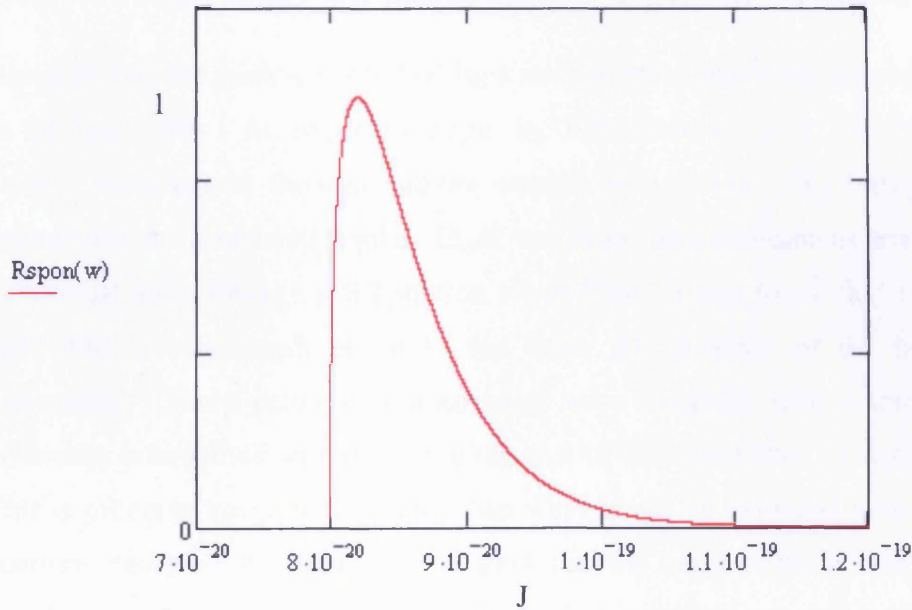


Figure 16: Plot of the normalised spontaneous emission spectrum  $R(\omega)$  (equation 1.72).

It can be seen that the spectrum has a low-frequency edge at  $\hbar\omega = E_g$ , and extends over a width of approximately  $2k_B T$ . Hence photons are emitted over a wide range of energies or, what we typically measure, wavelength.

The LED devices used in this research consist of three undoped intrinsic quantum well layers of GaInP sandwiched between AlGaInP p type and n type regions.

## 1.4 Photon-Surface Plasmon interaction

In the last thirty years there has been a large increase in the amount of work done on surface plasmons. Initially the main area of interest was aimed at developing optical sensors for biological, and chemical, measurements. This work was mainly based on the, now standard, Surface Plasmon Resonance (SPR) techniques used by cell-biologists today. More recently a lot of work has been aimed at the spatial control of light by using surface plasmon metal films and improving transmission efficiency through such films.

### 1.4.1 Controlling light using surface plasmon interaction

Research into the passive control of light using surface plasmons became popular in the late 1990s. An important paper by T.W. Ebbesen et al., 'Extraordinary Optical transmission through sub-wavelength hole arrays' (70) brought some unexpected and promising results. Light was shone on a two-dimensional array of cylindrical holes through a 0.2 micron silver film. It was found that zero-order light with a wavelength of up to ten times the diameter of the holes was transmitted. Sharp peaks in transmission were observed, with a transmission efficiency (normalised with respect to the area of the holes) often exceeding unity. This is orders of magnitude greater than what would be expected from standard aperture theory. T.W. Ebbesen et al show that the transmission is related to the coupling to photons to surface plasmons. The coupling is possible due to the metal film being periodically patterned with the cylindrical apertures.

Work by Tineko Thio et al (71), which included input from T.W.Ebbesen, took a closer look at this effect. In this paper the focus is stronger on the effect of the geometry of the hole array, and the importance of the diameter of the hole itself. The wavelength maxima were calculated by understanding the coupling that occurs between the incident light and the surface plasmons. For momentum conservation, and thus for coupling to occur

$$k_{sp} = k_x + iG_x + jG_y \quad (1.75)$$

where  $k_{sp}$  is the wave-vector (as shown in equation 1.7) of the surface plasmons,  $k_x$  is the wave-vector of the incident light.  $G_x$  and  $G_y$  are the k-space vectors of the periodic grating, where  $i$  and  $j$  are simply integers. This can be rearranged to show the resonance wavelength of the incident light at differing values of lattice integers  $i$  and  $j$ . The wavelength values obtained from these equations matched well with their experimental results. Once again transmission is greater than unity once normalised against the total area of the holes within the array that the light is incident.

Similar work on transmission through metallic gratings with arrays of holes/apertures has been done by U. Schröter et al. (72), Tae Jim Kim et al. (73), and H. J. Lezec et al. investigated transmission through a single aperture (74). They found that by using a textured surface around the aperture, in this case concentric circular gratings, they could control the divergence of the emerging beam. Using such a sub-wavelength aperture would normally result in light being diffracted over a wide range of angles. In their results the divergence was shown to be  $\pm 3^\circ$ . Interestingly, the angles of emission could be controlled spatially by altering the period of the grating. A longer grating pitch results in a higher emission angle (from perpendicular to the plane of the surface plasmons film). Similarly the coupling equations are dependent on wavelength, and as such the emission angles change with wavelength. Further theoretical work by L. Martin-Moreno et al (75) shows that the wavelength, angle (and angular width) of emission from a sub-wavelength aperture can be modified by the introduction of surface corrugations around the aperture and the tuning of its parameters.

Earlier in this chapter the two main ways of coupling between photons and surface plasmons were described. These were using a grating coupler, or via a prism coupler. In the above work the interaction between light and surface plasmons has been via a grating, or a periodic roughness or perturbation of some kind. The main advantage of using a grating over a prism is due to the fabrication and robustness of the finished device. Work by C. Geddes et al. (76) show that coupling and re-emission can be achieved by attaching a hemi-cylinder glass

prism. Useful in the author's area of fluorescence, they establish a new effect named Surface Plasmon Coupled Emission (SPCE). In this field the detection of the emission of fluorophores is very important. It is shown in this paper that excited fluorophores, which have been put into sulforhodamine 101 doped PVA and spin-coated onto the silver film, couple to the surface plasmons. Emission occurs from the alternate side of the metal film, through the glass prism. The emission occurs at a specific angle for a set emission wavelength, related by a coupling equation. Researchers believe that this could lead to multiple fluorophores being used on a single sample, each with their own observation angle related to their emission wavelength.

From the work done on the transmission of light through sub-wavelength apertures through metallic films, several interesting properties were found. These include enhanced transmission, low divergence, control of angular emission and the wavelength selection. These effects have the potential to be used very effectively to improve the functionality or efficiency of many optical devices.

#### **1.4.2 Semiconductor devices with integrated coupling with surface plasmon waves.**

An exciting area of work is that based on integrating surface plasmons films/layers into active semiconductor devices. There are many possible benefits from this, as noted in the previous section, including an improved efficiency and control over spatial emission.

Work done by A. Köck et al. (77) achieved an interaction by producing a line grating microstructure on the top surface of a AlGaAs/GaAs surface emitting LED. This was accomplished by etching a grating into the uppermost GaAs layer, and coating with a 25nm layer of silver. The paper describes how the emission from the device has been altered from that of a standard LED to emit light at specific angles. These angles can be calculated from considering two coupling

processes. Firstly the light generated within the LED must couple to the surface plasmons within the grating silver film. This occurs in the same manner as described previously in this chapter, and shown in equation (1.12). The surface plasmons now re-radiate into free-space photons on the upper side of the film. One LED that they made had a divergence of less than  $4^\circ$  and could have many benefits, such as coupling into waveguides or optical fibres. It should be noted that the directional emission was p-polarised light. This is to be expected as it is the orientation in which the electric fields of both photon and surface plasmons are aligned. The s-polarised light from one of their microstructured devices has the same angular emission profile as that of a standard LED.

Similar work was done by S. Gianordoli et al. in the paper 'Optimization of the emission characteristics of light emitting diodes by surface plasmons and surface waveguide modes' (78). All similar work prior to this has been done using simple line gratings. In this paper cross and hexagonal grating structures are used to excite and re-radiate surface plasmons. These structures were made using a photoresist mask which was patterned using holographic photolithography. This mask was exposed over the sample twice (separated by  $90^\circ$ ) for the cross pattern, or three times (separated by  $60^\circ$ ) for the hexagonal pattern. The pattern was transferred to the LED device by ion milling to a depth of 90nm. Au or Ag films of differing thicknesses were deposited on the gratings. The grating pitch was chosen to be 850nm which corresponded to emission at  $0^\circ$ , i.e. perpendicular to the grating plane.

The work is mainly concerned with beam divergence and quantum efficiency. The paper reports achieving a beam divergence of  $17^\circ$  with a 40nm Ag hexagonal grating. The external quantum efficiency was 0.22%, which is lower than the 1.4% of the same LED without the metal film. The quantum efficiency could be improved by adding a photoresist layer, but this increased the beam divergence. This is due to light, which would otherwise be lost to total internal reflection, being extracted into a waveguide mode within the dielectric layer.

The research done above focuses primarily on controlling the beam divergence from a semiconductor device. Surface plasmons can also be of assistance in simply improving the external efficiency of a device. Understanding how to extract more light from organic light-emitting diodes (OLEDs) via surface plasmons modes is very beneficial.

Jelane Vuckovic et al. (79) have looked, both theoretically and experimentally, at how to improve the extraction efficiency of LED devices. They have analysed a structure consisting of a semiconductor layer (thinner than  $\lambda/2$ ) between two metal films. Results show that a well designed periodic pattern in the top semitransparent layer can increase extraction efficiencies to 37%. Both the pitch, and thickness of the grating are important factors in terms of the optical transmission through the metal grating layer (80).

Peter Hobson et al. have addressed the problem of the low external efficiency related to OLEDs by focussing on the losses attributed to surface plasmons coupling. In the paper 'Surface Plasmon Mediated Emission from Organic Light-Emitting Diodes'(81) it is quoted that up to around 40% of the light produced in a typical OLED device may be lost to surface plasmons modes by quenching. (This loss is investigated thoroughly in their paper 'The Role of Surface Plasmons in Organic Light-Emitting Diodes' (82). Their work calculates that ~60% of the light lost to surface plasmons modes could be recovered with the addition of a periodic pattern. By using a 2-D periodic structure, of the correct grating pitch, these surface plasmons modes can be emitted as photons.

## **2 Experimental Techniques**

Coupling between surface plasmons and photons occurs at well defined angles. It is important to be able to accurately measure this angle to understand the behaviour of the surface plasmons within the device.

### **2.1 *Optical Power versus Emission Angle***

As with typical Surface Plasmon Resonance (SPR) experiments it is important to have an accurate representation of how the optical power is absorbed, or emitted, as a function of angle. In typical SPR experiments you would expect to see an absorption dip where the incoming light has coupled with the surface plasmon instead of reflecting onto the detector. In this work we will generally be looking at the emission from the device and therefore we would expect peaks of optical intensity at particular angles. Conversely the absorption of the device could be measured, which would provide the same information. Measuring optical emission is easier experimentally as there are fewer alignment issues. The problems arise when trying to focus incident light onto a small area, as the device can be very slightly off axis which would affect the results as the device is rotated. It is easier to collect the emitted light by rotating a detector around the device (83).

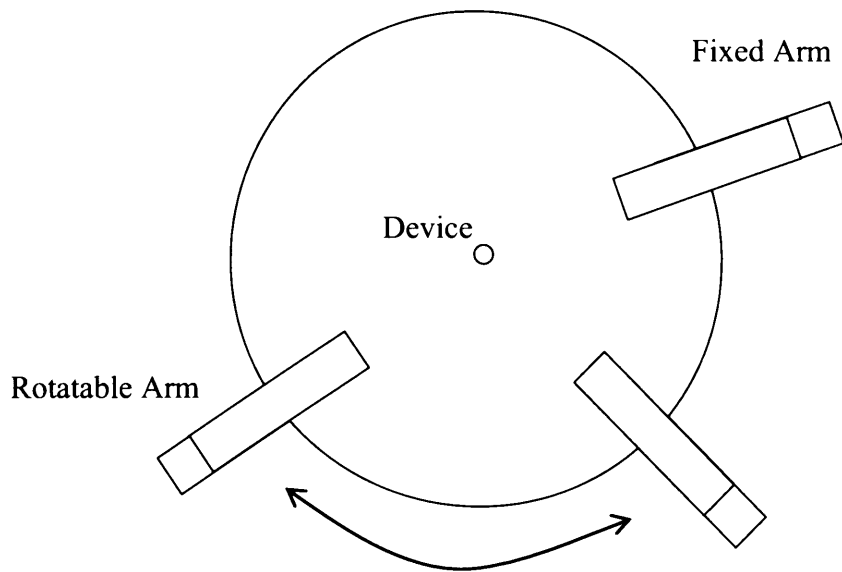


**Figure 17: Diagram of rotational mount designed to record the optical emission and absorption of the device.**

Figure 17 shows how the emission from the device was measured. The device was positioned in the centre of the rotation stage and two arms, one of which had free rotational movement whilst the other is fixed, are aligned towards the axial centre of the central mount. The central mount, where the device is placed, has xyz adjustment to ensure that the relevant section of the device (some devices have more than one aperture) lies directly on the axis of rotation.

Whilst one arm is in a fixed position the equipment still allows reflectivity experiments to be conducted as the central mount can rotate about its axis. Therefore you move the device relative to the fixed arm to set the angle and then adjust the freely moving arm accordingly.

The two rotation arms can have polarisers added to the end, this allows for polarisation dependent measurement to be taken. Having a polariser on each arm enables the polarisation of the incident light (in a reflectivity measurement) to be controlled, or alternatively it allows the emission to be recorded at multiple polarisations. This is very useful when working with these devices as the surface

plasmons themselves are highly polarised and thus we would expect the incident, or re-emitted, light to have the same dependence.

At the end of the each rotation arm is a holder for a photodetector. The photodetector has an active area of dimensions 2.5mm by 2.5mm. It is important to obtain results with good angular resolution, to ensure that finer detail in the emission angular profile is seen. The photodetector is a distance 180 mm from the device, which results in an angular resolution of  $0.8^\circ$ . There is however a trade-off between the angular resolution and the optical power that is measured. It would be simple to increase the theoretical angular resolution, but the decrease in optical intensity on the active area would not provide adequate results. A lock-in amplifier, locked to the pulsed power supply driving the device, is used to obtain a good signal and remove unwanted background light.

## **2.2 *Far-field Emission Images***

Although the rotating setup, as described above, is very useful for some measurements it has disadvantages. The main disadvantage being that the emission profile can only be taken in linear arcs across the device's far-field emission profile. This would be acceptable if, or when, the device is only showing effects in one dimension. For example it might be expected that the far field emission profile needs to only be taken in the plane of the grating vector of the nanoscale line grating, but this is not the case. Similarly devices with higher orders of symmetry would have structure in its emission profile not simply in one plane.

To understand the angles of emission from the device we simply need to record its far-field emission. To achieve this we used a CCD camera, and shone the device either straight onto the active area of the camera or used a thin semi-transparent screen. If using a screen the camera would be focussed onto the screen and light incident on one side of the screen, in a darkened room, would be clear on the

reverse side. To take measurements of polarised emission a rotatable polariser can be inserted between the device and the camera, or screen.

As the dimensions of the setup are known the optical intensity can be related to emission angle. When using a screen a simple scale is used to have a record of the dimension of the image, which is needed when analysing images using a computer. If the far-field emission is being recorded directly onto the camera then the angles can be calculated knowing the dimensions of the active array of the CCD (3 mm x 2.5 mm), and the resolution (720 x 576 pixels). Using computer software (such as Origin (84)) linear intensity profiles of the image can be acquired, with similar results to those obtained when using the rotating detector. Therefore a single image is sufficient to acquire a full spatial emission profile. However, there is a trade off with resolution and the far-field emission images are more useful in obtaining general far-field emission patterns rather than high resolution angular measurements.

## 3 Subwavelength-apertured gold grating

### 3.1 Device Design

The initial design chosen to achieve photon-surface-plasmon coupling with a semiconductor device is a hexagonal, or triangular, grating of apertures. That is an array of holes in the metal film on the top surface of the LED. Several previous papers (70)(74)(71)(72) show that light passing through metal holes, of subwavelength dimensions, can be enhanced. Whilst the previous work mainly considers light incident onto a separate metal film there is little reason why the system cannot be combined into one optically emitting device. The main difference is the control of the incident angle on the hole, as with a semiconductor LED, such as the one our film is applied to, there will be a wide spread of incident photon angles. This need not be a negative point as the wide angular spread of incident light could mean that there is a greater opportunity to couple light to surface plasmons and therefore see some evidence of coupling in the emission of the device.

A grating period of 580nm is chosen as to allow the LED emission to couple to the surface plasmon oscillations in the gold grating, and to re-emit into air at near normal. Using equations 1.7 and 1.12 this can be calculated by assuming an emission wavelength of 650nm, which is approximately the peak emission of the AlGaInP/GaInP LED. The dielectric constant of -13.375 for gold (at 650nm) and air ( $\epsilon=1$ ) can be used to calculate the surface plasmon wave-vector. Light within the LED couples to this grating at multiple angles dependent on the order of grating pitch it scatters from.

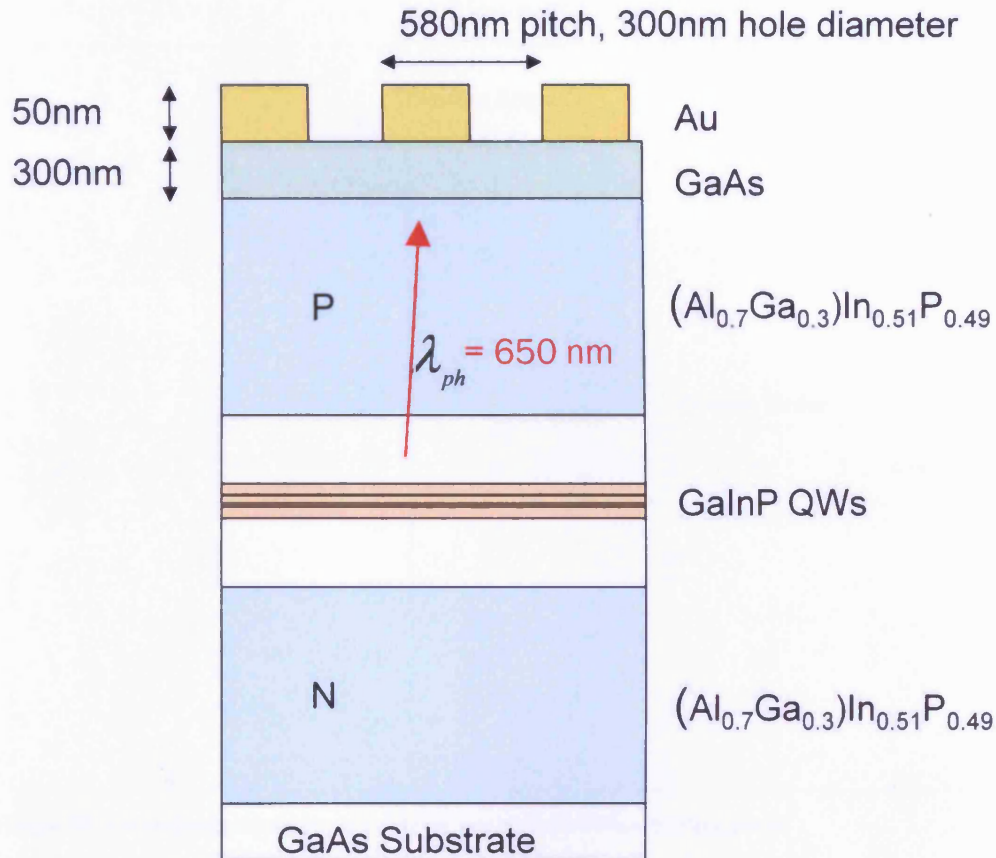


Figure 18: Multiple Quantum Well LED device with the gold grating of apertures. Not to scale.

Figure 18 shows a cross section of the multiple quantum well edge emitting LED with the gold grating applied. The peak wavelength from the three GaInP quantum wells is 650 nm. The structure on the surface of the device was defined using electron-beam lithography on a photo-resist layer which had been spun onto the device. After a 50nm layer of gold was thermally evaporated onto the device, a standard lift-off technique was used to leave a patterned gold film directly on the GaAs cap layer of the semiconductor wafer. The 50nm thickness allows coupling between the GaAs-gold surface plasmon and gold-air surface plasmon. Note that as opposed to some previous work (77), which adds periodicity into the semiconductor material itself, the addition of the gold film grating is a relatively simple process.

Figure 18

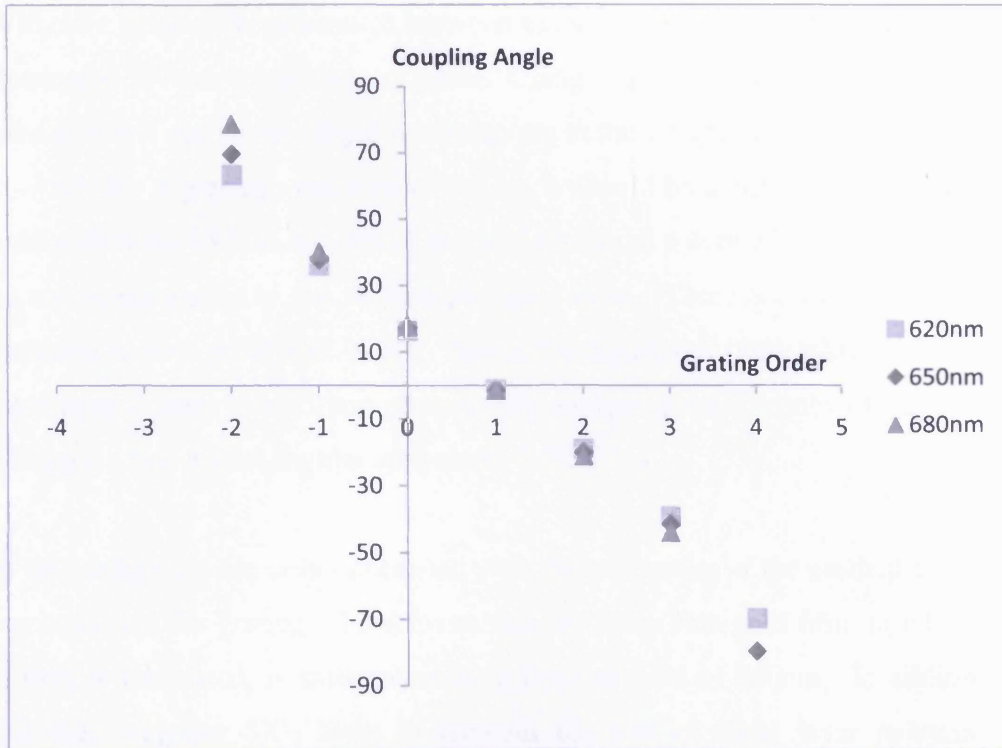


Figure 19: Theoretical calculation of coupling angles for a 580nm grating pitch.

Figure 19 shows how the coupling angle varies at different emission wavelengths. 620nm and 680nm are arbitrary wavelengths chosen near the minimum and maximum of the LED emission curve to show the extent of the angular variation. Grating orders of greater than 5 and less than -2 are of course forbidden as this would require the incident angle to be greater than 90°.

In the above calculation it is the surface plasmon at the air-gold interface that is being considered. Using equation 1.7 we can calculate the surface plasmon at the interface between the gold film and the top semiconductor layer. Coupling to this surface plasmon would require a grating period of around 50-75nm. In addition to this being a smaller feature size, and therefore more difficult to produce, it would also only allow coupling from an interaction with a single grating pitch which would be less efficient. The film thickness is chosen at 50nm as this appears to be an optimum value to ensure that the evanescent fields of the photons incident on the gold film can interact with surface plasmons at the air-gold interface (60)(85)(86).

The grating is required for the surface plasmon to re-emit as a photon into air. Without a grating the mis-match between the wave-vector of surface plasmon and free-space photon would be too great. Using the same equations as have been used above it can be calculated that coupling at the air-gold interface would occur at  $-4.65^\circ$  for a grating vector order of -1. It should be mentioned briefly that as light within the LED is not hitting the gold film from a defined direction there will be no directionality to the surface plasmon wave. Therefore we should expect emission at both  $4.65^\circ$  and  $-4.65^\circ$ . Again this figure has been achieved by using the values related to a 650nm photon. By analysing wavelengths of 620nm and 680nm we find a total angular spread of  $\sim 0.5^\circ$ .

In this design we are only concerned with the properties of the emitted light that has come via the grating. To achieve this the 50nm thin gold film, in which the grating is fabricated, is surrounded by a layer of gold of 300nm. In addition to this the insulating  $\text{SiO}_2$  layer underneath the contact metal layer restricts the current injection to the  $20\mu\text{m}$  square emission window. Figure 20 and Figure 21 show SEM images at different scales. In Figure 20 the  $20\mu\text{m}$  emission window is clearly seen surrounded by the thicker gold contact layer. The hexagonal grating can be seen in Figure 21 using a smaller scale.

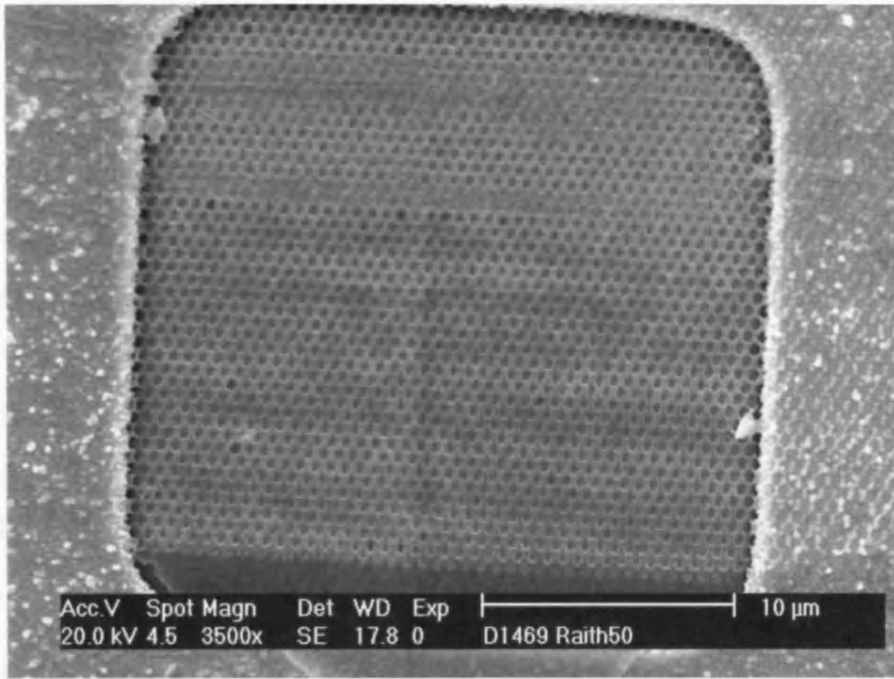


Figure 20: SEM image of the 50nm gold grating on the top surface of the LED.

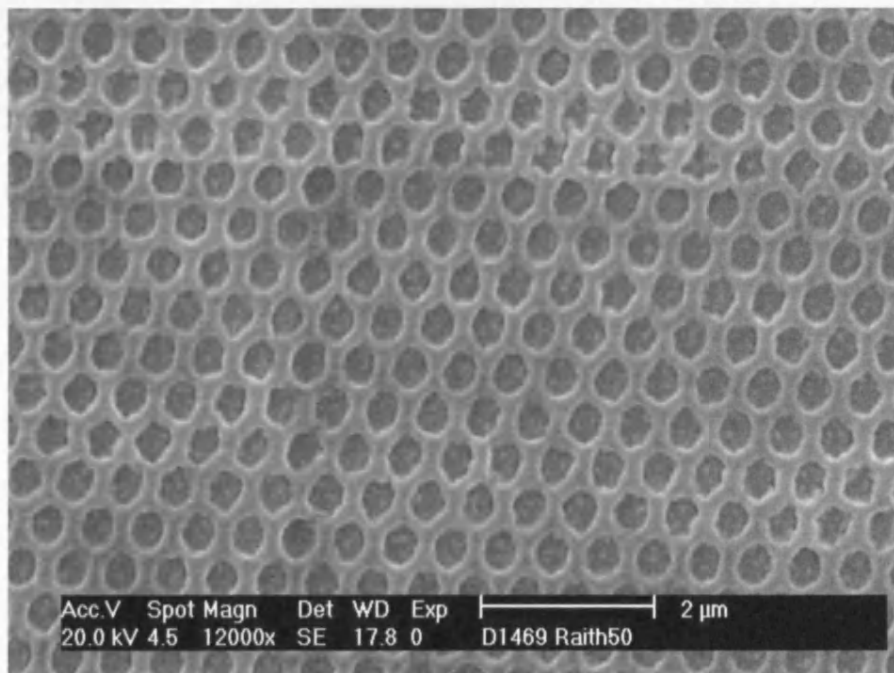


Figure 21: SEM image of the emission window, hexagonal grating clearly visible.

### 3.2 Far-field Emission Images

The first measurement to be taken of this device is an image of the far-field. This gives a quick and simple analysis of the far-field and it should show whether there are any significant effects of the addition of the grating. Using the setup described in chapter 2 the device was shone onto a screen, and, using a monochromatic CCD camera, a far-field image was captured.

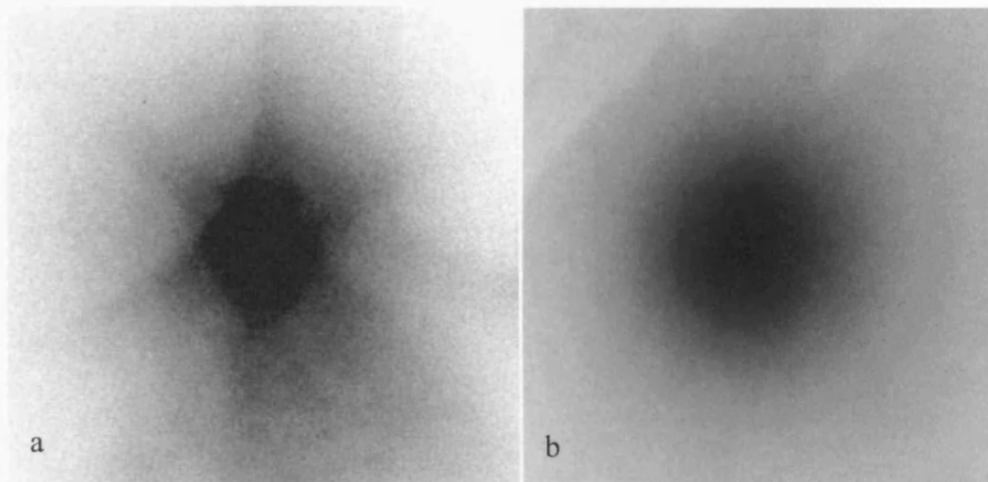


Figure 22: Inverted images of the far-field emission at a distance of 12mm from (a) hexagonal grating device with apertures (b) reference device. Images correspond to an area of 1cm by 1cm.

With a drive current at 25mA the image shown in Figure 22a was captured. From this image it can be seen that there is clearly some geometric pattern to the far-field emission. The reference device is an identical semiconductor device which also has a 20 $\mu$ m square window within a 300nm contact layer, however there is no thin gold film grating within this emission window. When compared to the reference device, in Figure 22 the pattern becomes very apparent. Note that the distance between the device and screen in this image was 12mm, chosen simply as it gave the best image on the CCD camera. By eye the emission pattern was very clear at both longer and shorter distances.

From inspection of the far field image one could recognise that there is roughly 6-fold rotational symmetry. There seem to be three planes of emission at higher angles (when compared to the reference device), each separated by 120°. This is

encouraging as the order of symmetry is identical to that of the hexagonal (or triangular) grating and therefore suggests that the changes in far-field emission are due to the presence of the gold grating.

As surface-plasmons are p-polarised we would expect to see some polarisation effects within the emission from the device. To test this a thin film polariser is placed between the device and the screen. If we define the top layer of the device to be in the x-y plane then the thin polariser is able to be rotated around the z axis. Figure 23 shows that there is very little change in optical power at various polarisations. However, on inspecting the far-field image, rotating the polariser isolates pairs of curved lines.

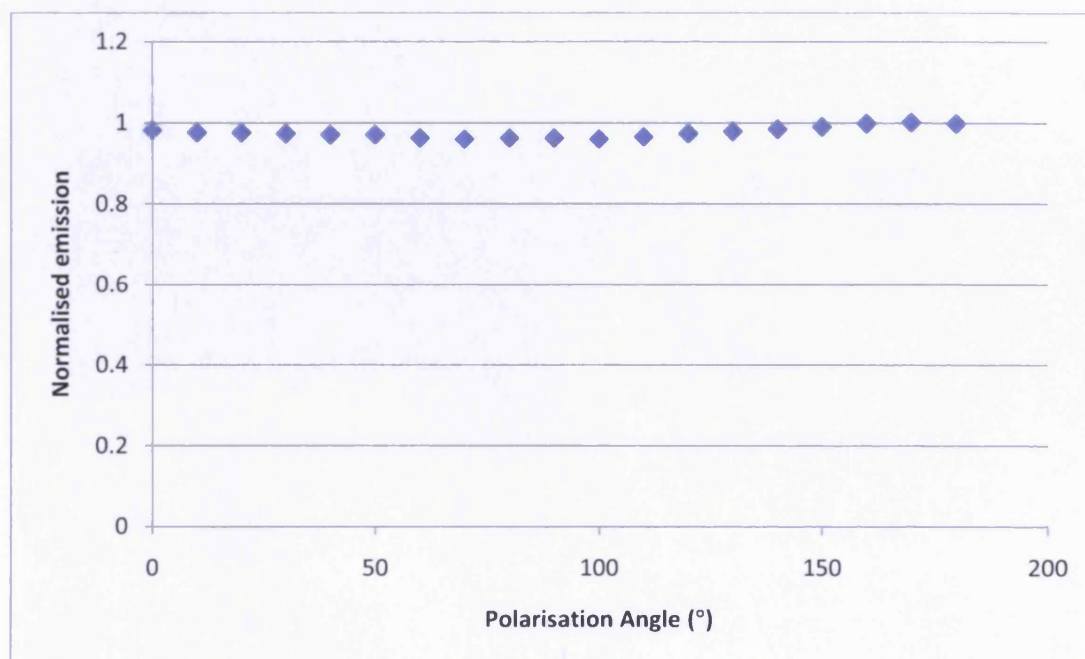
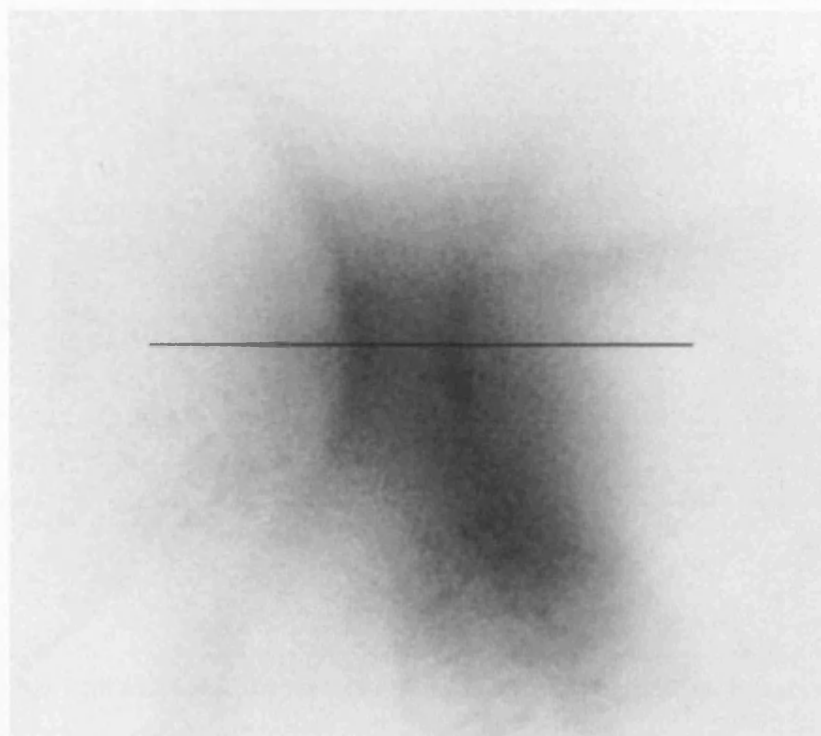


Figure 23: Emission from hexagonal device as a function of polarisation angle.

The pairs of lines are isolated every 60° turned. From rotating the polariser it is clear that the structure in the non-polarised far-field image is constructed from three pairs of these lines. An image of a pair of emission curves can be seen in Figure 24. From this image it should also be noted that there is still a typical Gaussian LED emission as the background to these curves. This is believed to be

simply emission, of the correct orientation to pass the polariser, that passes through the grating without interaction.



**Figure 24: A pair of emission lines isolated using a polariser. The horizontal black line represents the axis of relative polarisation of the polariser.**

In Figure 24 the black line shows not only the axis of the polariser, but also lies parallel to the grating vector. By considering this 2-D plane we can refer to the equations 1.7 and 1.12. The equations allow us to calculate the plasmon to photon coupling angle for a specific grating pitch, wavelength and material interface. We can analyse the image shown in Figure 24, along the plane defined by the grating vector and polarisation axis, as the dimensions are all known. An angle of  $\pm 4.9^\circ$  from perpendicular is calculated as the angle from the surface normal where the centre of the emission curves cross the black line.

Using the experimental setup as described previously in chapter 2.1 the optical emission as a function of angle can be calculated. The results, as shown in Figure 25, can be seen as the equivalent of an intensity profile along the black line in Figure 24. Using this method, with measurements taken every  $1^\circ$  interval, the

maximum emission is found to be at 5°. This is in close agreement with the 4.9° measured using the far-field image and the calculated value of 4.65°.

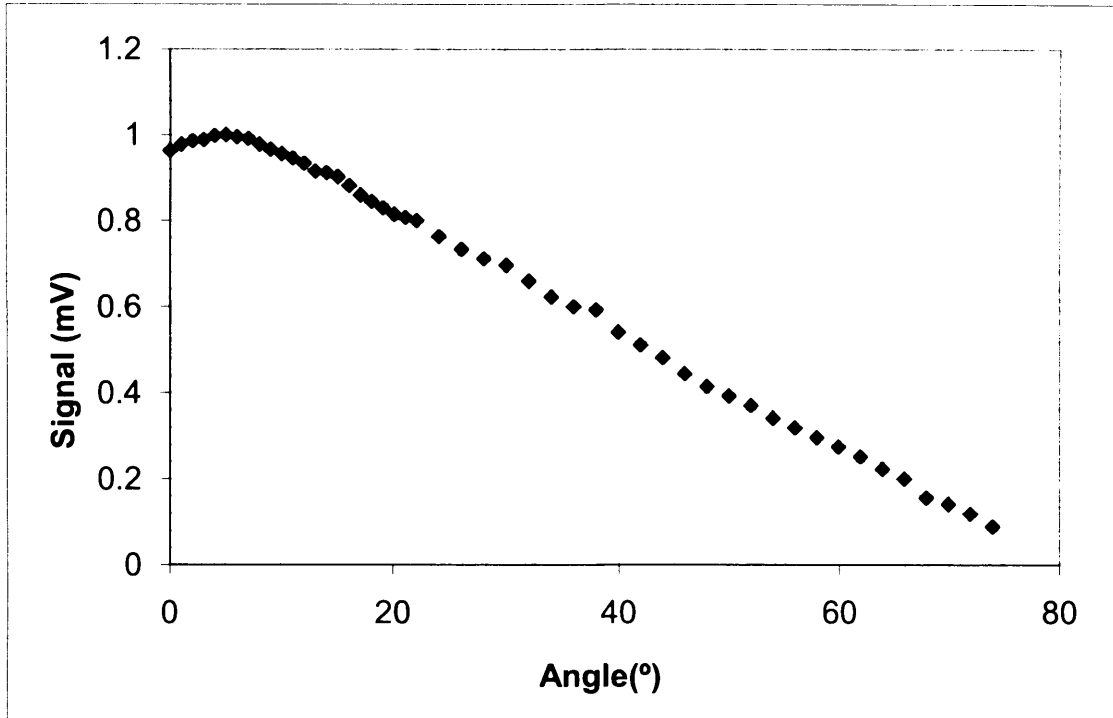


Figure 25: Emission profile through a pair of emission curves along the axis of polarisation.

Due to the symmetry of the grating/device, the measurements taken in Figure 25 could be reflected about 0° to gain a full profile.

### 3.3 Analysis of Emission Pattern

The hexagonal grating can be approximated by 3 periodic gratings of apertures, each at 120° to each other. This can be clearly seen in Figure 21. To understand the curvature of the emission curve it is beneficial to deal with the single 1-D grating related to a pair of curves. We must also define a new angle,  $\alpha$ , shown in Figure 26, which is the angle between the emitted light and the grating wave-vector.

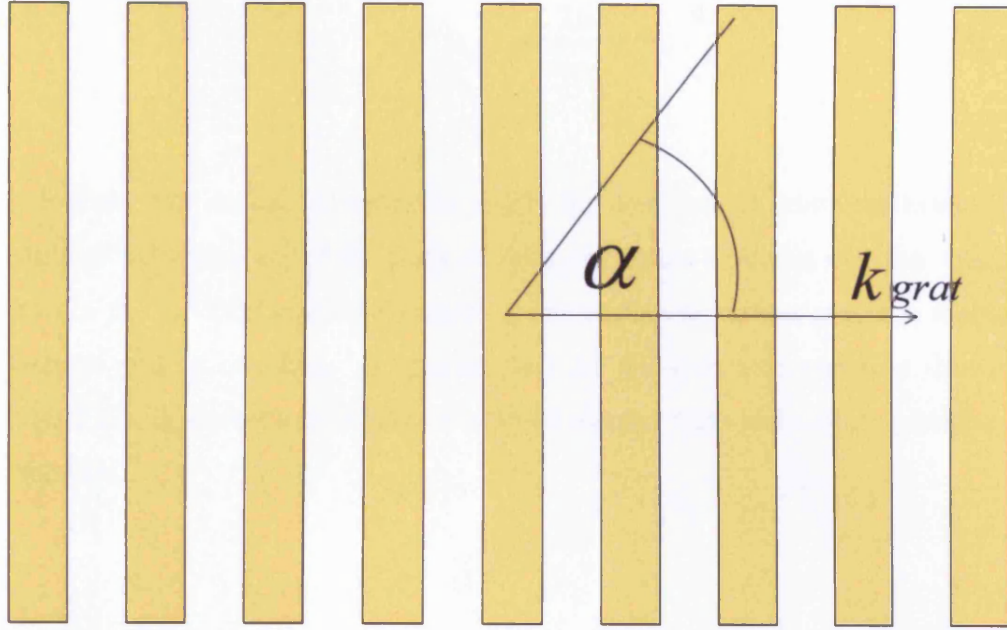


Figure 26: Representation of a single grating within the hexagonal grating.

In a 2-D system for coupling to occur it can be said that

$$k_{sp} = k_{ph} \sin \theta + N \cdot k_{grat} \quad (4.1)$$

Where  $k_{sp}$ ,  $k_{ph}$  and  $k_{grat}$  are the wave vectors of the surface plasmon, photon and grating respectively (as previously defined).  $\theta$  is the emission, or coupling, angle of the emitted or incident photon.

In the case shown in Figure 26 we can define  $\Lambda_{eff}$  which is the effective grating pitch that light, at an angle  $\alpha$  to  $k_{grat}$ , experiences. Therefore

$$\Lambda_{eff} = \frac{\Lambda_{grat}}{\cos \alpha} \quad (4.2)$$

Clearly as  $\alpha$  increases the effective grating,  $\Lambda_{eff}$ , increases.

It could be said that in general

$$k_{sp} = k_{ph} \sin \theta + N \cdot k_{eff} \quad (4.3)$$

Where

$$k_{eff} = \frac{2\pi}{\Lambda_{eff}} \quad (4.4)$$

It follows that as  $k_{eff}$  decreases the angle for coupling,  $\Theta$ , must increase. This explains the curvature of the pairs of lines and offers evidence that the structure seen in the far-field emission images is indeed due to surface plasmon emission through grating coupling. It appears that the non-polarised emission shown in Figure 22a is a combination of both non-interacting light and surface plasmon re-emission.

### **3.4 Emission Spectra**

Despite having some understanding as to the origin of spatial emission of the device it is very important to understand the spectral emission. Obtaining emission spectra from a device is very useful in understanding the interactions from an energy perspective. Due to the angular emission profile from the hexagonal grating device it is important to obtain spectral profiles at relevant points within the far-field.

Using a typical spectrometer the emission spectrum of the reference device was taken, as shown in Figure 27. This is clearly important in terms of seeing the changes that the presence of the gold film grating makes.

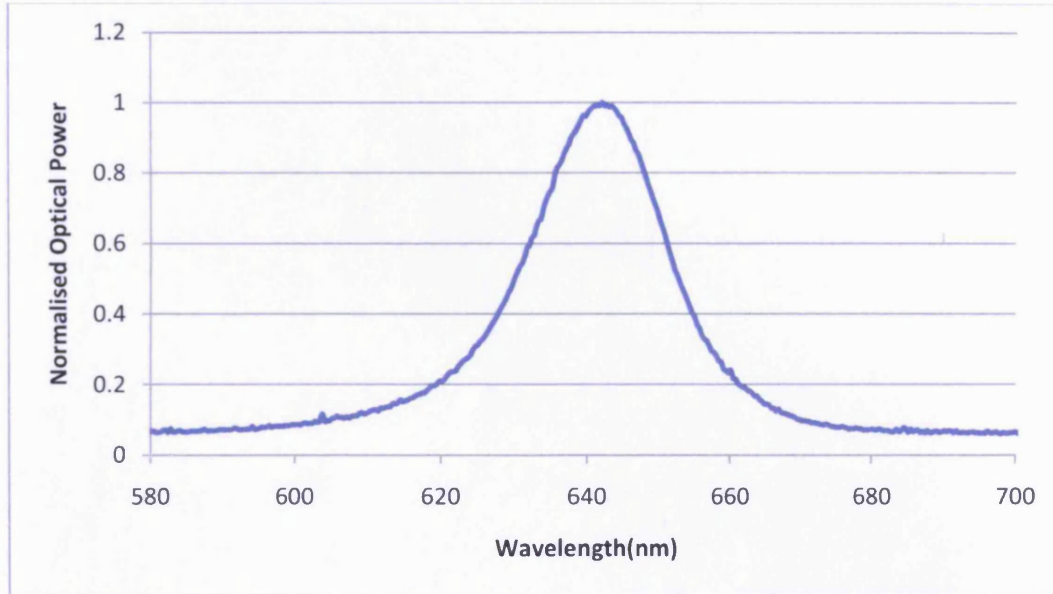


**Figure 27: Emission spectrum from the reference device operated at with a drive current of 35mA.**

Figure 27 shows a peak wavelength of 643nm and a typical broad spectrum. To compare the hexagonal grating device to the reference device we need to specify what part of the emission we want to collect light from. To achieve this a circular aperture of 2mm is mounted directly in front of the input slit of the spectrometer. This allows us to study the changes in spectrum at various points along the strong emission curves with the far-field spectrum. Figure 28 shows a representation of a pair of emission curves from the device. On this diagram there are 4 points marked A, B, C and D, each of which represent a part of the far-field pattern where an emission spectrum has been taken.

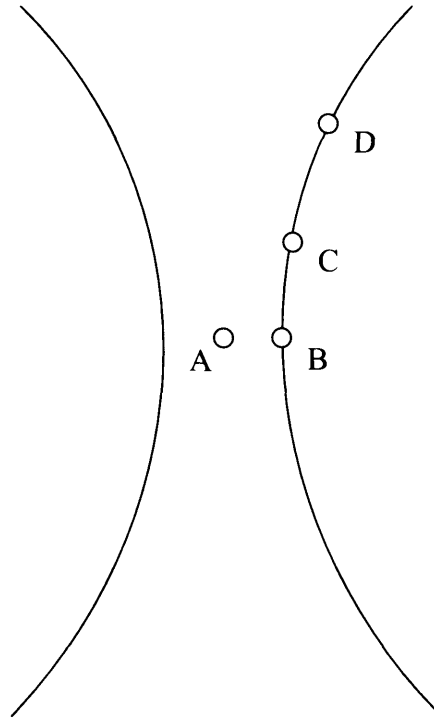


**Figure 28: Schematic diagram of a pair of emission curves. A, B, C and D represent points where spectra have been taken.**

The device is a distance of 11cm from the screen in which the circular aperture is made, therefore the angular resolution of these measurements can be calculated. The 2mm aperture at point A provides an angular collection cone of  $0.52^\circ$  from normal. Therefore, along a single axis, this is a total angle of  $1.04^\circ$ . Points B, C and D are  $4.9^\circ$ ,  $10^\circ$  and  $20^\circ$  from normal respectively. As the emission angle from normal increases, the capture angle from the device decreases. This is simply due to the distance from the device to the aperture increasing. At a distance of 11cm the divergence of the pattern's emission lines is large enough to fully cover the 2mm aperture. Therefore it is certain that all light being captured is from what we have referred to as the far-field emission curves.

It is thought that the far-field emission pattern is constructed from the strong emission curves, attributed to surface plasmon emission, and photons which pass through the grating without any plasmonic interaction. Therefore it is reasonable to expect that the optical spectrum taken at point A would be similar to that of the reference device. Figure 29 shows normalised spectra of both the reference

device and at point A (see Figure 28) of the hexagonal device. While the peak wavelength is of approximately the same value, 643nm, there is a clear difference in the emission curve. There is an approximate doubling of the FWHM in the spectra taken at point A relative to the reference device. Despite using a polariser to correctly align the emission curves there is no polariser used in these spectra.

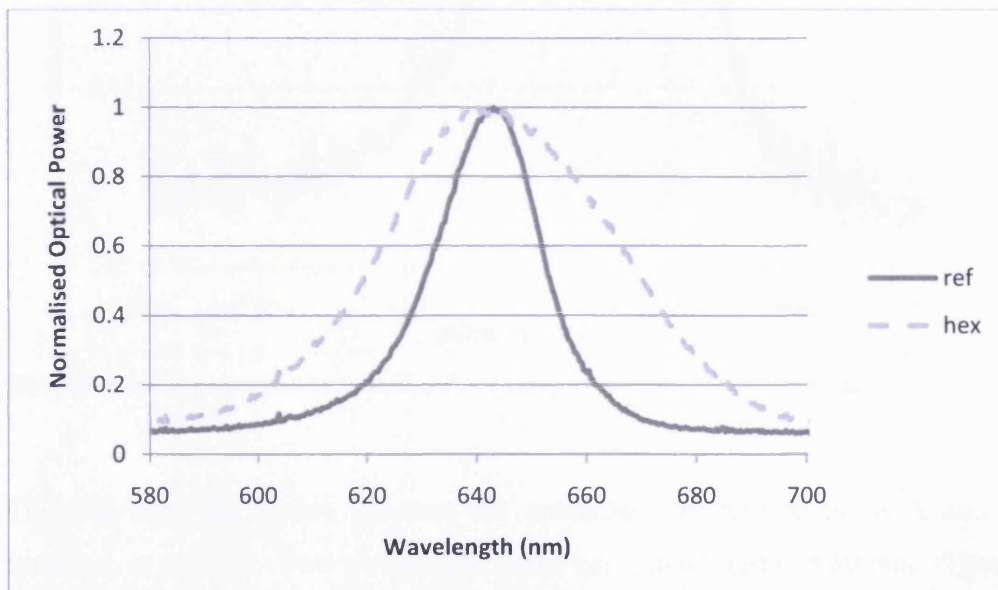


Figure 29: Comparison of the emission spectra of the reference device to that of the hexagonal grating device at point A.

Point B is the nearest point on the emission curve to A. A line from point A to B would be parallel to the grating vector and therefore corresponds to the minimum emission angle of  $4.9^\circ$  (as calculated previously). The emission spectrum at point B can be seen in Figure 30.

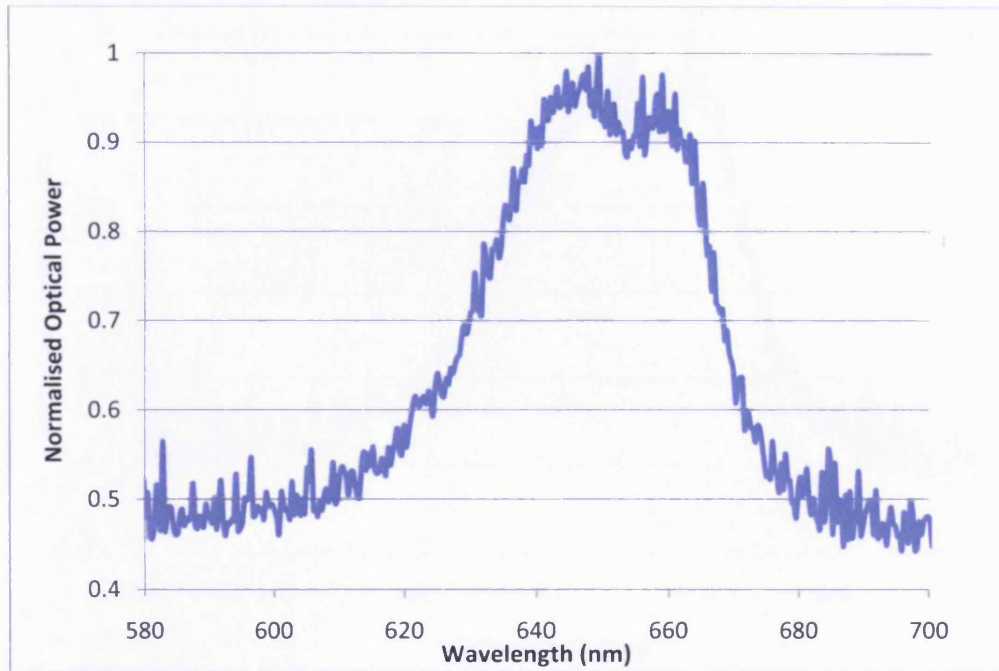


Figure 30: Emission spectrum at point B, isolated using an aperture of 2mm diameter.

There is clear difference between the emission spectrum at point A and the spectrum at point B. Two wavelength peaks exist, at 646nm and 600nm. There is an increase in the emission of light between the wavelengths of 654nm and approximately 670nm. On first inspection it appears that this spectrum is the same as that of Point A, but with the addition of another, relatively broad, emission mechanism. The addition of a polariser, set at a polarisation angle to isolate the relevant emission pattern, results in an identical normalised spectrum but due to the lower intensity there is an increase in noise and for this reason it is not shown here.

Normalised emission spectra taken at points C and D are shown in Figure 31 and Figure 32 respectively.

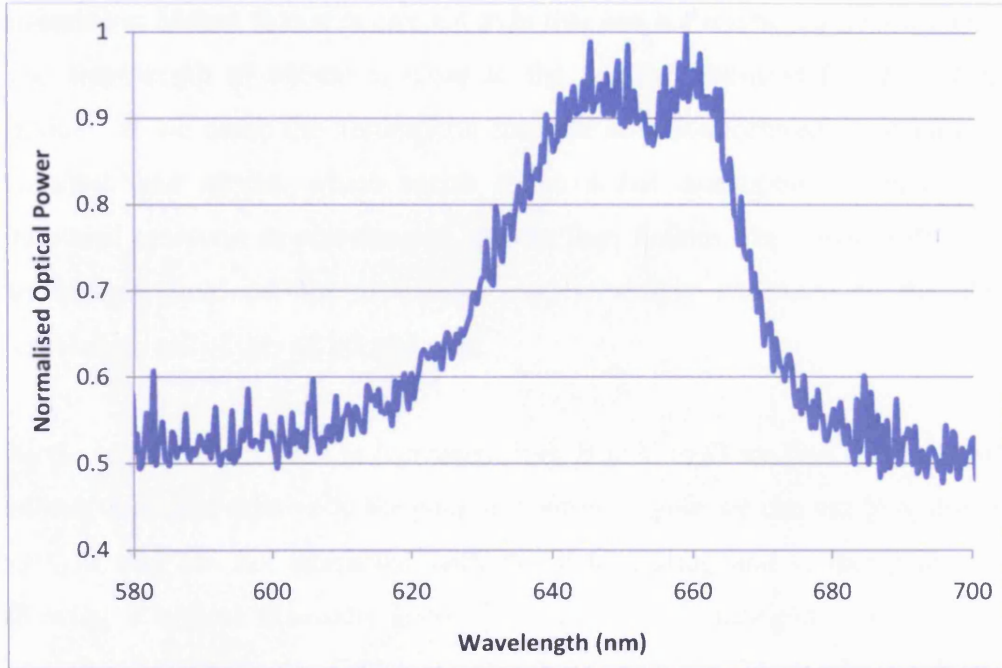


Figure 31: Emission spectrum at point C, isolated using an aperture of 2mm diameter.

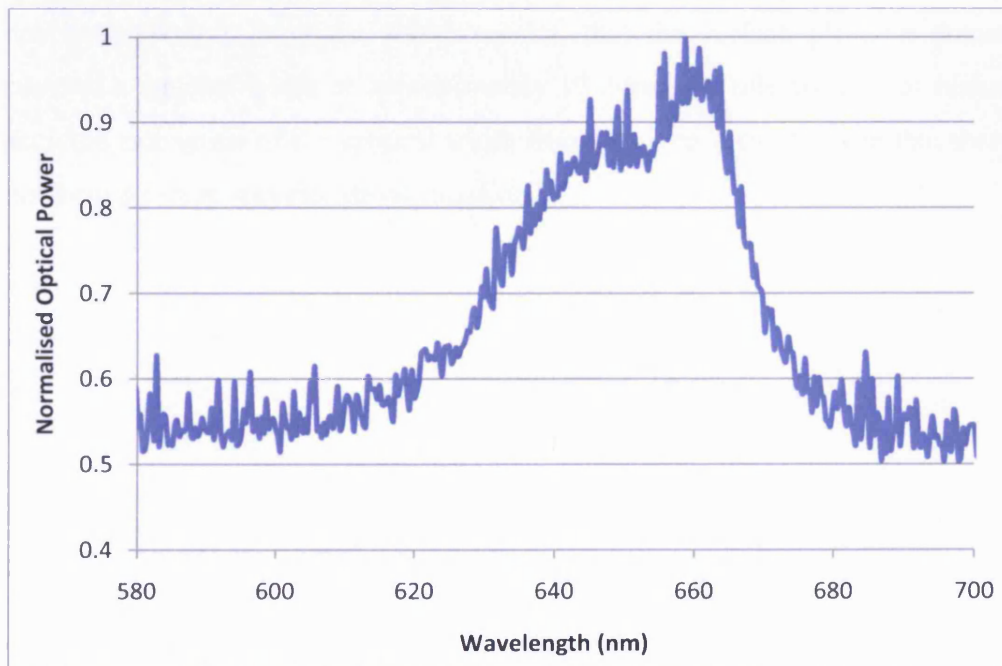


Figure 32: Emission spectrum at point D, isolated using an aperture of 2mm diameter.

In both Figure 31 and Figure 32 we see the presence of two emission peaks. Again they are both found to be at 646nm and 660nm. We can attribute the

emission at 646nm to that of emitted light that has not interacted with the grating. The wavelength of 646nm is close to the 643nm measured for the reference device. If we make the assumption that the emission centred at 660nm has a Gaussian like spread, which seems to be a fair assumption considering the increased emission at wavelengths greater than 660nm, the small shift in peak wavelength from 643nm to 646nm can be simply attributed to the shorter wavelength tail of this additional peak.

As the angle from normal is increased from B to C to D we find that the peak at 646nm decreases relative to the peak at 660nm. Again we can attribute this peak to light that has not interacted with the gold grating and is therefore simply showing a typical Gaussian intensity profile in the far-field. As the strong emission lines in the far-field image (such as in Figure 24) can be attributed to surface plasmon emission and the spectral peak at 660nm is only present in light directed into these emission curves then it can be said that the surface plasmon emission from the device is centred on a wavelength of 660nm. Furthermore it can be estimated, from the above spectra, that the surface plasmon emission covered a spectral width of approximately 10-30nm. While we cannot make an accurate estimation of the spectral width from this data it can be seen that there is not a single sharp wavelength of emission.

## 4 Periodic gold film

In the previous chapter we see that surface plasmon emission has been achieved from the application of an apertured gold film which has been integrated onto the top surface of an LED. The results suggest that the emission from the device is a mix of surface plasmon re-emission and light that has passed through the apertures without any interaction. Ideally we would like to achieve a device that has solely surface plasmon emission, or at least a reduction in the light that passes through the 20 $\mu\text{m}$  emission window without any form of interaction. Theory suggests that internal coupling to the surface plasmon (at the gold-air interface) can occur via the decaying evanescent electric field from the internal GaAs-gold interface of the semiconductor. Therefore if we removed the apertures from the top surface there would still be photon-surface plasmon coupling and hence external surface plasmon re-emission. However, with the removal of apertures we are left with simply a 50nm flat film and therefore no mechanism for coupling due to the difference between wave-vectors of the surface plasmon and free-space photon. It has been shown that there simply has to be some periodicity in the gold film in order to satisfy the coupling equations 1.12 (87). While it does not necessarily need to be periodicity of a constant pitch, for example methods where annealing of the gold film causes surface roughness, which allows coupling to surface plasmons (2), it is far simpler to have a fixed grating period.

To achieve periodicity in the gold film the top surface of the semiconductor was initially patterned with SiO<sub>2</sub> of 30nm thickness. The gold film of 50nm thickness was then evaporated over the SiO<sub>2</sub> pattern. A cross section of a linear grating can be seen in Figure 33. Again this thin gold film is deposited with a square 'emission window' of 20  $\mu\text{m}$ .

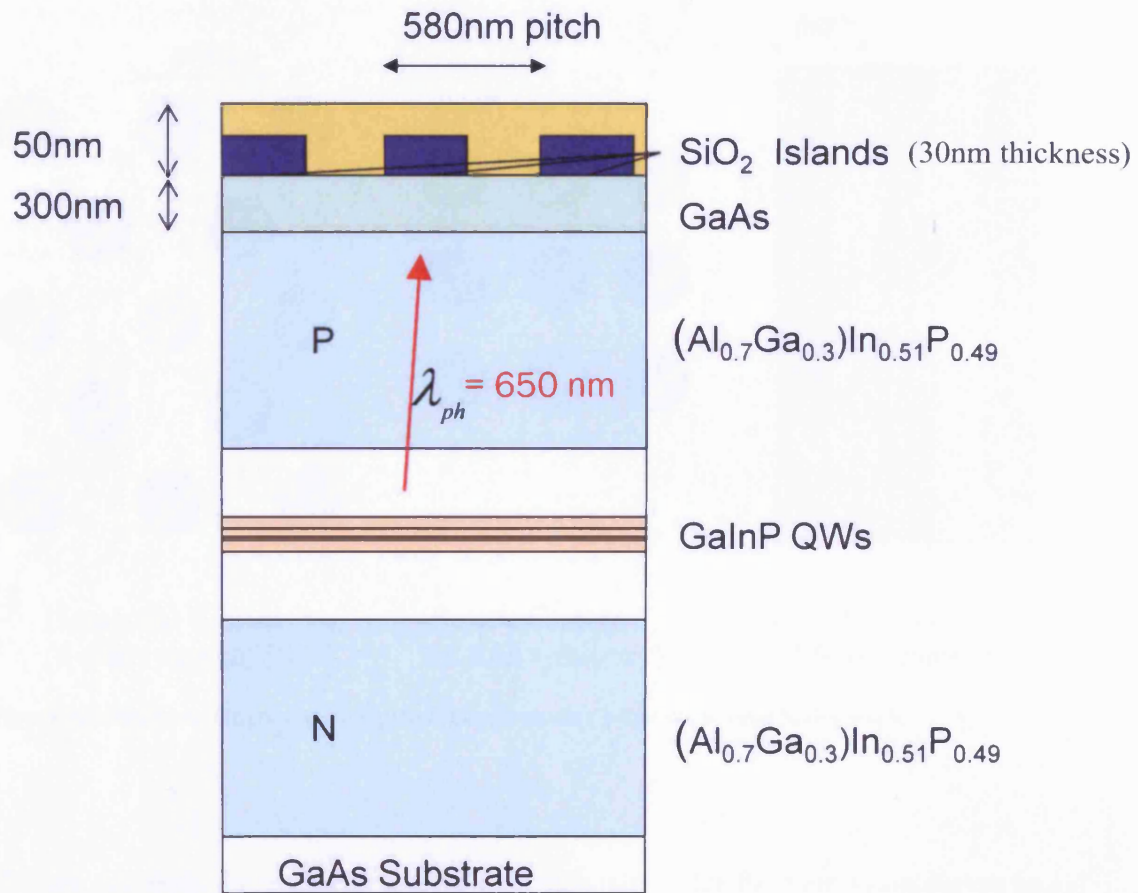
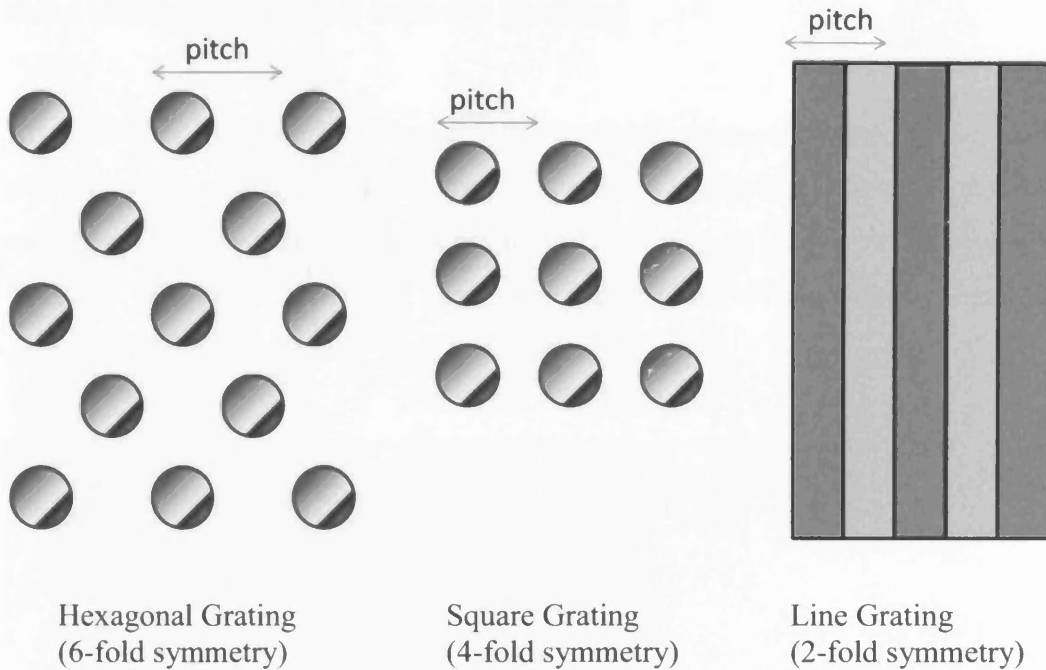


Figure 33: AlGaInP/GaInP Multiple quantum well LED with a gold film with periodicity of 580 nm due to SiO<sub>2</sub> gold islands.

In this section we fabricate gratings with 6 fold, 4 fold and 2 fold symmetry, which we refer to as the hexagonal, square and linear (or line) gratings respectively. These grating designs can be seen in Figure 34.



**Figure 34: Schematic diagram showing the different grating orientations used in this work.**

We can see from the previous chapter that each pair of far field emission curves is related to a single direction of the grating vector. To understand the coupling between photon and surface plasmons it is beneficial to use a linear grating as it simplifies the far-field emission pattern. In essence the linear grating is the most basic of grating patterns and it is worthwhile focussing on it as it will allow easier analysis of the surface plasmon interaction and allow the possibility of more complex device designs in the future.

## 4.1 Hexagonal and square grating

As shown in the previous chapter, the far-field emission of the devices can provide useful information about how the device is operating. Again the devices are shone directly onto a monochromatic CCD camera and their images are recorded. Figure 35 shows the hexagonal device being driven with a current of 22mA at a distance of 11mm from the camera.

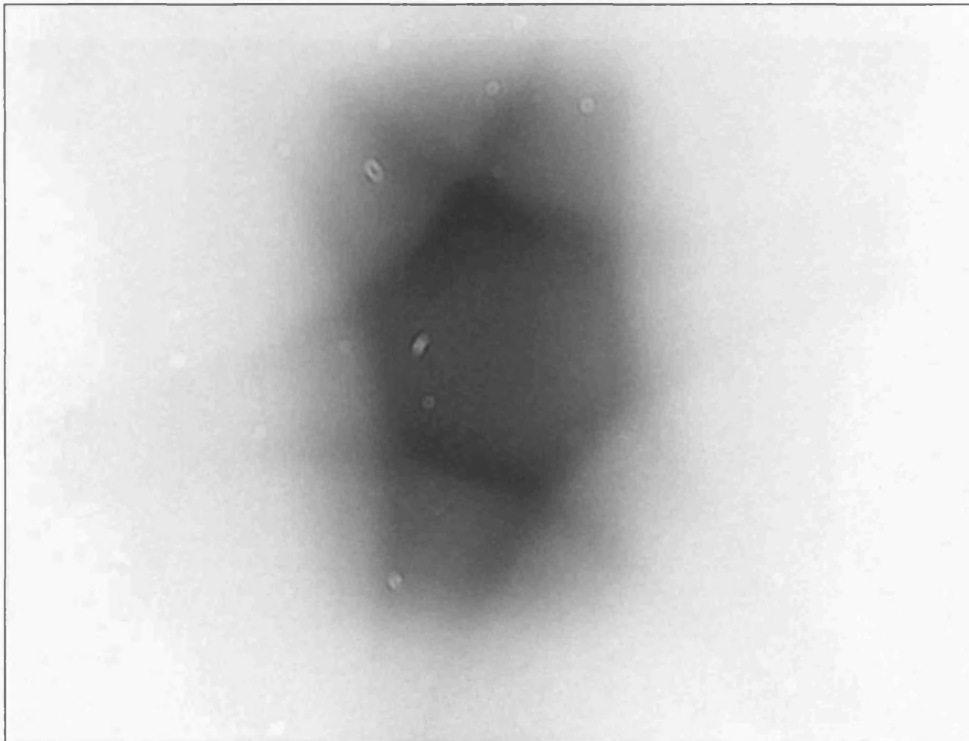


**Figure 35: Far-field image from a device with a hexagonal periodic grating.**

When compared against Figure 22 it is very clear that in this device the strong emission lines are more apparent. This is of course due to there not being any apertures in this device. At 50nm the gold film is thin enough to allow some light to pass through, however, relative to the device with apertures, it has been substantially reduced. In Figure 35 the emission can be seen to be constructed from 3 pairs of strong emission curves. The far-field profile may look different to that of Figure 22 but that is simply due to the scale. Knowing the distance from the device, the size of the active area of the CCD camera and its resolution, the minimum angle of emission from normal can be calculated to be  $5.2^\circ$ . This is a

close match to the angle calculated for the device with a grating array of apertures. Due to the angular width of the emission curves, and the resolution of the camera, there will be some error in this measurement.

Similarly Figure 36 shows the far-field emission from the square grating device. Here we see that there are now two axis of symmetry. This is of course due to the design of the grating as both orthogonal grating vectors contribute to a pair of emission curves (as explained in chapter 3).

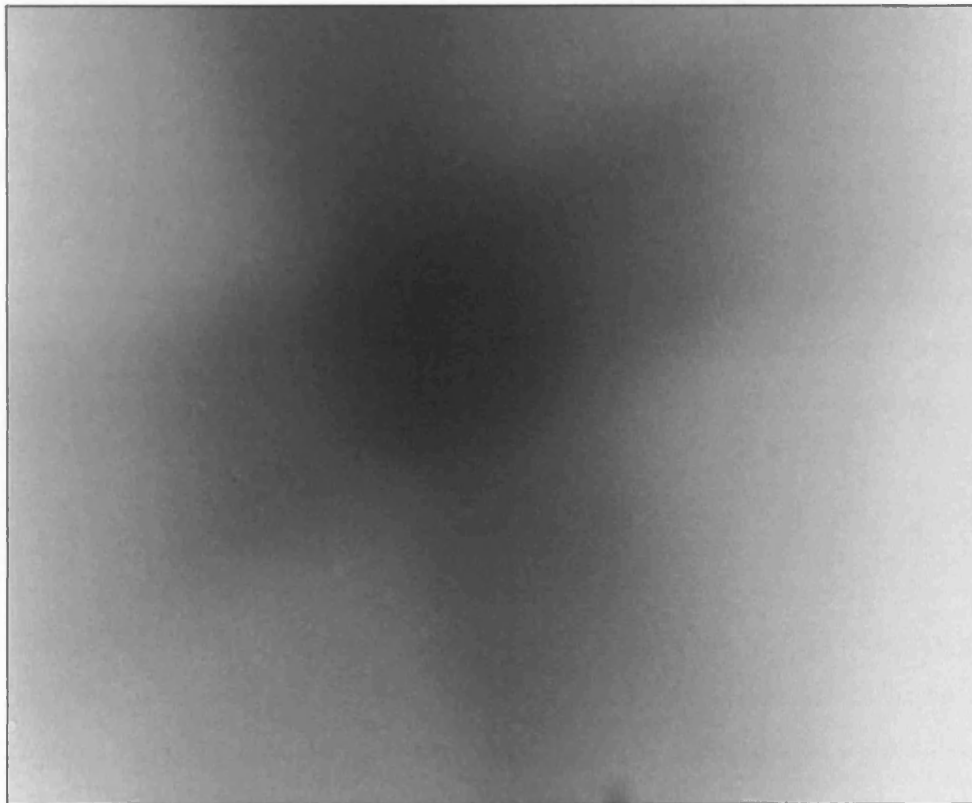


**Figure 36: Far-field image from a device with a square periodic grating.**

### **4.3 1-D Grating**

The film with linear periodicity provides the clearest opportunity to take measurements. A single grating vector results in a single pair of emission curves. This is useful for taking profile scans using a photodetector (see chapter 2) as there is no interference from other emission curves. In addition to this the emission along these lines should be of a higher intensity relative to the 'background' emitted light when compared against gratings of a high rotational symmetry. For example, surface plasmons in the gold film of a hexagonal patterned device could re-radiate as a photon relative to three grating axes. Therefore the total optical intensity of all surface plasmon re-radiation is split over 3 pairs of lines. In the linear grating the surface plasmons re-radiate at an angle relative to a single grating vector and the far-field emission pattern is therefore more optically intense. Ideally we would like to have emission from the device as just re-radiation from surface plasmons. This is difficult to achieve as there is a trade-off between having a thin metallic film for coupling to occur and having a thick gold film to prevent light passing through the film without coupling.

#### **4.3.1 Device measurements**

The far-field (Figure 37) is captured using a monochromatic CCD camera as with both the hexagonal and square devices. Visually there does seem to be a high contrast ratio between the emission lines and the 'background' light. Placing a polariser has a large effect on the image, dependent on its angle. When set in the position to allow surface plasmon emission to pass it has little effect except to slightly lower the intensity of the background light.

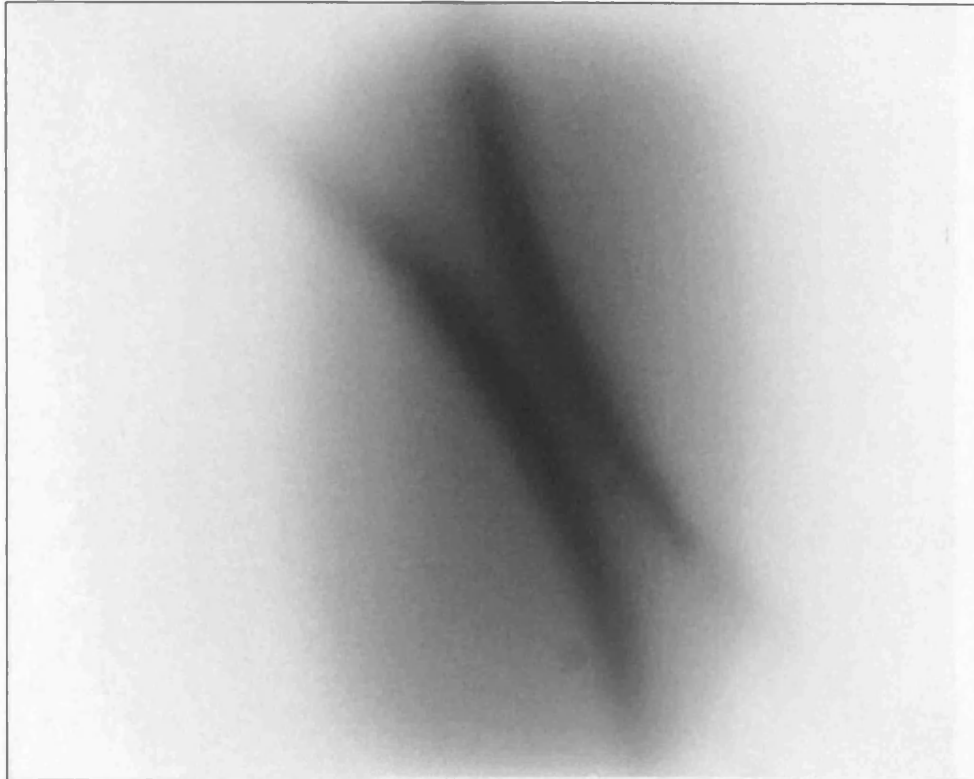


**Figure 37: Far-field image from a device with a periodic line grating.**

However, as shown in Figure 38, when the polariser is rotated  $90^\circ$  from the angle of maximum the pair of emission curves is hugely reduced.

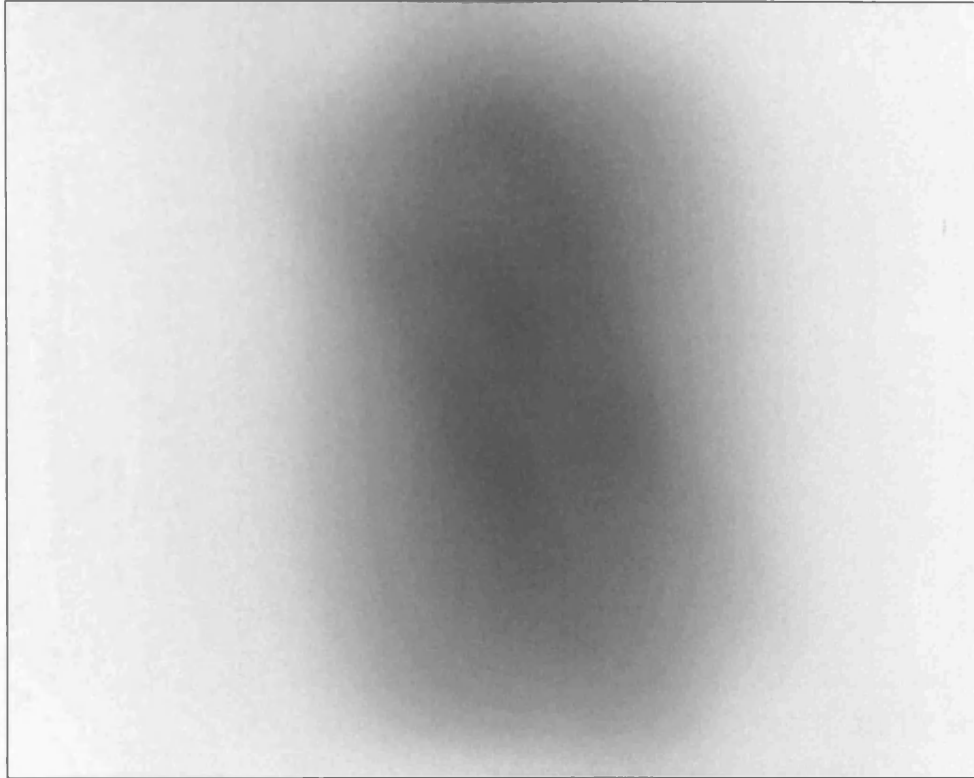


**Figure 38: Far-field image via a polariser from device with a periodic line grating. The polariser is set in a position to prevent the surface plasmon re-emission passing.**

This can be analysed further by measuring the total optical power as a function of polarisation angle. The device was driven with a pulsed current of 24mA and a lens collected all emitted light and directed it to a photodetector which was in turn connected to a lock-in amplifier. The polariser, between the lens and the photodetector, was rotated in  $10^\circ$  steps. The normalised measurements are shown in Figure 39. Steps of  $20^\circ$  were taken after  $180^\circ$  due to the symmetry. It can be seen that there is a large difference between the total optical power at both minimum and maximum powers. Where the pair of emission curves are blocked, where the polariser is set at  $20^\circ$  (or  $200^\circ$ ) the total optical intensity drops to half of the maximum value. As the background light is isotropic, and therefore has the same value of unpolarised light blocked at any given polarisation angle, the surface plasmon re-emission can be attributed to approximately half of the total output intensity from the device.

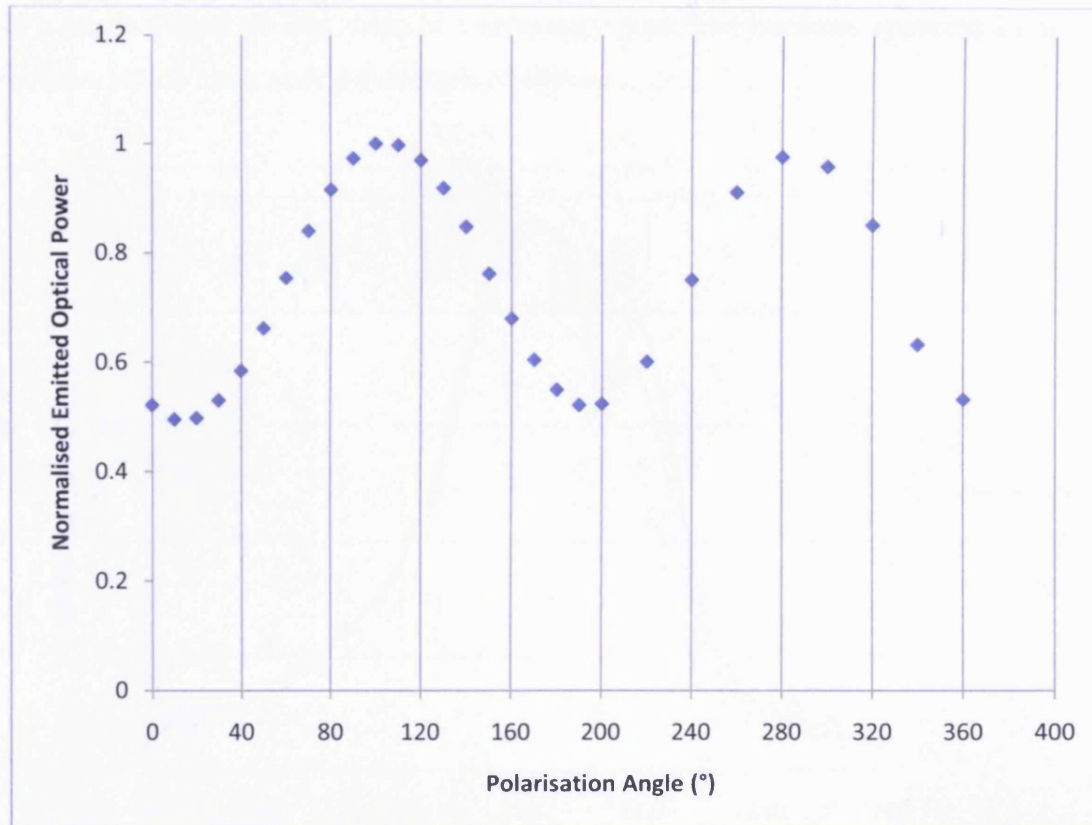


Figure 39: Normalised optical emission from 580nm pitch linear grating via a linear polariser.

We can look at the spectral behaviour of this device. As opposed to chapter 3, where the spectra were analysed at various points in the far-field, the data in Figure 40 have been obtained by collecting the large majority of the light from the device via a lens. The polarisation angles in Figure 40 can be directly compared to that of Figure 39. Spectra have been taken at the angles  $110^\circ$  and  $200^\circ$ , which correspond to a maximum and minimum in total optical power respectively, and at an angle of  $140^\circ$  which is simply a mid-point. Figure 40 shows that again there is a big difference in spectra dependent on the polarisation angle. There are two main situations to consider; one where the surface plasmon emission is able to pass through the polariser and one where the polariser is rotated by  $90^\circ$  and surface plasmon re-emission is not allowed to pass. When the polariser is set at  $200^\circ$ , which corresponds to a far-field image as shown in Figure 38, the resulting spectrum is as we would expect from a device without a gold film layer, with a maximum wavelength of 644nm. Rotating the polariser to  $110^\circ$  (or  $290^\circ$ ) allows the polarised light from the surface plasmons to be collected by the spectrometer.

We see in Figure 40 that there is a secondary peak that becomes apparent from 654nm, which has a peak wavelength of 660nm.

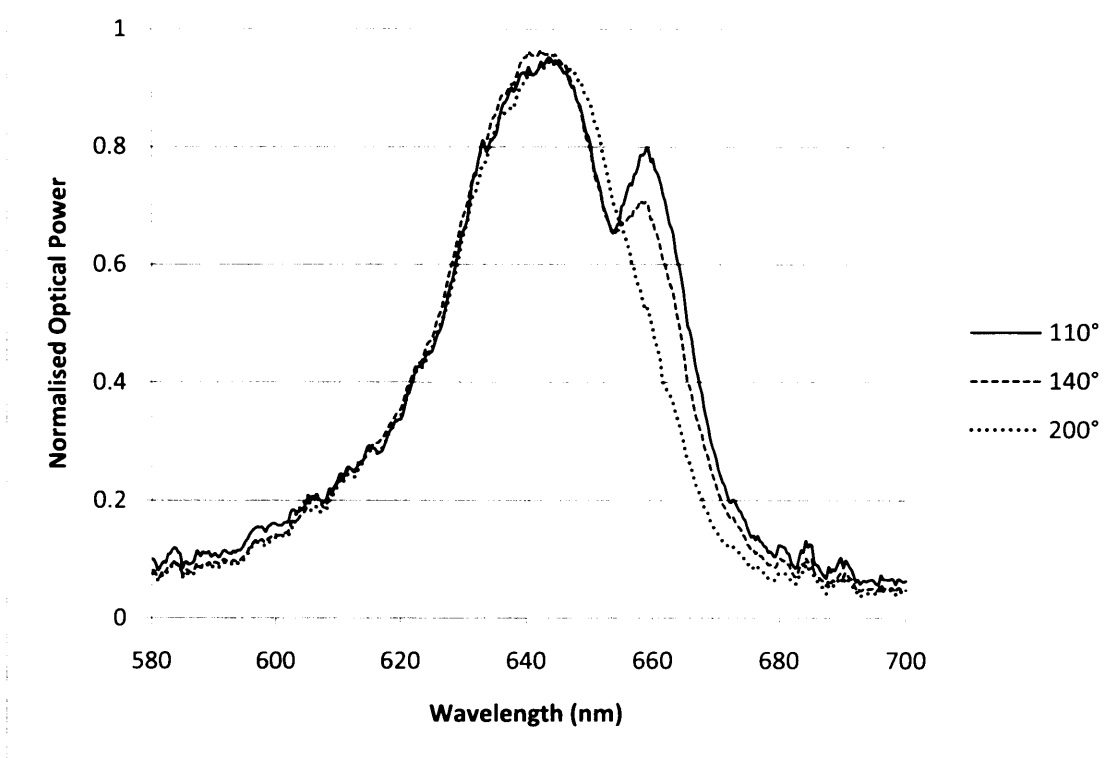


Figure 40: Polarised emission spectra from the line grating device. Polariser was set with angle at 110°, 140° and 200°.

It is worthwhile noting that the polarisation angles used in these measurements are simply the values read from the polariser and are not related to the angle  $\alpha$  which was defined previously (chapter 3) as the angle from the grating vector in the 2-D plane that the top layer of the gold film is parallel with. The angles of the minimum and maximum optical power do not correspond to 0° and 90° on the polariser (which are aligned as vertical and horizontal respectively) simply due to the emission window of the device, and therefore the grating vector, not being aligned to the horizontal. In fact it can be seen in Figure 37 that the device is approximately 20° from vertical. The device mount used in experimental setup prevented an accurate rotational alignment.

The polariser does a far more effective job in isolating surface plasmon emission in the linear grating device than the hexagonal grating. Figure 41 demonstrates

the minimal change in optical power when using the hexagonally grated device. This is due to the higher order of rotational symmetry in the hexagonal device.

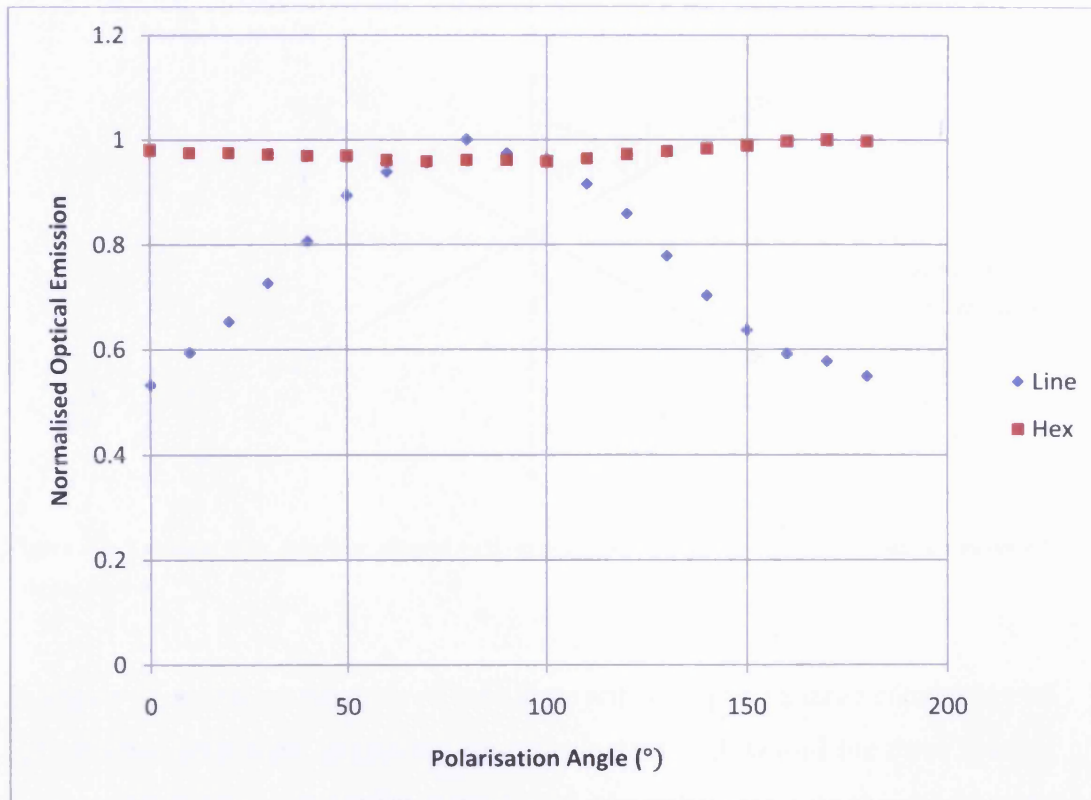
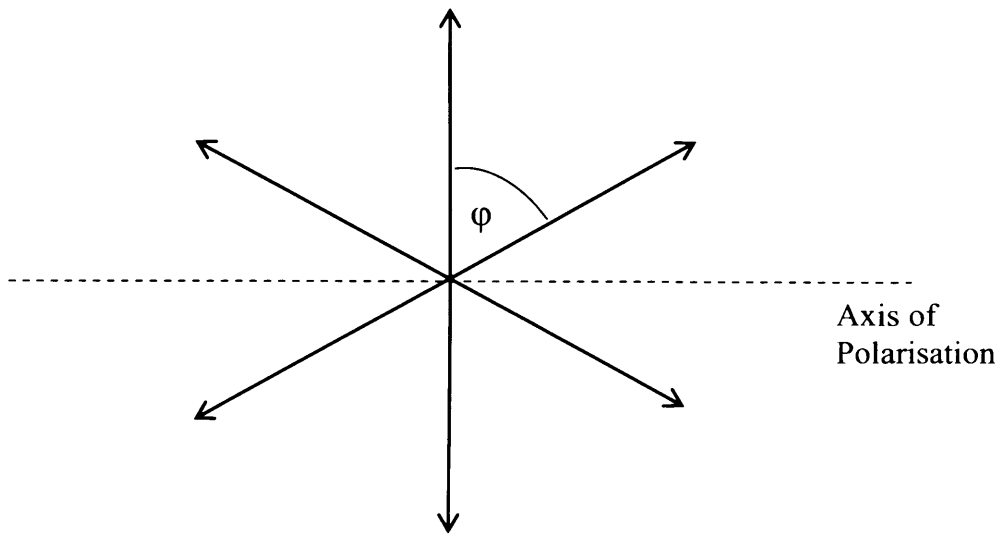


Figure 41: Normalised polarised optical emission from linear grated and hexagonally grated devices.

An angle on the linear polariser which is orthogonal to a single direction of periodicity would remain only  $30^\circ$  from the two other grating vectors (see Figure 42) and therefore a significant amount of light is able to pass through the polariser. The polarisation angle of  $140^\circ$  in Figure 39 and Figure 40 demonstrate this.



**Figure 42: Example of a polariser aligned orthogonally to a single grating vector on a hexagonal grating device.**

In Figure 42 we see an example of how there will always be a large component of light emitted from light originating from interaction with two of the three grating vectors. Therefore as the order of rotational symmetry increases the polarisation dependence decreases. With a grating of concentric circles we would therefore expect to see no polarisation dependence, and similarly no pairs of emission curves.

### 4.3.2 Alternative grating pitch

In addition to using a grating pitch of 580nm, periods of both 540nm and 620nm were also fabricated on separate devices. From the linear relationships described in chapter 1 we would expect this to have an effect on the angular emission. The value of the grating pitch alters the grating wave-vector,  $k_g$ , which in turn alters the angles of emission following equation 1.12.

Figure 43 is a far-field image of the 580nm period device which is similar to the image taken in the previous section (Figure 37). The image has been taken using a polariser to enhance the contrast between the emission curves and the isotropic background light

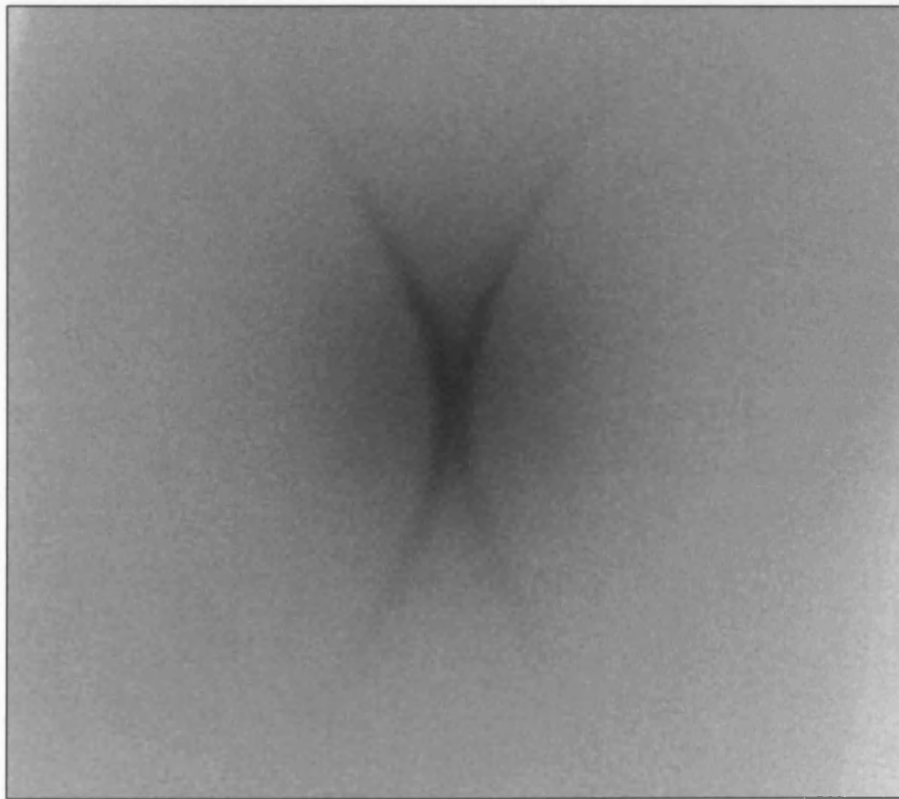
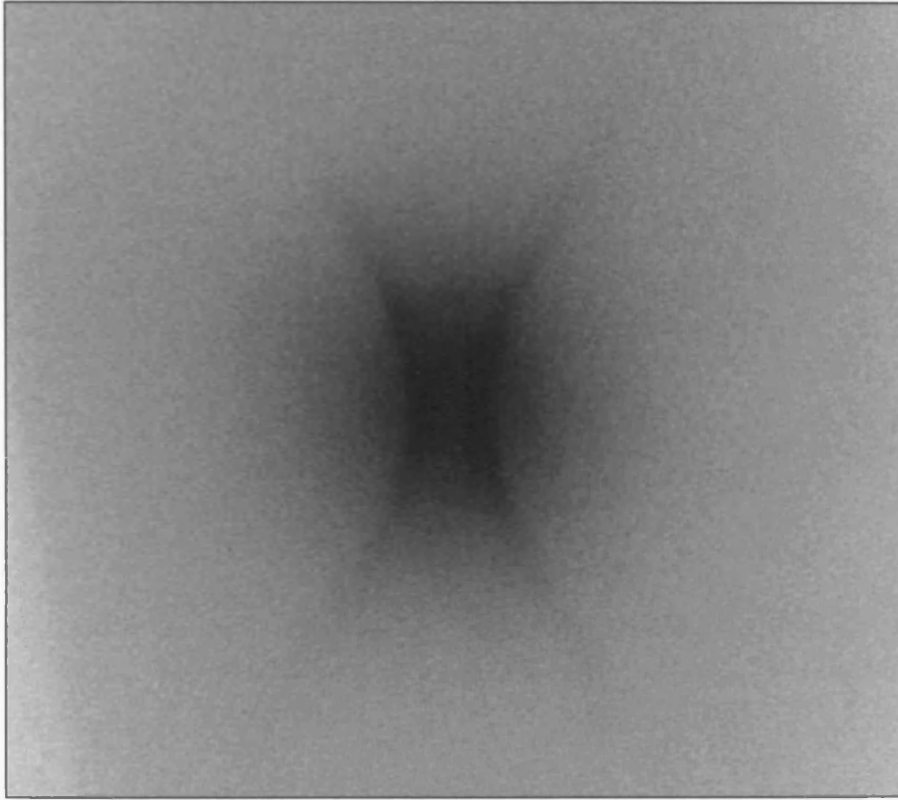


Figure 43: Far-field image from a device with a periodic line grating with a pitch of 580nm

Figure 44 and Figure 45 show the far-field emission patterns for the 540nm and 620nm devices respectively. The smaller grating pitch of 540nm increases the

value of  $k_g$  which results in the pair of emission curves being translated to a higher angle in the x direction.



**Figure 44: Far-field image from a device with a periodic line grating with a pitch of 540nm**

In contrast the increased grating pitch has the opposite effect and the emission curves actually cross and overlap. We can see by observation that the increase or decrease of 40nm results in an equal linear shift in both positive and negative direction along the x-axis of the emission curves.

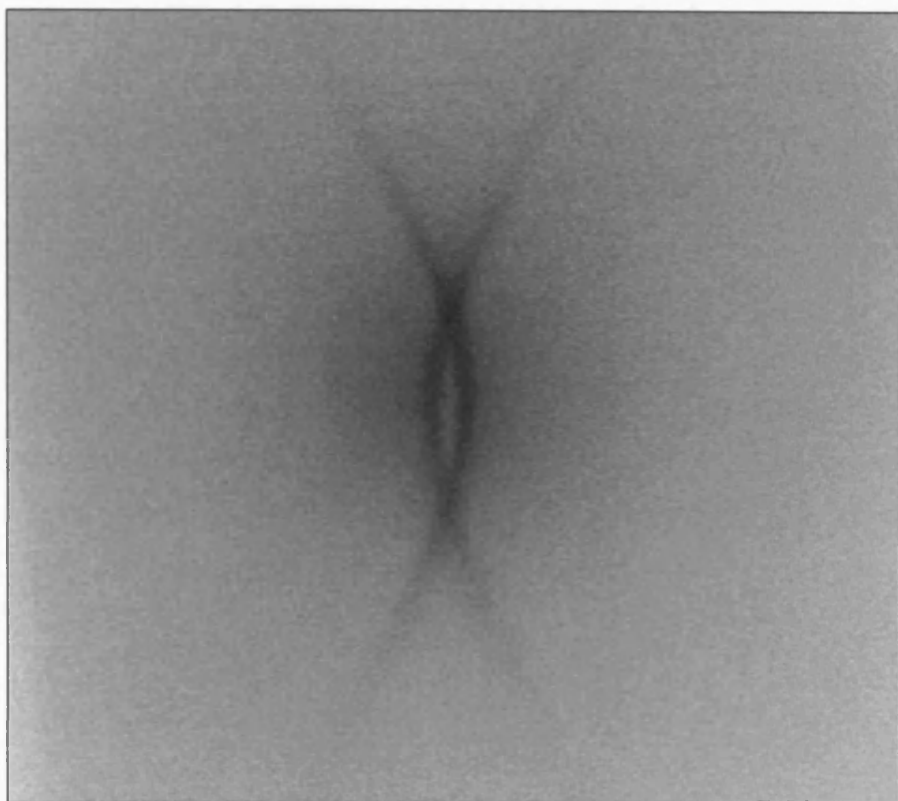


**Figure 45: Far-field image from a device with a periodic line grating with a pitch of 620nm**

The point at which the lines cross is a point in which the emitted light has no component in the x-direction. From analysis of the far-field images we can calculate the grating pitch that would result in normal emission. The relationship between grating pitch and pixels is known, due to a calibration of the setup, to be 3.13nm/pixel. By analysis of the far-field images we can calculate the grating pitch required to get predominately surface normal emission. Using the original uncompressed bitmap image of the 580nm far-field image we can estimate that a translation of around four pixels is needed for the emission curves to pass through the zero point. A four pixel shift is the equivalent of a grating pitch increased by 12.53nm, which would give a grating pitch of 592.53nm. Similarly, using the 620nm device, the image has to be shifted by nine pixels. A shift of nine pixels in the opposing direction equates to a decrease in grating pitch by 28.19nm. Therefore from using the far-field image of the 620nm device a grating pitch of 591.80nm would be required for emission at zero degrees along the x-axis. Taking into account the errors in this analysis due to the resolution of the camera, and other factors such as the errors in the fabrication of the device, we can

approximate the grating pitch for normal emission relative to the x direction to be 592nm. This is only applicable to this particular device as alterations of the gold thickness, dimensions of the SiO<sub>2</sub> islands or the actual semiconductor materials would result in a different value of the surface plasmon wave-vector and hence alter the values required for coupling to occur.

If this were a device with a periodic gold film with a higher order of rotational symmetry, similar to the hexagonal grating shown earlier in this chapter, it would be possible to produce a highly directional beam profile by using a specific value of the grating pitch. This would be a cheap and simple yet effective way to control the large optical divergence that is typical from an LED device.

## 5 Surface Plasmon Analysis

### 5.1 Calculated versus Experimental surface plasmon wave-vector value

It has previously stated that the dispersion relationship for the surface plasmon can be described by:

$$k_x = \frac{\omega}{c} \left( \frac{\epsilon_1 \epsilon_2}{\epsilon_1 + \epsilon_2} \right)^{\frac{1}{2}} \quad (5.1)$$

This relationship is derived from a semi-infinite interface between medium 1 and 2. In a real device, due to the finite thickness of a material layer and the evanescent field of the surface plasmon this will always be an approximation. However it is very accurate when material thicknesses are of the order of many microns. If we consider the interface between gold and air, then we can calculate the depth into the material that the field drop to 1/e of its maximum. This depth is calculated by (60):

$$\hat{z}_2 = \frac{\lambda}{2\pi} \left( \frac{|\epsilon_1'| + \epsilon_2}{\epsilon_2^2} \right)^{\frac{1}{2}} \quad (5.2)$$

And

$$\hat{z}_1 = \frac{\lambda}{2\pi} \left( \frac{|\epsilon_1'| + \epsilon_2}{\epsilon_1^2} \right)^{\frac{1}{2}} \quad (5.3)$$

Where  $\epsilon_1'$  is the real part of  $\epsilon_1$ , the dielectric constant of the metal and  $\epsilon_2$  is the dielectric constant of the air. For a wavelength of 600nm, the depth is 31nm into the gold and 280nm into air (60). Figure 46 shows the evanescent decay of the

electric field in the x direction of a surface plasmon which exists at in interface in the y-z plane.

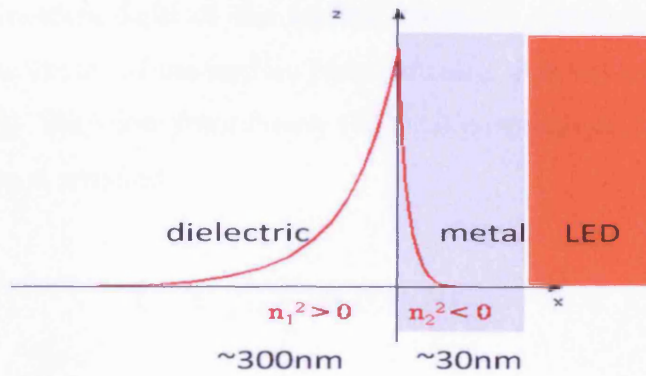


Figure 46: Evanescent field decay into dielectric material and metal layer.

This ‘skin depth’ increases approximately linearly with the wavelength due to the wavelength dependence of  $\epsilon_1$ . We can see that for wavelengths around 650 nm the skin depth would be approximately the depth of the 50 nm gold film and the electric field would certainly still be of substantial size at the distance of the SiO<sub>2</sub> islands. It is easy to see that the calculated wave-vector for a self-infinite interface between two materials would not be expected to be a perfect match to the actual wave-vector of the surface plasmon which exists between the gold film and air. The evanescent tail of the surface plasmon also extends far enough so that an overlap with the beam profile within the edge-emitting LED is possible, and hence coupling between these fields occurs.

From equation 1.12 we can calculate the surface plasmon wave-vector due to all known variables. Using the dielectric constant at 660nm as  $\epsilon_1' = -14.95$ , the dielectric constant of the output material, air, to be  $\epsilon_2 = 1$  and a wavelength of 660nm we can calculate the surface plasmon wave-vector to be  $9.892 \times 10^6 \text{ m}^{-1}$ . The wavelength of 660 nm is used as this is the peak wavelength spectra associated with surface plasmon emission as shown in chapter 3. The value of  $9.892 \times 10^6 \text{ m}^{-1}$  is derived mainly from theory, except the wavelength value. Using

a wavelength of 650 nm, and the appropriate value of the gold dielectric constant for this wavelength, we obtain a wave-vector of  $1.007 \times 10^7 \text{ m}^{-1}$ .

These values are again simply obtained by considering a semi-infinite interface and not a device of finite thickness of the order of magnitude of the skin depth of the decaying evanescent field of the surface plasmon. However we can also calculate the wave vector of the surface plasmon using data we have obtained in the measurements. We know from theory (60) that coupling can occur when the following equation is satisfied

$$k_{sp} = \sqrt{\epsilon_0} \frac{\omega}{c} \sin \theta_i \pm N k_g \quad (5.4)$$

It is in fact only  $k_{sp}$  that is an unknown in this equation. The coupling angle  $\theta_i$  is known to be  $4.9^\circ$  for a device with pitch 580 nm. This value was recorded from the far-field emission images and from profile scanning using a photodetector at various angles relative to the device. K-space analysis in chapter 1 shows that coupling in a linear grating occurs when a surface plasmon in the negative x direction is shifted by a grating momentum vector,  $k_g$ , in the opposite direction. Therefore we can say that

$$\sqrt{\epsilon_0} \frac{\omega}{c} \sin \theta_i = -k_{sp} + k_g \quad (5.5)$$

And so

$$k_{sp} = k_g - \sqrt{\epsilon_0} \frac{\omega}{c} \sin \theta_i \quad (5.6)$$

	Surface Plasmon k-vector
Experimental value	$1.002 \times 10^7 \text{ m}^{-1}$
Theoretical value	$9.892 \times 10^6 \text{ m}^{-1}$

The results can be seen in the table above. Using this equation 5.6 we can calculate the surface plasmon wave-vector to be  $1.002 \times 10^7 \text{ m}^{-1}$ . This value was also calculated at an emission wavelength of 660 nm. The experimental value is slightly higher than the theoretical value of  $9.892 \times 10^6 \text{ m}^{-1}$ , meaning that the surface plasmon wavelength has a smaller value in this thin gold film. It could be suggested that the retardation of the surface plasmon wave could be due to the evanescent tail of the surface plasmon overlapping into the high refractive index semi-conductor material but that is speculative and would need further work to establish a firm reason.

It is useful to refer back to the k-space coupling theory in section 1.2.2. Figure 47 shows simply the central circle representing free-space photons. The radius of this circle has been calculated for a wavelength of 660 nm, the maximum wavelength from the surface plasmon component of the emission. This particular diagram shows the curves within this circle from the overlapping surface plasmon circles for a device with a hexagonal grating. The radius of all the surface plasmon circles is  $1.007 \times 10^7 \text{ m}^{-1}$ , the value obtained from experiment.

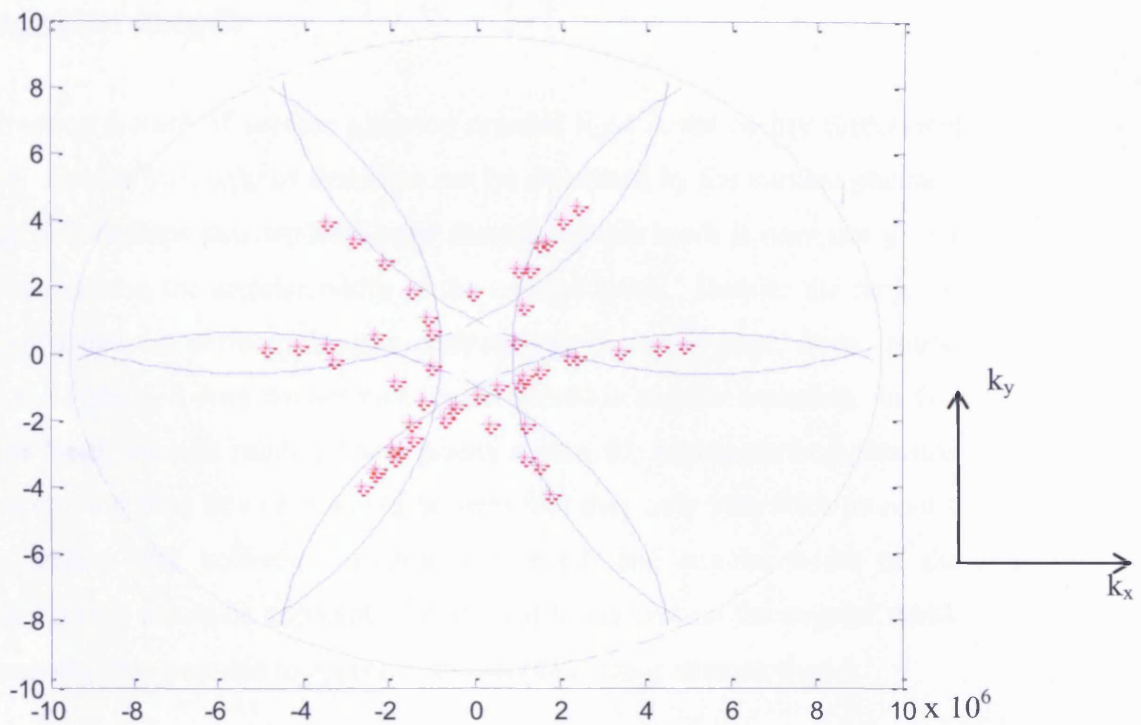


**Figure 47: k-space representation of the coupling values for the hexagonal grating device. The curved lines are theoretical points whilst the crosses are points converted from far-field emission images. (Refer to chapter 1.2.2. for explanation of this representation.)**

Data points from the far-field image of the hexagonal device have been taken and converted into k-space values, marked as crosses. Knowing the dimensions involved this is possible via simple trigonometry. It can be seen that the far-field emission from the hexagonal device matches the theoretical pattern well.

## ***5.2 Dipole antenna array and surface plasmon propagation length***

An interesting feature of surface plasmon emitted light is the highly directional emission. Whilst the angle of emission can be described by the surface plasmon coupling relationships that we have seen throughout this work it does not go far towards describing the angular width of the emitted beam. Despite the range of wavelengths that the surface plasmon emitted light is spread over, from around 654 nm to ~665nm, it does not account for the spread in angular emission. In fact if spectra were taken at random local points within the strong surface plasmon emission curve from a device it would be seen that they only vary with intensity. If there were a link between emission wavelength and angular width of the emission curve it would be apparent. To attempt to understand the angular width of the emission it is possible to approach the problem using antenna theory.

The beam formation from surface plasmon emission can be seen to be very similar to that of the construction of far-field patterns from oscillating dipoles. This is possible if we consider the periodic thin film to be constructed of multiple radiating points. In fact we say that each periodic element is a single radiating dipole. We shall just consider a one dimensional grating and therefore, using  $20\mu\text{m}$  divided by the grating pitch of 580 nm, we have 34.48 radiating points. Antenna array theory is well developed and can be used for optical emission in this instance as opposed to typically radio or microwave radiation. Figure 48 shows a typical linear array of equally spaced dipoles each contributing to the far field emission pattern.

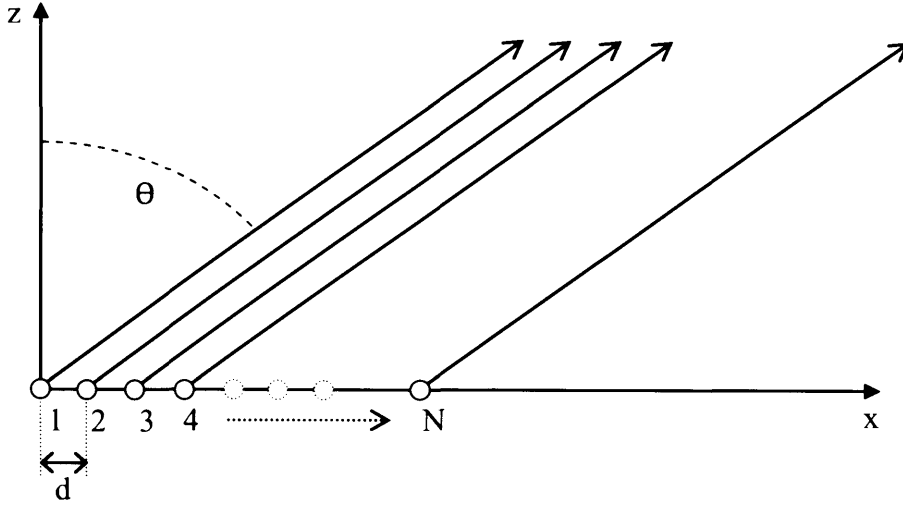


Figure 48: Linear array of N dipole oscillators.

The far-field pattern of the electric field can be described by (88):

$$E(\theta) = \left(\frac{1}{N}\right) \frac{\sin(N(\beta d \sin(\theta) + \delta)/2)}{\sin((\beta d \sin(\theta) + \delta)/2)} \quad (5.7)$$

Where N is the number of contributing dipoles, d is the distance between dipoles,  $\theta$  is the angle from normal,  $\beta = 2\pi/\lambda$  (where  $\lambda$  is the free-space emission wavelength) and  $\delta$  is the relative phase. The relative phase refers to the phase of the surface plasmon wave with respect to the grating elements. This phase term determined by

$$\delta = 2\pi \frac{d}{\lambda_{sp}} \quad (5.8)$$

Where  $\lambda_{sp}$ , the wavelength of the surface plasmon wave, is given simply as

$$\lambda_{sp} = \frac{2\pi}{k_{sp}} \quad (5.9)$$

In this case d is the value of the grating pitch.

Matlab (89) was used to model a linear array of N emitters. The code can be seen in Appendix 7.2. Figure 49 and Figure 50 show the optical intensity as a function

of emission angle, where  $0^\circ$  is normal emission, for an array of 34 elements. Figure 49 shows clearly the highly directional emission from the array, which in this case would be aligned vertically. However it is more convenient to use standard plots, such as Figure 50, for analysis of the beam width.

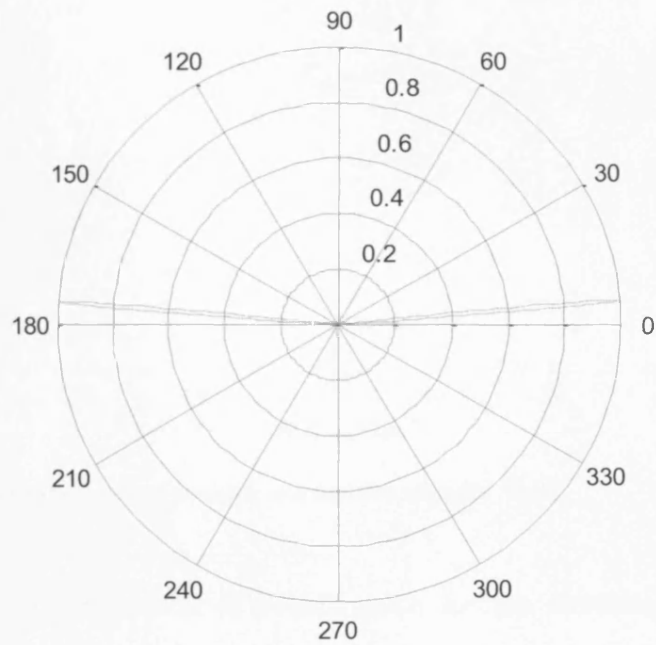
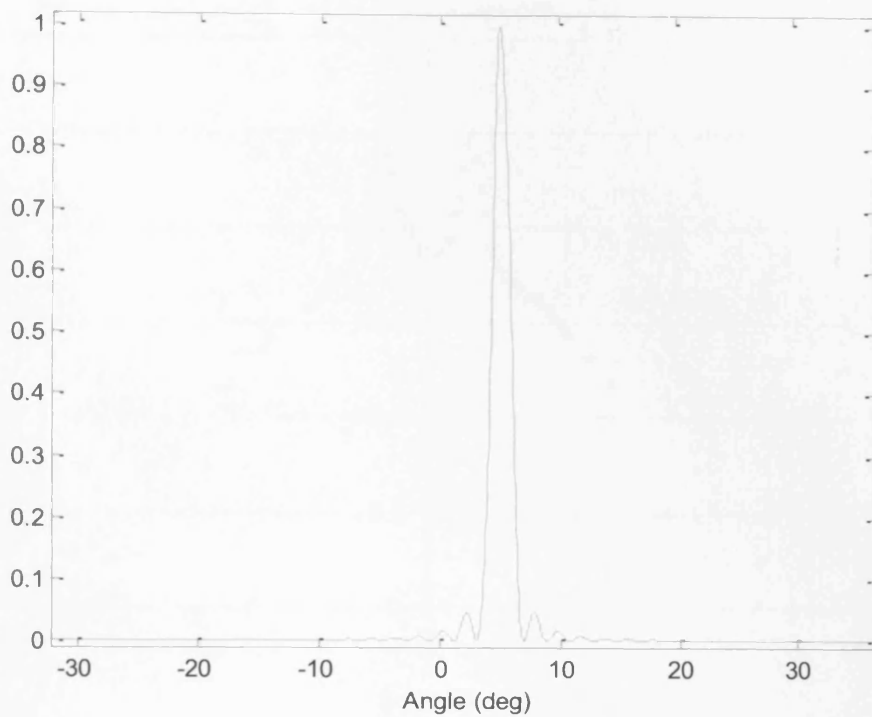


Figure 49: Polar plot of optical intensity as a function of angle.  $N=34$ .



**Figure 50: Plot of normalised optical intensity as a function of angle. N=34.**

The full width half maximum (FWHM) value for the simulation 34 emitting dipoles is  $1.6^\circ$ . The peak is at a value of  $4.93^\circ$  which matches experimental data accurately. There is only one emission peak at  $4.93^\circ$ , as opposed to two, reflected about the normal, due to this model only considering the surface plasmon wave travelling in one direction. If we were to consider both positive and negative directions we would achieve the symmetry we see in the devices.

A line-profile scan is used to compare the FWHM of the simulation to that of a real device. Figure 51 is a line-profile of the optical intensity taken from the 580 nm grated device. The data was taken at an angle of  $22^\circ$  from normal as to ensure that the emission peaks are separated. The width of the strong emission curves, and therefore the pair of peaks in Figure 51, does not vary with the angle,  $\alpha$  (as previously defined), with respect to the grating vector. We can see that the strong emission peaks are on top of a background of isotropic LED emission. The uniformity of the background emission can be seen very clearly in a polar plot of the same data (Figure 52).

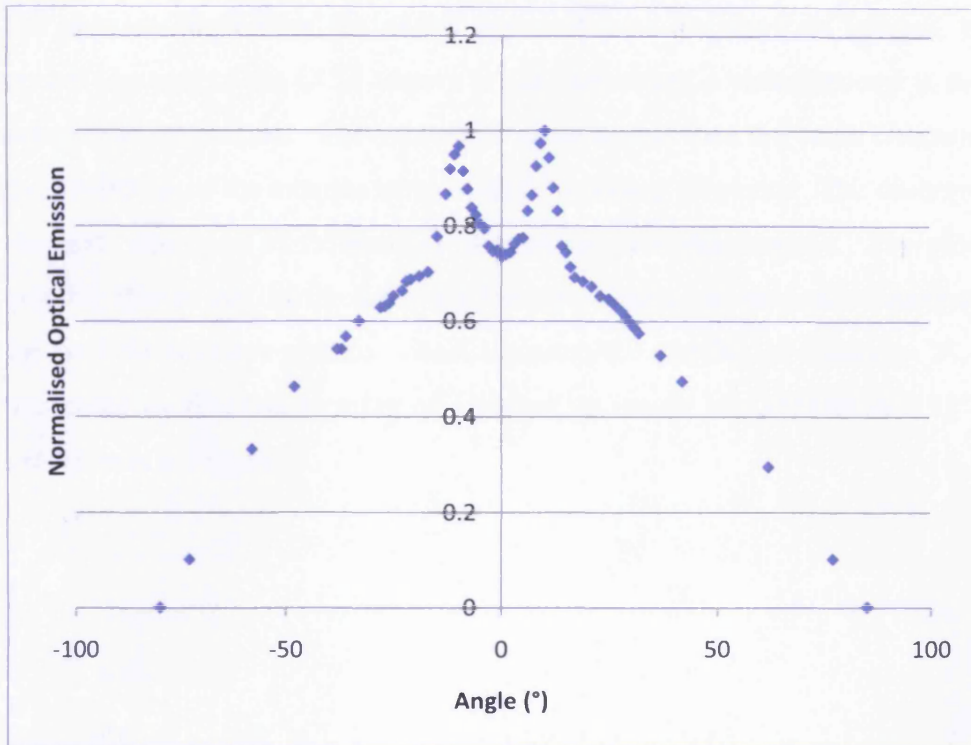


Figure 51: Optical intensity of emitted light as a function of angle. This line-scan profile is taken at an angle of  $22^\circ$  relative to the normal of the plane of the 580 nm grated device.

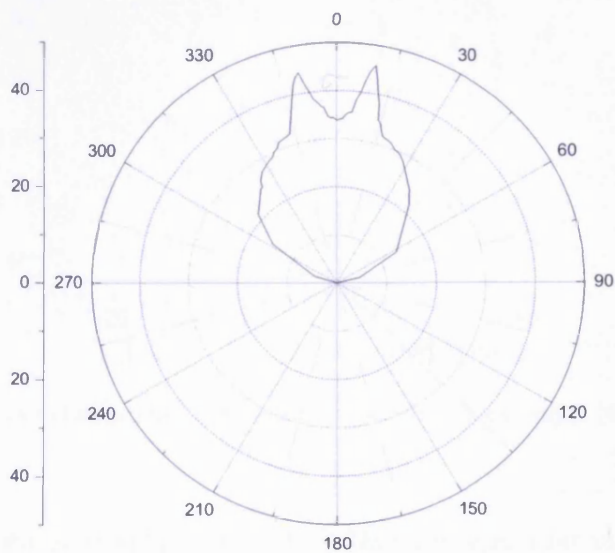
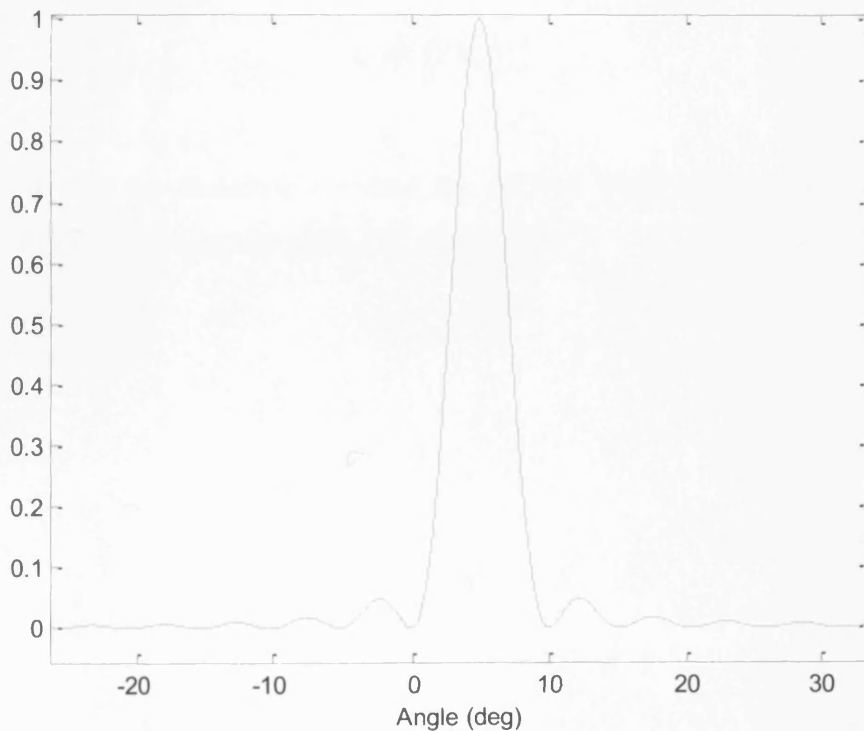


Figure 52: Polar plot of the line-scan through the optical emission emitted at an angle of  $22^\circ$  relative to the normal of the plane of the 580 nm grated device.

From Figure 51 the FWHM of the two peaks are found to be around  $5^\circ$ . Note that this appears larger than the width expected from the far-field images, but the optical linearity of the CCD camera is not known and a photodetector is far more accurate in this respect. The value of  $5^\circ$  is far higher than the value obtained from the modelling of the antenna array with 34 emitting elements. The divergence of the beam decreases as the number of emitting elements increase. Therefore it is possible that in our device there is a reduced number of elements contributing to the far field emission pattern. From adjusting the number of elements,  $N$ , within the model we find that an array of 13 elements results in a FWHM of  $5.18^\circ$ . This can be seen in Figure 53.



**Figure 53:** Plot of normalised optical intensity as a function of angle.  $N=13$ .

Initially this would appear to show that the dipole antenna array model cannot be used as an approach to understand the beam divergence. However in this approach we have assumed that the surface plasmon wave exists across the whole array of 34 points. This assumption is incorrect as the intensity of a surface

plasmon wave decays as it propagates. The surface plasmon wave decays as it propagates as

$$I_{sp} = I_0 e^{-2k_x'' x} \quad (5.10)$$

Where  $k_x''$  is the imaginary component of the surface plasmon wave-vector, given by (60):

$$k_x'' = \frac{\omega}{c} \left( \frac{\epsilon_1' \epsilon_2}{\epsilon_1' + \epsilon_2} \right)^{\frac{3}{2}} \frac{\epsilon_1''}{2(\epsilon_1')^2} \quad (5.11)$$

The length  $L_i$  after which the intensity decreases to 1/e is determined by

$$L_i = (2k_x'')^{-1} \quad (5.12)$$

The values for the dielectric constant are derived from the complex refractive index for gold shown in Appendix 7.3, where  $\epsilon = n^2$ .

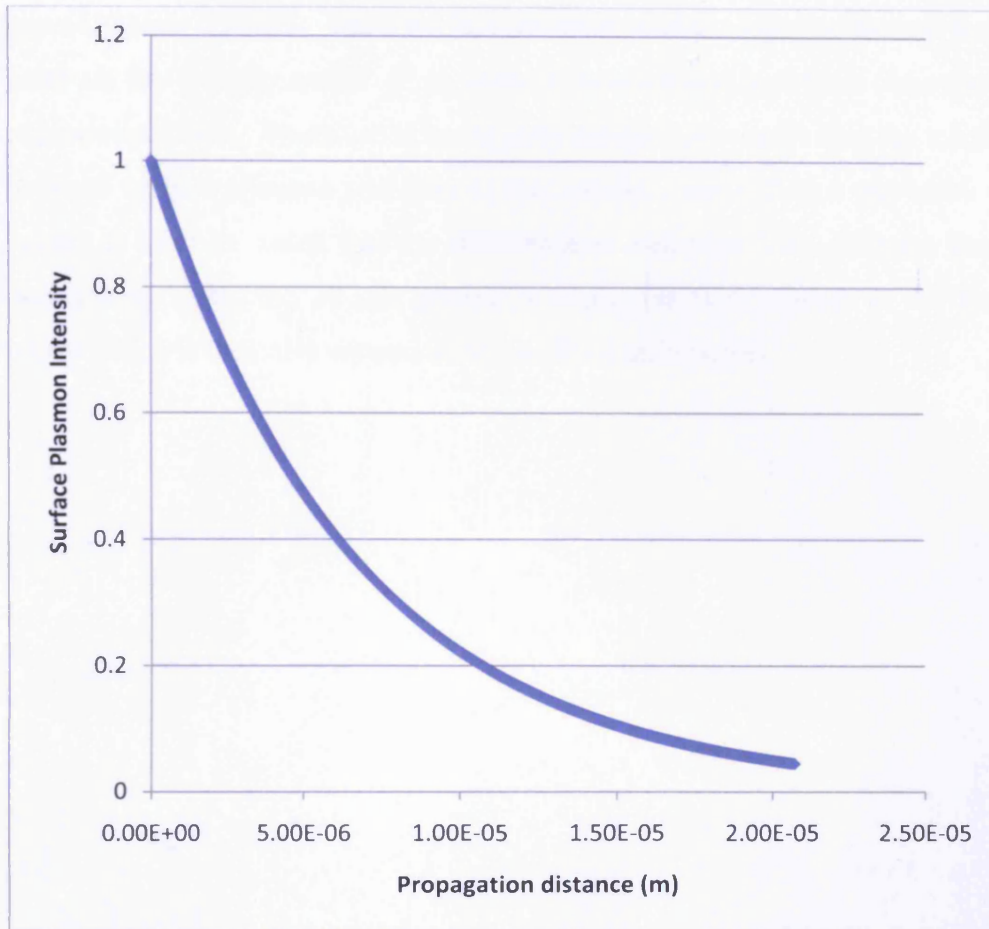


**Figure 54: Intensity decay of a surface plasmon travelling along the interface between gold and air.**

Figure 54 shows the decay in intensity for a surface plasmon travelling along the interface between air and gold. It can be seen that the intensity of the surface plasmon after it has travelled the distance of 20  $\mu\text{m}$ , the full width of the grating, has diminished to 5% of its maximum. The value of  $L_i$  here is calculated to be 6.63 nm. We can see from Figure 54 that the surface plasmon intensity decreases rapidly and the majority of the intensity has decayed over the first 10  $\mu\text{m}$ . The FWHM of the modelled beam implied that there were 13 oscillators contributing to the spatial emission pattern. The length of 13 grating elements, each of 580 nm in length, is 7.54 nm. One should refer to this propagation length as a coherence length, rather than a decay length. It is the coherent nature of the surface plasmon wave that allows comparison with dipole antenna theory.

This result demonstrates that a single surface plasmon wave is not travelling the whole length of the grating, but is decaying rapidly over a distance of

approximately 7.5 nm. Each surface plasmon wave, occurring at any localised point on the grating, results in an angular beam emission which corresponds to experimental data. Therefore it is not only the emission angle that the interaction between surface plasmon and grating has control over, but also the width of the beam. It must be noted that the difference in emission from different localised points from along the 20  $\mu\text{m}$  grating is negligible with respect to the far-field image which is typically viewed on the scale of millimetres.

## 6 Discussion and Concluding Remarks

The general aim of the work in this thesis was to achieve an interaction between surface plasmons and photons emitted from a semiconductor device. The difficulty in this is due to the surface plasmons being classed as non-radiative and therefore a mechanism to allow wave-vector matching must be implemented. To achieve this a periodic grating was added to the standard semiconductor device, which was a typical multiple quantum well (AlGaInP/GaInP) light emitting diode. It is found that a grating of apertures allows for surface plasmons within the gold film to re-radiate into the far-field in a well defined emission pattern. Apertures were used to construct the periodicity required for coupling as previous work showed extra-ordinary enhancement of the transmission of light through sub-wavelength apertures in metallic films. However the presence of apertures allowed for a substantial amount of light to pass through the gold film without interaction. This resulted in the re-radiated emission from surface plasmons being difficult to separate from what is essentially in this instance background emission. Analysis of the measurements taken on this device show that the pattern in the far-field emission is solely due to the re-radiation of surface plasmon waves. It is the periodicity of the gold film that allow coupling to free-space photons to occur.

The subsequent design of the gold film proved to be very successful. The periodicity was introduced into the gold film by depositing a 50 nm thickness of gold over a 30 nm pattern of SiO<sub>2</sub> (photoresist). The processing needed to achieve this is relatively simple and well established. This is in contrast to adding a periodicity into the semiconductor device itself, as some previous work has shown (77). The results from the device with grating without apertures are very successful. The far-field emission demonstrates that a far-higher ratio of surface plasmon emission to 'typical' LED emission is achieved. In effect the gold film grating acts as a conversion filter, absorbing light from the semiconductor and re-emitting it into specific directions. The far-field images are much clearer and we can perform a much better analysis on these devices. It would now be possible, with the understanding we now have of the re-emission of surface plasmons, to

design a device with a more complex emission pattern. A useful future design would be using a grating pitch of 592 nm, which is shown to have emission normal to the top surface of the device. If this was combined with a grating pattern of 6 fold symmetry (such as the hexagonal device) or higher it would produce a highly directional beam from an LED device which would normally have a wide isotropic far-field emission. A high order of rotational symmetry would be required so that a surface plasmon wave, travelling in any direction in the gold film, would always make a relatively small angle between the wave plasmon wave-vector and a pseudo-grating vector.

By treating the emission from the surface plasmon film as analogous to that of a linear antenna array it was shown that the surface plasmon wave does not exist over the entire emission aperture. This is confirmed by a calculation of the propagation length of the surface plasmon wave travelling between air and gold. It appears that the far-field emission pattern from the device can be attributed to the coherent oscillation of the surface plasmon over approximately the distance of 13 grating pitches. To investigate this further it would be interesting to fabricate new devices with a varying aperture window, from a 10 nm to 100 nm square. If the far-field emission pattern was related to sets of around 13 grating elements we would not see a difference between these devices. In fact it would be interesting to see how the optical intensity varied with the size of the emission window. Ideally we would like to see the 'background' emission i.e. the emission not directly from surface plasmon re-emission, to be reduced. It would be useful to fabricate devices with varying thickness of the gold film and at different ratios to the SiO<sub>2</sub> island thickness. However this would be expected to have an effect on the value of  $k_{sp}$ , and therefore the angular emission could not be accurately predicted until a 'calibration' device has been tested.

Something that is not yet understood is why the surface plasmon emission is at a wavelength of 660 nm, and what governs the spectral width of the emission. Although the integration of the gold film onto the device has many benefits for future practical applications it does not allow for simple analysis of the coupling of light within the semiconductor device and the surface plasmon waves in the

gold film. In a system where the photon source is separated from the surface plasmon interface, such as the work in chapter 1.4.1, it is possible to vary the incoming light in terms of its wavelength, incident angle and polarisation. With an integrated device it is difficult to adjust the wavelength of the incoming light, although some change is possible by reducing the temperature. The semiconductor material within the device could be altered to produce a different wavelength but then we are possibly adjusting two variables; both the wavelength and the dielectric constants within the device, which could have an effect on the surface plasmon wave vector, or the waveguided light within the device. Due to the difficulty of adjusting the emission wavelength it would be useful to try to gain a general understanding of the coupling to the surface plasmon. This could be done by depositing the periodic gold/SiO<sub>2</sub> film into glass, or preferably some material with a refractive index near to that of GaAs, the uppermost layer of the device. The incident light could be at a specific wavelength, or, by using the LED device used in this research, a spread of wavelengths could be used which matched that of the wavelengths within the integrated device. Once coupling to the device is understood it may be possible to increase the rate at which light within the device is absorbed into the surface plasmon layer, and hence increase surface plasmon re-emission from the device. Using resonant cavity LEDs or VCSELs may prove to be a more efficient device for coupling to surface plasmons as the intensity profile within the device may overlap with that of the evanescent field of the surface plasmon more than that of the ‘tail’ guided beam within an edge-emitting LED.

In addition to these future experimental measurements it would be very useful to have an accurate model to predict the electric fields in and around the gold film and the interaction with photons. While the modelling in this research is very useful in determining the far-field emission it is not able to make accurate predictions on complex systems, such as  $k_{sp}$  values for gratings with SiO<sub>2</sub> islands of a particular size or shape. The linear coupling models also do not consider the propagation length of the surface plasmon or the evanescent decay into the materials at the interface. It would also be of interest to investigate how more complex emission patterns could be obtained from corrugations in the gold film.

For example a far-field emission of a straight line, a cross, small circles etc. It might technically be difficult to fabricate the gold film to make such emission patterns but it would be interesting to see what was possible. In the work presented in this thesis the gratings, or pseudo-gratings, are linear and of constant grating pitch throughout the pattern. It is of course possible to have a curved grating with a varying grating pitch.

This research relates back to the optical biochips project as it is similar to the surface plasmon resonance (SPR) experiments that are useful for cell-biologists. In typical SPR experiments we detect coupling to surface plasmons by a drop in the reflected intensity of light from a metal surface. The devices in this research transmit, as opposed to reflect, light determined by the coupling relationships. Therefore it is the angle of transmission that determines the presence, or activity, of cells or molecules near the surface and can be considered to be a transmission surface plasmon resonance experiment (T-SPR). The continued development of the devices used in this research could lead to devices which could perform rapid SPR experiments in the field without the need for large desktop instrumentation or a fixed power supply. The uses of such a device could span from cheap manufacturing sensors to military sensors for chemical and biological sensing. More work would have to be done to make these devices more suitable for this function, including minimising the width of spatial and spectral surface plasmon emission.

While there is a lot of future research that could be done in this area, the work described in this thesis is very successful. This is an area of physics and optoelectronics that is relatively new and there is relatively little previous work in the area of spatial emission control using a simple gold film. The aim of this research was to achieve coupling between photons and surface plasmons within a single semiconductor device. We have shown that not only has this been made possible via a sub-wavelength grating but that we have also produced a device with a far-field emission which has a substantial amount of emission contributed by surface plasmons on the gold surface. We have gained an understanding about how the design of the grating can alter far-field emission from the device, in terms

of both angle and pattern. This work essentially demonstrates that a typical optically emitting semiconductor device can have a periodic gold film integrated, relatively cheaply and easily, in order to control the properties of the emission.

## 7 Appendix

### 7.1 Matlab code for the analysis of grating coupling.

```
%%%%%%%%%%%%%% k-space coupling %%%%%%%%%%%

clear, clg, hold off;

%      definition of variables

L = 20;           % distance at which far-field imaged (mm)
lambda = 0.66;
d = 0.58;        % grating pitch
kg = 2*pi/d;
kph = 2*pi/lambda;
ksp = 10.0;

theta = 0:1:360;
theta = 2*pi*theta./360;

yph = kph*sin(theta);
xph = kph*cos(theta);

ysp = ksp*sin(theta);
xsp = ksp*cos(theta);
xspgplus = xsp + kg;
xspgminus = xsp - kg;

plot(xph, yph, xsp, ysp, xspgplus, ysp, 'r-', xspgminus, ysp, 'r-');
axis([-25 25 -25 25]);

xcross = (kph.^2+kg.^2-ksp.^2)./(2.*kg)
xcrossp = kg-xcross;
angcross = acos(xcrossp/ksp);
angcross = round(180.*angcross./pi)-1;

pause;           % calculate matched part of k-space

alpha = -angcross:1:angcross;
alpha = 2*pi*alpha./360;

yspr = ksp*sin(alpha);
xspr = ksp*cos(alpha);
xsprinv = -xspr;
xsprp = xsprinv + kg;
xsprm = xspr - kg;

ang2 = atan(yspr./xsprp);
xsprp2 = xsprp.*cos(ang2+pi/3)./cos(ang2);
xsprp3 = xsprp.*cos(ang2+2*pi/3)./cos(ang2);
ysprp2 = yspr.*sin(ang2+pi/3)./sin(ang2);
ysprp3 = yspr.*sin(ang2+2*pi/3)./sin(ang2);
```

```

ang3 = atan(yspr./xsprm);
xsprm2 = xsprm.*cos(ang3+pi/3)./cos(ang3);
xsprm3 = xsprm.*cos(ang3+2*pi/3)./cos(ang3);
ysprm2 = yspr.*sin(ang3+pi/3)./sin(ang3);
ysprm3 = yspr.*sin(ang3+2*pi/3)./sin(ang3);

%experimental data
exptx = [2 4.2 5.8 7.3 8.1 9 9.8 9.4 9 8.8 8.7 8.9 9.1 9.6 10.1
10.6 9.4 8.8 7.7 6.6 5.3 4 3.1 2 3.5 4.5 5.4 6.2 6.7 6.7 6.5 6.2
5.7 5.2 4.7 5.9 7.2 8.3 9.3 10.2 11.4 12.6 13.5 11.4 10 8.9 7.8 7
6.2 5.7 5.1 4.7];
expty = [10.9 10.5 9.8 9.1 8.5 7.3 5.8 7 8.5 9.8 11.1 12.2 13.4
14.4 15.3 15.9 14.3 13.4 12.6 11.8 11.3 11 10.9 10.9 15.5 14.6
13.7 12.7 11.4 10.3 9.2 8.5 7.6 6.8 6 7.6 9 9.7 10.2 10.6 10.8
10.9 11 10.8 10.6 10 9.4 8.7 8 7.3 6.6 6];

exptx = 2.08.*(exptx-7.8);
expty = 2.08.*(expty-10.7);

theta = atan(expty./exptx);
for i = 1:length(expty),
    if (exptx(i) < 0)
        theta(i) = pi+atan(expty(i)./exptx(i));
    end
end

beta = atan(sqrt(exptx.^2+expty.^2)./L);

kxexpt = kph.*sin(beta).*cos(theta);
kyexpt = kph.*sin(beta).*sin(theta);

plot(xspgplus, ysp, 'r-', xspgminus, ysp, 'r-
', xsprp, yspr, 'y', xsprm, yspr, 'y', xsprp2, ysprp2, 'y', xsprm2, ysprm2, 'y
', xsprp3, ysprp3, 'y', xsprm3, ysprm3, 'y', kxexpt, kyexpt, '*');
pause;
plot(xph, yph, 'g', xsprp, yspr, 'b', xsprm, yspr, 'b', xsprp2, ysprp2, 'b', x
sprm2, ysprm2, 'b', xsprp3, ysprp3, 'b', xsprm3, ysprm3, 'b', kxexpt, kyexpt
, '*r');
axis([-10 10 -10 10]);

```

## 7.2 Matlab code for N-dipole array

```
%%%%%%%%% N-dipole antenna array %%%%%%%%%%

clear;

pitch = 580E-9;
lambda = 660E-9;

n=14;
alpha = 0;

pitch_eff = pitch/(cos(alpha*pi/180));

angle= [-180:0.05:180];

k_sp = ((2*pi/lambda)*sin(4.9233*pi/180)) - (2*pi/pitch_eff);
%k_sp= ((2*pi)/lambda)*sqrt(-11.8/-10.8);

lambda_sp = (2*pi)/k_sp

phase = 2*pi*pitch/lambda_sp;

i=1;
while i<=max(size(angle))

    a(i) = ((2*pi*pitch_eff)/lambda)*sin(angle(i)*pi/180) +
    phase;

    E(i) = (1/n) * (sin (n*a(i)/2)) / (sin(a(i)/2));

    I(i) = E(i)*E(i);

    i=i+1;
end

polar(angle*pi/180,I)

pause;

plot(angle, I);
```

### 7.3 Refractive Index data for gold as a function of wavelength(60)

Lambda(nm)	n (Au)	k (Au)
610	0.2184	3.1833
611	0.216	3.1939
612	0.2137	3.2045
613	0.2114	3.215
614	0.2091	3.2255
615	0.2069	3.236
616	0.2047	3.2465
617	0.2026	3.257
618	0.2004	3.2674
619	0.1984	3.2779
620	0.1963	3.2883
621	0.1943	3.2986
622	0.1923	3.309
623	0.1903	3.3194
624	0.1884	3.3297
625	0.1865	3.34
626	0.1847	3.3503
627	0.1828	3.3605
628	0.181	3.3708
629	0.1793	3.381
630	0.1776	3.3912
631	0.1759	3.4014
632	0.1742	3.4116
633	0.1726	3.4218
634	0.171	3.4319
635	0.1695	3.442
636	0.1679	3.4521
637	0.1664	3.4622
638	0.165	3.4723
639	0.1636	3.4823
640	0.1622	3.4923
641	0.1608	3.5023
642	0.1595	3.5123
643	0.1582	3.5223
644	0.157	3.5323
645	0.1557	3.5422
646	0.1545	3.5521
647	0.1534	3.562
648	0.1523	3.5719
649	0.1512	3.5818
650	0.1501	3.5916
651	0.1491	3.6014
652	0.1481	3.6113

Lambda(nm)	n (Au)	k (Au)
653	0.1472	3.621
654	0.1462	3.631
655	0.1454	3.641
656	0.1445	3.65
657	0.1437	3.66
658	0.1429	3.67
659	0.1421	3.68
660	0.1387	3.689
661	0.1386	3.699
662	0.1384	3.709
663	0.1382	3.718
664	0.1381	3.728
665	0.1379	3.737
666	0.1378	3.747
667	0.1376	3.757
668	0.1375	3.766
669	0.1373	3.776
670	0.1372	3.785
671	0.137	3.795
672	0.1369	3.804
673	0.1368	3.814
674	0.1366	3.823
675	0.1365	3.833
676	0.1364	3.842
677	0.1363	3.851
678	0.1362	3.861
679	0.1361	3.87
680	0.136	3.88
681	0.1359	3.889
682	0.1358	3.898
683	0.1357	3.908
684	0.1356	3.917
685	0.1355	3.926
686	0.1354	3.936
687	0.1353	3.945
688	0.1353	3.954
689	0.1352	3.963
690	0.1351	3.973
691	0.1351	3.982
692	0.135	3.991
693	0.135	4
694	0.1349	4.009
695	0.1349	4.019

## Bibliography

1. *Directional Control of Light-Emitting-Diode Emission Via a Subwavelength-Apertured Metal Surface.* **M. D. Harries, H. D. Summers.** 21, s.l. : IEEE Photonics Technology Letters, 2006, Vol. 18, pp. 2197-2199.
2. *Surface plasmon mediated emission in resonant-cavity light-emitting diodes.* **P. A. Porta, M. D. Harries, H. D. Summers.** 12, 2006, Applied Physics Letters, Vol. 89.
3. *Plasma Losses by Fast Electrons in Thin Films.* **Ritchie, R H.** 874, s.l. : Phys. Rev., 1957, Vol. 106.
4. *A Collective Description of Electron Interactions: II. Collective vs Individual Particle Aspects of the Interactions.* **Pines D., Bohm D.** 338, s.l. : Phys. Rev., 1952, Vol. 85.
5. *Collective Energy Losses in Solids.* **Pines, D.** 184, s.l. : Rev. Mod. Phys., 1956, Vol. 28.
6. *Oscillations in Ionized Gases.* **Tonks L, Langmuir I.** 195, s.l. : Phys. Rev., 1929, Vol. 33.
7. *Elektronenbremsung an Röntgenniveaus.* **Ruthemann, G.** 145, s.l. : Ann. Phys., 1942, Vol. 30.
8. **Lang, W.** 233, s.l. : Optik, 1948, Vol. 3.
9. *Origin of the Characteristic Electron Energy Losses in Aluminum.* **Powell C.J., Swan J.B.** 869, s.l. : Phys. Rev, 1959, Vol. 115.
10. *Surface Plasma Oscillations of a Degenerate Electron Gas.* **Stern E.A., Ferrell R.A.** 130, s.l. : Phys. Rev., 1960, Vol. 120.
11. *Van der Waals interaction between an atom and a solid surface.* **Zaremba E., Kohn W.** 2270, s.l. : Phys. Rev. B, 1976, Vol. 13.
12. *Effects of spatial dispersion on electromagnetic surface modes and on modes associated with a gap between two half spaces.* **Sernelius, B E.** 235114, s.l. : Phys. Rev. B, 2005, Vol. 71.
13. *Inclusion of dynamics in the ion-metal surface interaction.* **Feibelman, P J.** 438, s.l. : Surf. Sci., 1971, Vol. 27.
14. *Surface plasmons and the image force in metals.* **Ritchie, R H.** 189, s.l. : Phys. Lett. A, 1972, Vol. 38.

15. *Dynamical image charge theory*. **Ray R., Mahan G.D.** 301, s.l. : Phys. Lett. A, 1972, Vol. 42.
16. *Dynamical corrections to the image potential*. **Sunjic M., Toulouse G., Lucas A.A.** 415, s.l. : Solid State Commun., 1972, Vol. 11.
17. *Theory of electron-hole pair excitations in unimolecular processes at metal surfaces*. **Gadzuk J.W., Metiu H.** 2603, s.l. : Phys. Rev. B, 1980, Vol. 22.
18. *Plasmon theory of the surface energy of metals*. **Schmit J., Lucas A.** 415, s.l. : Solid State Commun., 1972, Vol. 11.
19. *Exchange-correlation in inhomogeneous systems— a comment on the surface energy problem*. **Lang N.D., Sham L.J.** 581, s.l. : Solid State Commun., 1975, Vol. 17.
20. *Exchange-correlation energy of a metallic surface: Wave-vector analysis*. **Langreth D.C., Perdew J.P.** 2884, s.l. : Phys. Rev. B, 1977, Vol. 15.
21. *High-Resolution Infrared Study of Hydrogen ( $1 \times 1$ ) on Tungsten (100)*. **Chabal Y.J., Sievers A.J.** 944, s.l. : Phys Review Lett., 1980, Vol. 44.
22. *Vibrational Phase Relaxation at Surfaces: CO on Ni(111)*. **Persson B., Rydberg R.** 2119, s.l. : Phys. Rev. Lett., 1985, Vol. 54.
23. *Absorption profile at surfaces*. **Echenique P.M., Pendry J.B.** 2936, s.l. : Phys. C: Solid State Phys., 1975, Vol. 8.
24. *Semiclassical image potential at a solid surface*. **Echenique P.M., Ritchie R.H., Barberan N., Inkson J.** 6486, s.l. : Phys. Rev. B, 1981, Vol. 23.
25. *Theory of core-hole-decay dynamics of adsorbates on metal surfaces: Role of the  $2\pi^*$  level of a chemisorbed CO molecule*. **Ueba, H.** 569, s.l. : Phys. Rev. B, 1992, Vol. 45.
26. *Interfaces and thin films as seen by bound electromagnetic waves*. **Knoll, W.** 569, s.l. : Anni.Rev.Phys. Chem., 1998, Vol. 49.
27. **Herminghaus S., Vorberg J., Gau H., Conradt R., Reinelt D., Ulmer H., Leiderer P., Przyrembel M.** 425, s.l. : Ann. Phys. Lpz., 1997, Vol. 6.
28. *Biospecific interaction analysis using biosensor technology*. **Malmqvist, M.** 186, s.l. : Nature, 1993, Vol. 261.
29. **Braguglia, C M.** 183, s.l. : Chem. Biochem. Eng., 1998, Vol. 12.
30. *A sensitivity comparison of optical biosensors based on four different surface plasmon resonance modes*. **Chien F.C., Chen S.J.** 633, s.l. : Biosensors Bioelectron., 2004, Vol. 20.

31. *Inelastic tunneling excitation of tip-induced plasmon modes on noble-metal surfaces.* **Berndt R., Gimzewski J.K., Johansson P.** 3796, s.l. : Phys. Rev. Lett., 1991, Vol. 67.
32. *Surface-plasmon ejection of Ag<sup>+</sup> ions from laser irradiation of a roughened silver surface.* **Shea M. J., Compton R.N.** 9967, s.l. : Phys. Review. B, 1993, Vol. 47.
33. *Photoinduced Conversion of Silver Nanospheres to Nanoprisms.* **Jin R. C. Cao Y.W., Mirkin C.A., Kelly K.L., Schatz G.C., Zheng J.G.** 1901, s.l. : Science, 2001, Vol. 294.
34. *Controlling anisotropic nanoparticle growth through plasmon excitation.* **Jin R., Cao C., Hao E., Metraux G.S., Schatz G.C., Mirkin C.** 487, s.l. : Nature, 2003, Vol. 425.
35. *Surface plasmon microscopy.* **Rothenhausler B., Knoll W.** 615, s.l. : Nature, 1988, Vol. 332.
36. *Two-Dimensional Imaging of Potential Waves in Electrochemical Systems by Surface Plasmon Microscopy.* **Flatgen G., Krischer K., Pettinger B., Doblhofer K., Junkes H., Ertl G.** 668, s.l. : Science, 1995, Vol. 269.
37. *Reliable determination of binding affinity and kinetics using surface plasmon resonance biosensors.* **Schuck, P.** 498, s.l. : Curr. Opin. Biotechnol., 1997, Vol. 8.
38. *Surface plasmon resonance sensors: review.* **Homola J., Yee S.S., Gauglitz G.** 3, s.l. : Sensors Actuators B, 1999, Vol. 54.
39. *Protein Interaction Methods-Toward an Endgame.* **Mendelson A.R., Brend R.** 1948, s.l. : Science, 1999, Vol. 284.
40. *Surface plasmon resonance analysis of dynamic biological interactions with biomaterials.* **Green R.J., Frazier R.A., Shakeshaft K.M., Davies M.C., Roberts C.J., Tendler S.J.B.** 1823, s.l. : Biomaterials, 2000, Vol. 21.
41. *Playing Tricks with Light.* **Pendry, J B.** 1687, s.l. : Science, 1999, Vol. 285.
42. *A Hybridization Model for the Plasmon Response of Complex Nanostructures.* **Prodan E., Radloff C., Halas N.J., Nordlander P.** 419, s.l. : Science, 2003, Vol. 302.
43. *Extraordinary optical transmission through sub-wavelength hole arrays.* **Ebbesen T.W., Lezec H.J.** 419, s.l. : Nature, 1998, Vol. 302.
44. *Beaming Light from a Subwavelength Aperture.* **Lezec H.J., Degiron A., Devaux E., Linke R.A. Martin-Moreno L., Garcia-Vidal F.J., Ebbesen T.W.** 820, s.l. : Science, 2002, Vol. 297.

45. *Plasmonics: Merging Photonics and Electronics at Nanoscale Dimensions*. **Ozby, E.** 189, s.l. : Science, 2006, Vol. 311.
46. *Surface plasmon subwavelength optics*. **Barnes W.L., Dereux A., Ebbesen T.W.** 824, s.l. : Nature, 2003, Vol. 424.
47. *Nanodot coupler with a surface plasmon polariton condenser for optical far/near-field conversion*. **Nomura W., Ohtsu M. Yatsui T.** 1108, s.l. : Appl. Phys. Lett., 2005, Vol. 86.
48. *Non-diffraction-limited light transport by gold nanowires*. **Krenn J.R., Lamprecht B., Dittbacher H., Schider G. Saleno M., Leitner A., Assenegg F.R.** 663, s.l. : Europhys. Lett., 2002, Vol. 60.
49. *Surface plasmon polaritons in metal stripes and wires*. **Krenn J.R., Weeber J.C.** 739, s.l. : Phys. Rev. Lett. B, 2004, Vol. 362.
50. *Local detection of electromagnetic energy transport below the diffraction limit in metal nanoparticle plasmon waveguides*. **Maier S.A., Kik P.G., Atwater H.A., Metzger S., Harel E., Koel B.E., Requicha A.A.G.** 229, s.l. : Nature Mater., 2003, Vol. 2.
51. *Transition from localized surface plasmon resonance to extended surface plasmon-polariton as metallic nanoparticles merge to form a periodic hole array*. **Murray W.A., Astilean S., Barnes W.L.** 165407, s.l. : Phys. Rev. B, 2004, Vol. 69.
52. *Low-loss fiber accessible plasmon waveguide for planar energy guiding and sensing*. **Maier S.A., Barclay P.E., Johnson T.J., Friedman M.D., Painter O.** 3990, s.l. : Appl. Phys. Lett., 2004, Vol. 84.
53. *Experimental demonstration of fiber-accessible metal nanoparticle plasmon waveguides for planar energy guiding and sensing*. **Maier S.A., Friedman M.D., Barclay P.E., Painter O.** 071103, s.l. : Appl. Phys. Lett., 2005, Vol. 84.
54. *Channel polaritons*. **Novikov I.V., Maradudin A.A.** 035403, s.l. : Phys. Rev. B, 2002, Vol. 66.
55. *Characterization of long-range surface-plasmon-polariton waveguides*. **Berini O., Charbonneau R., Lahoud N., Mattiussi G.** 043109, s.l. : J. Appl. Phys., 2005, Vol. 98.
56. *Active plasmonics: Controlling signals in Au/Ga waveguide using nanoscale structural transformations*. **Krasavin A.V., Zheludev N.I.** 1416, s.l. : Appl. Phys. Lett., 2004, Vol. 84.
57. *Active control of surface plasmon-polariton waves*. **Krasavin A.V., Zayats A.V., Zheludev N.I.** 85, s.l. : J.Opt.A.: Pure Appl. Opt., 2005, Vol. 7.

58. *Energy Transfer Across a Metal Film Mediated by Surface Plasmon Polaritons*. **Andrew P., Barnes W.L.** 1002, s.l. : Science, 2004, Vol. 306.
59. **Kittel, C, Kroemer H.** *Thermal Physics (2nd Edition)*.
60. **Raether, H.** *Surface Plasmons on smooth and rough surfaces and on gratings*. London : Springer-Verlag.
61. *Surface Plasmon sensors: review*. **J. Homolar, S. Yee, G. Gaugltz.** 1-2, 1999, Sensors and Actuators : Chemical, Vol. 54, pp. 3-15.
62. *Plasmon light scattering in biology and medicine: new sensing approaches, visions and perspectives*. **K. Aslan, J. Lakowicz, C Geddes.** 2005, Current Opinion in chemical biology, Vol. 9, pp. 538-544.
63. *Scanning plasmon near-field microscope*. **M. Specht, J. Pedarnig, W. Heckl, T. Hansch.** 1992, Phys. Rev. Lett., Vol. 68, pp. 476-479.
64. *Five-dimensional optical recording mediated by surface plasmons in gold nanorods*. **Zilstra P., Chon J., Gu M.** s.l. : Nature, 2009, Vol. 459.
65. *Achieving transparency with plasmonic and metamaterial coatings*. **Alu A., Engheta N.** 016623, s.l. : Phys. Rev. E, 2005, Vol. 72.
66. *Radiative Transitions in semiconductors*. **Braunstein, R.** 1955, Physical Review, Vol. 99, pp. 1892-1893.
67. **Biard, B. et al.** *Semiconductor Radiant Diode*. 3293513 U.S., 8 August 1962.
68. *Optical Semiconductor Devices*. **Fukado, M.** s.l. : Wiley, 1999.
69. **Mitin, V.** *Quantum Heterostructures*.
70. *Extraordinary optical transmission through sub-wavelength hole arrays*. **T. Ebbesen, H. Lezec, H Ghaemi, T. Thio.** 1998, Nature, Vol. 491, pp. 667-669.
71. *Surface-plasmon enhanced transmission through hole arrays in Cr films*. **T. Thio, H. Ghaemi, H. Lezec, P. Wolff, T. Ebbesen.** 10, 1999, J. Opt. Soc. Am. B, Vol. 16, pp. 1743-1748.
72. *Surface-plasmon-enhanced transmission through metallic gratings*. **U. Schroter, D. Heitmann.** 23, 1998, Physical Review B, Vol. 58, pp. 15419-15421.
73. *Control of optical transmission through metals perforated with subwavelength hole arrays*. **T. J. Kim, T. Thio, T. Ebbesen, D. Grupp, H. Lezec.** 4, 1999, Optics Letters, Vol. 24, pp. 256-258.

74. *Beaming Light from a Subwavelength Aperture*. **H. Lezec, A. Degiron, E. Devaux, R. Linke, L. Martin-Moreno, F. Garcia-Vidal, T. Ebbesen**. 2002, *Science*, Vol. 297, pp. 820-822.
75. *Theory of Highly Directional Emission from a Single Subwavelength Aperture Surrounded by Surface Corrugations*. **L. Martin-Moreno, F. Garcia-Vidal, H. Lezec, A. Derignon, T. Ebbesen**. 16, *Physical Review Letters*, Vol. 90.
76. *Directional Surface Plasmon Coupled Emission*. **C. Geddes, I. Gryczynski, J. Malicka, Z. Gryczynski, J. Lakowicz**. 1, 2004, *Journal of Fluorescence*, Vol. 14, pp. 119-123.
77. *Strongly directional emission from AlGaAs/GaAs light emitting diodes*. **A. Köck, E. Gornik, M. Hauser, W. Beinstingl**. 22, 1990, *Appl. Phys. Lett*, Vol. 57, pp. 2327-2329.
78. *Optimization of the emission characteristics of light emitting diodes by surface plasmons and surface waveguide modes*. **S. Gianordoli, R. Hainberger, A. Kock, N. Finger, E. Gornik, C. Hanke, L. Korte**. 15, 2000, *Applied Physics Letters*, Vol. 77, pp. 2295-2297.
79. *Surface Plasmon Enhanced Light-Emitting Diode*. **J. Vuckovic, M. Loncar, A. Scherer**. 10, 2000, *IEEE Journal of Quantum Electronics*, Vol. 36, pp. 1131-1144.
80. *Surface Plasmon resonance on microaperture vertical-cavity surface-emitting laser with metal grating*. **S. Shinada, J. Hashizume, F. Koyama**. 5, 2003, *Applied Physics Letters*, Vol. 83, pp. 836-838.
81. *Surface Plasmon Mediated Emission for Organic Light-Emitting Diodes*. **P. Hobson, S. Wedge, J. Wasey, I. Sage, W. Barnes**. 19, 2002, *Adv. Mater.*, Vol. 14, pp. 1393-1396.
82. *The Role of Surface Plasmon in Organic Light-Emitting Diodes*. **P. Hobson, J. Wasey, I. Sage, W. Barnes**. 2, *IEEE Journal on Selected Topics in Quantum Electronics*, Vol. 8, pp. 378-386.
83. *Description of a single modular optical setup for ellipsometry, surface plasmons, waveguide modes, and their corresponding imaging techniques including Brewster angle microscopy*. **M. Harke, R. Teppner, O. Shulz, H. Motschmann**. 8, 1997, *Rev. Sci. Instrum.*, Vol. 68, pp. 3130-3134.
84. <http://www.OriginLab.com>. *Origin 8*.
85. *Effects of Sample Thickness on the Optical properties of Surface Plasmon-Coupled Emission*. **I. Gryczynski, J. Malicka, K. Mowczyk, Z. Cryczynski, J. Lakowicz**. 2004, *Journal of Physical Chemistry B*, Vol. 108, pp. 12073-12083.

86. *Determination of dielectric permittivity and thickness of a metal layer from a surface plasmon resonance experiment.* **H. de Bruijn, R. Kooyman, J. Greve.** 13, Applied Optics, Vol. 29, pp. 1974-1978.

87. *Surface-plasmon photonic bandgaps in dielectric gratings on a flat metal surface.* **J. Yoon, G. Lee, S. Song, C. Oh, P. Kim.** 1, Journal of Applied Physics, Vol. 94, pp. 123-129.

88. **Born M., Wolf E.** *Principles of Optics: electromagnetic theory of propagation, interference and diffraction of light.* s.l. : Pergamon Press, 1965.

89. <http://www.mathworks.com>. Matlab.

90. *Plasmonics: Merging Photonics and Electronics at Nanoscale Dimensions.* **Ozbay, Ekmel.** 5758, s.l. : Science, 2006, Vol. 13, pp. 189-193.